In the Trenches of the Solar-Stellar Connection. III. The HST/COS Ecliptic Poles Stellar Survey (EclipSS)

Thomas R. Ayres

Center for Astrophysics and Space Astronomy,
389 UCB, University of Colorado, Boulder, CO 80309;
Thomas.Ayres@Colorado.edu

ABSTRACT

Ecliptic-poles Stellar Survey (EclipSS) collected far-ultraviolet (FUV: 1160–1420 Å) spectra of 49 nearby ($d \lesssim 100$ pc) F3—K3 Main-sequence stars, located at high Ecliptic latitudes (North and South), using Cosmic Origins Spectrograph of Hubble Space Telescope. The Ecliptic poles receive higher exposures from scanning missions like Transiting Exoplanet Survey Satellite (high-precision optical photometry) and Extended Roentgen Survey with an Imaging Telescope Array (X-ray monitoring), which can deliver crucial contextual information, not otherwise easily secured. The objective was to support theoretical studies of stellar hot outer atmospheres—chromospheres ($\sim 10^4$ K) and coronae ($\gtrsim 1$ MK)—which, among other things, can adversely impact exoplanets via host-star "space weather." Flux–flux diagrams (e.g., C II 1335 Å versus O I 1306 Å) were constructed for the EclipSS stars, solar Cycle 23/24 irradiances, and long-term FUV records of α Cen A (G2 V) and B (K1 V). The EclipSS cohort displays similar minimum ("basal") fluxes as the Sun and solar twin α Cen A, in chromospheric O I 1306 Å. In hotter C II 1335 Å, a downward slump of the basal fluxes—noted in previous, less controlled surveys—can now be explained as an effect of sub-solar abundances. The consistent basal minima in chromospheric and higher temperature species at solar metallicity favor the idea that stellar analogs of the solar supergranulation network provide a baseline of high-energy emissions. The magnetic network is replenished by a "local dynamo" independently of the stellar spin. It can operate even when the starspot-spawning internal Dynamo has ceased cycling, as during the Sun's 17th-Century Maunder Minimum.

Subject headings: Sun: activity — Sun: UV radiation — stars: activity — techniques: spectroscopic

1. INTRODUCTION

The initial foray into the "Trenches" series (Ayres 2020a; hereafter Paper I) assessed long-term (decadal) trends in soft X-rays (0.2–2 keV; 6.2–62 Å) and ultraviolet (UV: 1100–3000 Å) fluxes of three low-activity Sun-like dwarf stars: α Centauri A (HD 128620: G2 V), α Cen B (HD 128621: K1 V)[1], and the Sun (G2 V) itself. There were numerous motivations for such a study (see Paper I). Suffice it to say that high-energy proxies of stellar magnetic activity have ramifications across a broad cosmic spectrum, including the Sun's "space weather" and exoplanet host counterparts, atmospheric modeling, and fundamental plasma physics, to mention a few examples. The main empirical outcome of Paper I was a series of "flux–flux" correlations: scatter diagrams pitting intensities from pairs of different species, such as coronal soft X-rays ($T \sim 1$ MK) versus chromospheric Mg II 2800 Å ($T \sim 8000$ K).

Historically, such comparisons involved several dozen, or more, stellar UV spectra and companion X-ray pointings, each object rarely visited more than once, and typically in separated epochs, by the different space facilities needed to access the disparate wavelength bands. Despite the sporadic samples and lack of temporal connectivity, the stellar flux–flux correlations showed clear power-law trends between emissions formed at different temperatures, with increasing slopes for higher excitation species when compared against a lower temperature reference, commonly Mg II, dominant radiative coolant of the chromosphere. Coronal X-rays displayed the steepest power-law slopes ($\alpha \sim 3$) relative to Mg II; intermediate temperature C IV (10^5 K) had a shallower, but still steep, $\alpha \sim 2$; while other chromospheric emissions, such as O I 1305 Å (8000 K) trended closer to 1:1 (see, e.g., Ayres et al. 1995).

Contrasted to the earlier stellar UV/X-ray surveys of numerous objects, but in a one-off fashion, Paper I focused on photometric time series of individual stars over their long-term magnetic cycles. Only the three late-type ("cool") stars mentioned earlier—α Cen AB and the Sun—had suitable cycle-spanning UV and X-ray observations for the purpose. Unexpectedly, the simple power-laws found in the previous stellar work gave way on the Sun to curved relations, and inversions in the activity hierarchy. For example, Si III had steeper flux–flux correlations than N V, despite the latter's four times higher formation temperature (2×10^5 K versus 5×10^4 K). At the same time, the Sun's flux–flux relations paralleled those of low-activity solar twin α Cen A, suggesting that the curious solar behavior was not unique, but perhaps commonplace at the lowest tiers of activity among Sun-like stars. In fact, the cooler, somewhat more active, K dwarf companion α Cen B, displayed correlations more closely aligned with the previous stellar lore (which, to be sure, was biased toward more

[1]Hereafter, α Cen A & B when mentioned together will be denoted "α Cen AB" or simply "AB."

active stars by limited sensitivity of the early measurements).

Paper II (Ayres 2020b) was a quick diversion into the solar extreme ultraviolet (EUV: 100–1100 Å), arising in the $\sim 10^4$ K layers of the Sun's upper chromosphere and hotter regions extending into the ~ 1 MK corona. Moderate resolution (~ 1 Å) EUV irradiance ("Sun as a star") spectra were obtained from the Extreme Ultraviolet Variability Experiment (EVE: Woods et al. 2012) onboard the Solar Dynamics Observatory (SDO: Pesnell et al. 2012) for the years 2010.5–2020.0, capturing the rise and fall of recent (albeit rather tepid) sunspot Cycle 24. The motivation was to explore the variability of key high-excitation EUV emissions over a solar cycle, relative to longer wavelength UV counterparts (e.g., H I 1215 Å Lyα and Mg II 2800 Å) already assessed in Paper I. The solar-stellar connection was that the EUV emissions in the H I Lyman continuum interval (300–920 Å) normally are not visible in stars, even the nearest, owing to severe interstellar atomic hydrogen absorption. Robust scaling relations with UV emissions less affected by the ISM, could allow the unobservable spectra to be reconstructed, at least for stars similar in activity to the Sun.

Predictions of EUV line intensities from more easily collected stellar UV proxies are important to characterize atmospheric mass loss from exoplanets harshly irradiated by their host stars (Airapetian et al. 2020). EUV species play a key role ionizing and heating the uppermost layers of a planetary atmosphere, from which hot ions can escape directly or be swept away by the stellar wind (e.g., Ayres 1997). Flux–flux scaling relations, spanning a wide range of ionization temperatures, can also test solar (and stellar) chromosphere-corona models (see, e.g., review by Linsky 2017).

The present installment of "Trenches" builds on the starspot cycle behavior of the Sun and α Cen AB described in Paper I, by introducing a broader context of Field dwarf stars closely bracketing the solar classification (G2 V). Source of the context stars was the Ecliptic-poles Stellar Survey (EclipSS), an HST Cycle 25 project (GO–15300) to record the 1160–1420 Å "short-FUV" (s-FUV) in a sample of 49 early-F to early-K-type dwarfs in the Ecliptic polar regions (for reasons described shortly), using the high-performance Cosmic Origins Spectrograph (COS: Green et al. 2012) of Hubble Space Telescope (HST).

Paper III is organized as follows. The leading section summarizes the stellar sample; followed by the spectral observations from HST/COS; the merging of the multiple s-FUV wavelength segments of each target; and the line strength measurements. Next, flux–flux correlations are constructed from the stellar s-FUV intensities, including the cycle-spanning solar and α Cen AB relations from Paper I. This, mainly empirical, study concludes with a brief discussion of the results. An Appendix describes the assignment of fundamental stellar parameters to the survey targets, drawing heavily on the Gaia mission (Gaia Collaboration et al. 2016: astrometry, photometry, and radial velocities).

2. OBSERVATIONS

2.1. Considerations for the EclipSS Sample

The EclipSS targets were chosen from candidates situated within 20° of the North or South Ecliptic poles, because these areas were expected to receive special attention from scanning missions like Transiting Exoplanet Survey Satellite (TESS: Richter et al. 2015) and Extended Roentgen Survey with an Imaging Telescope Array (eROSITA: Predehl et al. 2016), owing to the respective survey designs. These complementary missions could provide crucial supporting information to place the HST/COS s-FUV spectra into a more secure diagnostic context, with respect to understanding the origins of the stellar magnetic Dynamo (Parker 1970), at the heart of the cycling activity, and especially its ancillary consequences for atmospheric heating.

NASA's planet-hunting TESS satellite was launched 2018 April into an Earth-Moon resonant orbit. TESS images the sky along a 24°×96° strip using four off-pointed wide-field (24°×24°) cameras, one continuously viewing the Ecliptic pole, the other three arrayed in Ecliptic longitude down to nearly the equator. The sky band ("sector") is advanced every 27.4 d, to maintain the desired spacecraft orientation orthogonal to the Sun–Earth line and allow the Ecliptic hemisphere to be swept out over the course of a year (13 sectors); at which point the satellite flips over to scan the opposite hemisphere. As of this writing, TESS has completed its primary mission (in 2020 July), having covered about 85 % of the sky with at least one 27.4 d sector, but year-long coverage (each) for ∼24°-diameter patches at the North and South Ecliptic poles.

eROSITA is prime instrument of the Russian–German "Spectrum-Roentgen-Gamma" (SRG) mission. SRG was launched 2019 July into a halo orbit around the L2 point (on the anti-sunward side of Earth), to allow uninterrupted viewing of the sky. eROSITA has a wide-field (∼ 1°) soft X-ray imager—a cluster of seven independent high-energy telescopes—which scans along great circles in Ecliptic longitude, precessing 1° d^{-1} to sweep out the full hemisphere in 6 months. eROSITA covers six great circles per day, with about 40 s of on-source time for a given celestial object in each pass. Nevertheless, owing to the convergence of the scan paths at the Ecliptic poles, sources within about 15° of the poles receive higher exposures, as much as ten times or more, compared with the equator. Over the nominal 4-year mission, eight 6-month all-sky surveys are planned. As of this writing, the first one has been completed (in 2020 June), and the second nearly so.

EclipSS intended to take advantage of key supporting information—rotation periods, asteroseismology, and coronal X-ray fluxes—that ultimately would be available from TESS and eROSITA (the HST Guest Observer project was instigated before either mission was

launched). The EclipSS candidates, accordingly, were chosen to be bright enough for TESS and eROSITA, but not too bright (specifically at H I 1215 Å Lyα) for COS (which has strict detector safety screening limits: Lyα is by far the brightest emission line in the s-FUV spectrum of a normal star, even when attenuated by interstellar hydrogen absorption). For example, the TESS bright limit (where saturation effects become important) is about $V = 5$, while the optimum photometric error occurs for objects between 7th and 9th magnitude (depending on spectral type). For stars with the minimum visibility (i.e., one 27.4 d sector, near the Ecliptic equator), asteroseismology is possible down to about $V = 7.5$, but that limit likely would be pushed a magnitude, or more, fainter near the poles, where the minimum visibility is >80 d at 20°, and >300 d within 12°. (To be sure, the 2-minute cadence used for seismic targets in the initial TESS all-sky survey is not optimum for the cooler dwarfs. Nevertheless, an even faster, more suitable, 20 s sampling is available for selected targets in the extended mission, currently underway.)

The TESS stars near the poles are especially valuable for discerning systematic photometric variations caused by stellar rotation (e.g., Canto Martins et al. 2020). The stellar rotation is a key ingredient in the magnetic Dynamo, and is difficult to measure in low-activity stars because the modulation contrast usually is too low to track successfully from the ground. The typical TESS target away from the poles receives only one 27.4 d sector of exposure, similar to the 25 d solar rotation period. This is too short to reliably measure the period of a middle-age star like the Sun, which would require at least three repeats of a photometric cycle for a secure period confirmation, perhaps more during low-activity starspot-free intervals when the photometric contrast is especially low. Of course, faster spinning active stars would be more accessible in a single sector. Nevertheless, for active dwarfs a months-to-year near-continuous photometric time series could potentially assess latitudinal differential rotation effects, as well as inventory large white-light flares ("superflares:" see Tu et al. 2020), which are of interest as rare, but extreme events, possibly relevant to the Sun-Earth connection itself (Notsu et al. 2019).

The Ecliptic poles also benefit from higher exposures by eROSITA, which by the nature of its scanning program could provide soft X-ray detections for bright late-type coronal sources on a variety of timescales, from hours to days and months to years, over the planned 4-year survey phase. The total exposure over the full mission is expected to be about 2 ks near the Ecliptic equator, but 5 ks 20° from the Ecliptic poles, 9 ks at 10°, and 20 ks, or more, within 6°. The soft sensitivity (0.2–2 keV) of the cameras is excellent, and the quoted limiting luminosity (in the harder 0.5–2 keV band) is about $2{\times}10^{27}\,(d/40\,\mathrm{pc})^2$ erg s^{-1} (40 pc is the mean distance of the EclipSS F9–G5 Sun-like stars) near the Ecliptic equator (Robrade 2017); which translates to about $2{\times}10^{26}\,(d/40)^2$ within 6° of the poles, and up to about $8{\times}10^{26}$ within 20°; the latter limit is similar to the cycle-average $L_{\mathrm{X}}^{\odot}$. Because some

of the EclipSS sources were expected to be more active than the Sun—itself pretty much at the bottom of the coronal heap—not only would long-term average L_X's be collected, but also time variability over the 4-year survey, perhaps enough to see cycle changes in at least the cooler sample members (early-K-type α Cen B has an X-ray period of about 8 years: Paper I).

Beyond TESS and eROSITA, the Ecliptic polar regions have good accessibility for pointed satellites, like HST, Chandra X-ray Observatory, XMM-Newton, and upcoming James Webb Space Telescope, because the poles always are well away from the solar avoidance zones (within 45° of the Sun for HST). The poles also are good for ground-based astronomy for a similar reason.

An additional selection step for EclipSS was to examine the fields around each of the potential candidates, to check whether another bright star might be too close to the desired target. The source extraction region for eROSITA is $1'$ in diameter, while the 90% ensquared energy box for TESS is $1.4' \times 1.4'$. So, one wants to avoid bright stars within about $2'$ of a candidate target, which might otherwise affect the X-ray count rate, as well as add optical loading on the eROSITA CCDs; or contaminate the TESS photometry. A number of candidates were eliminated on that basis, leaving a final list of 49. EclipSS is less biased than historical bright-star samples (e.g., Ayres et al. 1995), because there was no pre-selection according to FUV emission-line strengths, unknown for these faint stars.

The Gaia G (broad-band optical) magnitudes of the selected targets are in the range 6.8–8.6 mag. The sample falls almost entirely within the extended 100 pc solar neighborhood. The distances and other stellar properties are well characterized by Gaia Data Release 2 (DR2[2]), as well as the previous Hipparcos astrometric sky survey and optical catalogs of stellar effective temperatures, surface gravities, and metallicities (an important contributor was the TESS Input Catalog (TiC): Stassun et al. 2018).

[2]see: http://simbad.u-strasbg.fr/simbad/sim-ref?bibcode=2018yCat.1345....0G

Table 1. EclipSS Targets and Summary Stellar Properties

Name	Type	β	d	G	$(bp-rp)$	$\upsilon_{\rm R}$	$T_{\rm eff}$	$\log g$	[Fe/H]	$f_{\rm BOL}$
		(°)	(pc)	—	(mag) —	(km s^{-1})	(K)	(cm s^{-2})		(10^{-8})
(1)	(2)	(3)	(4)	(5)	(6)	(7)	(8)	(9)	(10)	(11)
Sun	G2	0	$4.8\,10^{-6}$	−26.90	0.82	+0	5772	4.439	+0.00	$1.361\,10^{14}$
HD 128620[a]	G2	−43	1.338	···	···	−22	5800	4.31	+0.24	2718
HD 128621[a]	K1	−43	1.338	···	···	−21	5230	4.54	+0.22	899
HD 20052	G0	−72	78.9	8.175	0.744	+28	6150	···	···	1.23
HD 21166	F4	−75	83.9	7.117	0.580	+7	6660	···	···	3.26
HD 22359[b]	F6	−73	55.0	(7.46)	0.621	(+2)	6310	···	···	2.37
HD 24293	G3	−76	42.2	7.684	0.836	+22	5730	4.21	−0.08	1.96
HD 24636	F3	−77	57.0	7.022	0.538	+15	6780	···	···	3.57
HD 28471	G3	−80	43.7	7.728	0.824	+55	5750	4.40	−0.04	1.88
HD 28481	F7	−73	103.4	8.167	0.656	+31	6250	···	···	1.24
HD 28701	G3	−81	44.3	7.695	0.821	−7	5750	4.36	−0.30	1.96
HD 29255	F7	−80	82.4	8.257	0.654	+8	6410	···	···	1.14
HD 30501	K2	−71	20.4	7.339	1.061	+23	5130	4.51	+0.08	2.87
HD 32778	G3	−78	22.3	6.841	0.831	+1	5720	4.48	−0.59	4.36
HD 34297	G4	−78	34.9	7.144	0.852	(+32)	5620	4.40	−0.65	3.32
HD 36767	F9	−80	36.1	7.020	0.718	+46	6090	4.42	···	3.55
HD 38459	K0	−71	37.1	8.292	1.013	+27	5260	4.48	+0.21	1.17
HD 39194	G8	−86	26.4	7.852	0.973	+14	5250	4.57	−0.62	1.79
HD 39755	F3	−85	80.9	7.739	0.539	+2	6820	···	···	1.85
HD 41004[c]	K3	−72	41.6	8.376	1.092	+43	5180	4.39	+0.18	1.10
HD 42286	K2	−83	27.0	8.189	1.073	+24	5050	4.61	···	1.33

Table 1—Continued

Name	Type	β	d	G	$(bp-rp)$	$v_{\rm R}$	$T_{\rm eff}$	$\log g$	[Fe/H]	$f_{\rm BOL}$
		(°)	(pc)	—	(mag) —	(km s^{-1})	(K)	(cm s^{-2})		(10^{-8})
(1)	(2)	(3)	(4)	(5)	(6)	(7)	(8)	(9)	(10)	(11)
HD 47252	G9	−86	28.1	8.033	0.987	+43	5260	4.59	···	1.49
HD 51608	G8	−77	35.1	7.961	0.954	+40	5380	4.39	−0.07	1.57
HD 51929	G1	−78	37.4	7.240	0.779	+66	5800	4.21	−0.65	3.02
HD 53658	F6	−84	56.6	7.213	0.627	+7	6480	···	···	2.98
HD 55720	G5	−71	27.6	7.309	0.892	+87	5510	4.54	−0.31	2.84
HD 56737	F5	−80	59.4	7.040	0.600	+7	6480	···	···	3.49
HD 62850	G2	−76	32.9	7.033	0.791	+18	5880	4.38	···	3.53
HD 63765	G6	−72	32.6	7.910	0.921	+23	5460	4.47	−0.13	1.63
HD 64184	G4	−76	33.4	7.312	0.862	−9	5670	4.47	−0.19	2.79
HD 73744	G2	−75	36.7	7.424	0.789	+48	5850	4.47	···	2.47
HD 137826	G5	+75	49.0	8.556	0.883	−35	5540	4.35	−0.34	0.90
HD 144061[d]	G2	+78	29.6	7.120	0.801	−9	5680	4.40	−0.29	3.34
HD 146044	G5	+76	42.5	7.934	0.872	−67	5600	4.39	−0.15	1.58
HD 146868	G4	+77	31.0	7.510	0.853	−18	5640	4.37	−0.28	2.34
HD 147231	G5	+80	40.2	7.654	0.881	−17	5610	4.46	−0.03	2.03
HD 150706	G1	+76	28.3	6.850	0.780	−17	5920	4.48	−0.03	4.18
HD 151541	G8	+82	24.2	7.344	0.953	+9	5320	4.40	−0.20	2.79
HD 154956	F8	+76	92.1	8.141	0.679	−11	6180	···	···	1.27
HD 156389[e]	F6	+78	86.4	7.707	0.626	(−6)	6450	···	···	1.89
HD 156559	F3	+80	82.0	7.782	0.553	−18	6760	···	···	1.78
HD 159329	G0	+86	45.7	7.519	0.737	−34	6070	···	···	2.25

Table 1—Continued

Name	Type	β	d	G	$(bp-rp)$	$\upsilon_{\rm R}$	$T_{\rm eff}$	$\log g$	[Fe/H]	$f_{\rm BOL}$
		(°)	(pc)	——	(mag) ——	(km s^{-1})	(K)	(cm s^{-2})		(10^{-8})
(1)	(2)	(3)	(4)	(5)	(6)	(7)	(8)	(9)	(10)	(11)
HD 161897	G5	+84	30.0	7.418	0.889	−17	5610	4.52	−0.02	2.52
HD 165700	F8	+79	88.7	7.645	0.673	(−12)	6210	···	···	2.00
HD 168093	F9	+74	53.9	7.507	0.723	−9	6060	4.14	−0.15	2.29
HD 172669	G2	+86	36.1	7.415	0.798	−7	5950	···	···	2.48
HD 180712	G1	+79	45.1	7.822	0.781	−14	5880	4.43	+0.06	1.71
HD 185239	F5	+76	81.5	8.033	0.606	+11	6490	···	···	1.40
HD 187876	G0	+74	46.6	7.611	0.755	−52	6010	···	···	2.07
HD 199476	G5	+74	30.9	7.625	0.884	−30	5490	4.54	−0.47	2.14
HD 201651	G7	+73	32.3	7.987	0.932	−13	5340	4.48	−0.29	1.55
HD 202123	K1	+73	31.5	8.444	1.048	+7	5160	4.47	−0.34	1.04

Note. — Col. 2 spectral types based on a Gaia color-transformation (see Appendix A). Col. 3 is the Ecliptic latitude. Parallax-based distances (Col. 4), G magnitudes (Col. 5), and $(bp-rp)$ colors (Col. 6) are from Gaia DR2. Radial velocities (Col. 7) are mainly from Gaia, with a few exceptions originating from SIMBAD (parenthetical values) if not available in DR2. Effective temperatures (Col. 8), surface gravities (Col. 9), and metallicities (Col. 10) are described in Appendix A. Units for the bolometric fluxes (Col. 11) are: erg cm^{-2} s^{-1}. In the Table footnotes, below, "Hipp" refers to the Hipparcos satellite and "WDS" to the Washington Visual Double Star Catalog (Mason et

al. 2001), both accessed through SIMBAD. For the binary star entires, "PA" is the position angle, "sep" is the separation, the third quantity is the magnitude difference, and the trailing parenthetical value is the epoch of measurement.

[a] α Cen AB parameters mainly from Kervella et al. (2017) (See Paper I). The cited radial velocities are empirical, based on fits to low-excitation, narrow chromospheric emission lines in co-added HST/STIS E140M-1425 spectra. The co-addition/cross-correlation process favored the velocity scale of the leading observation in each series, circa 2010 in both cases.
[b] Revised G magnitude: see Table A1. Binary (Hipp): PA= 85°, sep=0.74″, ΔHp = 0.35 mag (1991); Binary (WDS): PA= 64°, sep= 0.70″, ΔV=0.42 mag (2018).
[c] Binary (Hipp): PA= 176°, sep= 0.54″, ΔHp = 3.68 mag (1991); Binary (WDS): PA= 153°, sep= 0.30″, ΔV= 3.69 mag (2019).
[d] Binary (WDS): PA= 29°, sep= 2.4″, ΔV= 5.0 mag (2015).
[e] ϖ from Hipp (no DR2); Binary (Hipp): PA= 319°, sep= 0.38″, ΔHp = 0.28 mag (1991); Binary (WDS): PA= 335°, sep= 0.40″, ΔV= 0.66 mag (2019).

Table 1 summarizes stellar parameters of the sample, including Gaia magnitudes, colors and distances; as well as consensus effective temperatures, gravities, and metallicities aggregated as described in more detail in the Appendix. Note in Table 1 the quantity $f_{\rm BOL}$, the stellar bolometric flux (equivalent to the stellar irradiance: erg cm^{-2} s^{-1} at Earth). It will be used later to normalize stellar s-FUV flux densities and integrated line intensities, as a way to de-bias star-to-star comparisons, given the wide range of stellar distances and sizes in the sample (especially considering the Sun and nearby (1.3 pc) α Cen AB versus the $\sim$40 pc Sun-like dwarfs of EclipSS)[3].

Figure 1 is a rogues' gallery of the EclipSS targets, incorporating schematic renditions of the COS FUV spectra (described later), and also including equivalent tracings for the Sun and α Cen AB. The postage-stamp images are $5'$ on a side, and were obtained from the Digital Sky Survey (DSS, hosted by the Infrared Science Archive[4] at the California Institute of Technology). A green-dashed boundary enclosing the middle section of the diagram highlights the stars considered "Sun-like," namely within $\pm$3 subtypes of the solar G2 classification. The schematic COS spectral lines are depicted on a common, linear $f_\lambda / f_{\rm BOL}$ "flux density" scale ("FD$\star$" in lowermost left panel), so the activity level of the object is directly related to the apparent strength of the features. The three illustrated spectral bands, separated by thin vertical dark dashed lines, are: at left, Si III 1206 Å (5×10^4 K); middle, C II 1334 Å + 1335 Å (2×10^4 K); and right, Si IV 1393 Å (8×10^4 K). The spectral views are 2 Å-wide at left and right, and 3 Å in the middle. The C II 1334 Å ground-state transition (left of center) is often degraded by interstellar C^+ absorption: narrow central dips can be seen in the higher resolution α Cen features (from the HST Space Telescope Imaging Spectrograph (STIS): see Paper I). The solar profiles to the left naturally are free of interstellar absorption, but noticeably are broader than their stellar counterparts owing to the much poorer resolution of the SORCE/SOLSTICE irradiance spectrometer (but nevertheless adequate to allow accurate emission-line measurements of several key species: see Paper I). Notice that many of the targets have low apparent emission line strengths, an outcome of the relatively unbiased sample construction (fast-rotating active dwarfs are most commonly found in young clusters, and are relatively rare in the Field).

---

[3]Note: $f \,/\, f_{\rm BOL}$ is equivalent to $L \,/\, L_{\rm BOL}$. Further, $f_{\rm BOL}$ is related to the energy density available in the stellar surface layers to drive local dynamo action (e.g., Nordlund et al. 1992), as well as the turbulent stressing of magnetic fibrils, which could cause plasma heating in the immediate vicinity as well as in higher layers. $f \,/\, f_{\rm BOL}$ also is related to the irradiation levels in the Habitable Zone around a host star, because only a narrow range of $f_{\rm BOL}$ near the terrestrial value of 1.4 kW m^{-2} would permit sufficiently temperate conditions on a planetary surface for liquid water to exist.

[4]https://irsa.ipac.caltech.edu/data/DSS/

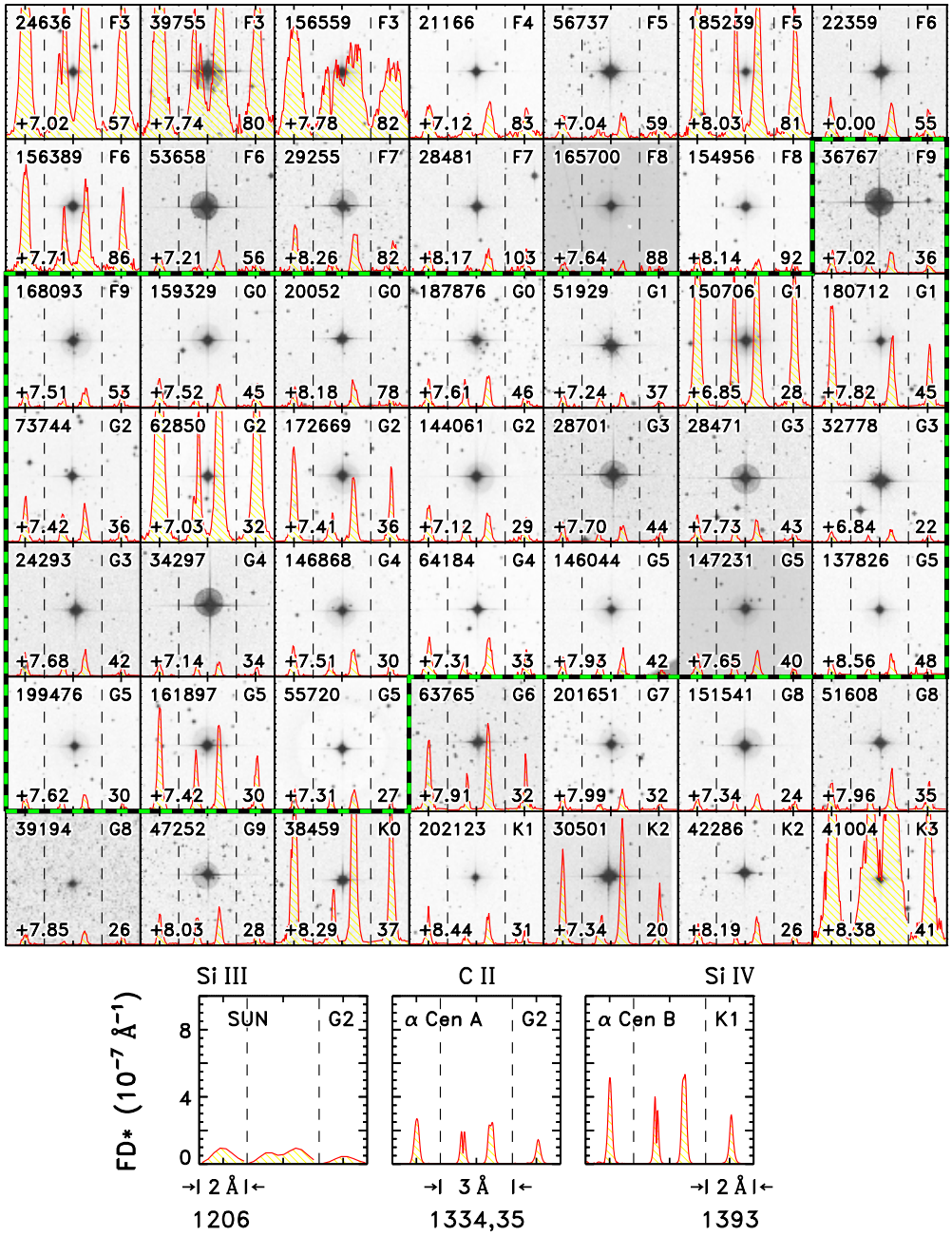

Fig. 1.— Snapshots of the EclipSS targets from the Digital Sky Survey, with superimposed schematic FUV spectra from HST/COS. The large middle section of the diagram bordered by a green-dashed line highlights the stars considered "Sun-like," i.e., within a few spectral types of the solar G2 classification. Subtitles in each panel, clockwise from upper left are: HD number, spectral type, distance (in pc), and Gaia G magnitude. Bottom group of panels, for the Sun and α Cen AB, summarize the schematic emission lines, from left to right: Si III 1206 Å, C II 1334 Å + 1335 Å, and Si IV 1393 Å. The y-axis is bolometrically normalized flux density with the scale and units indicated in the bottom left frame.

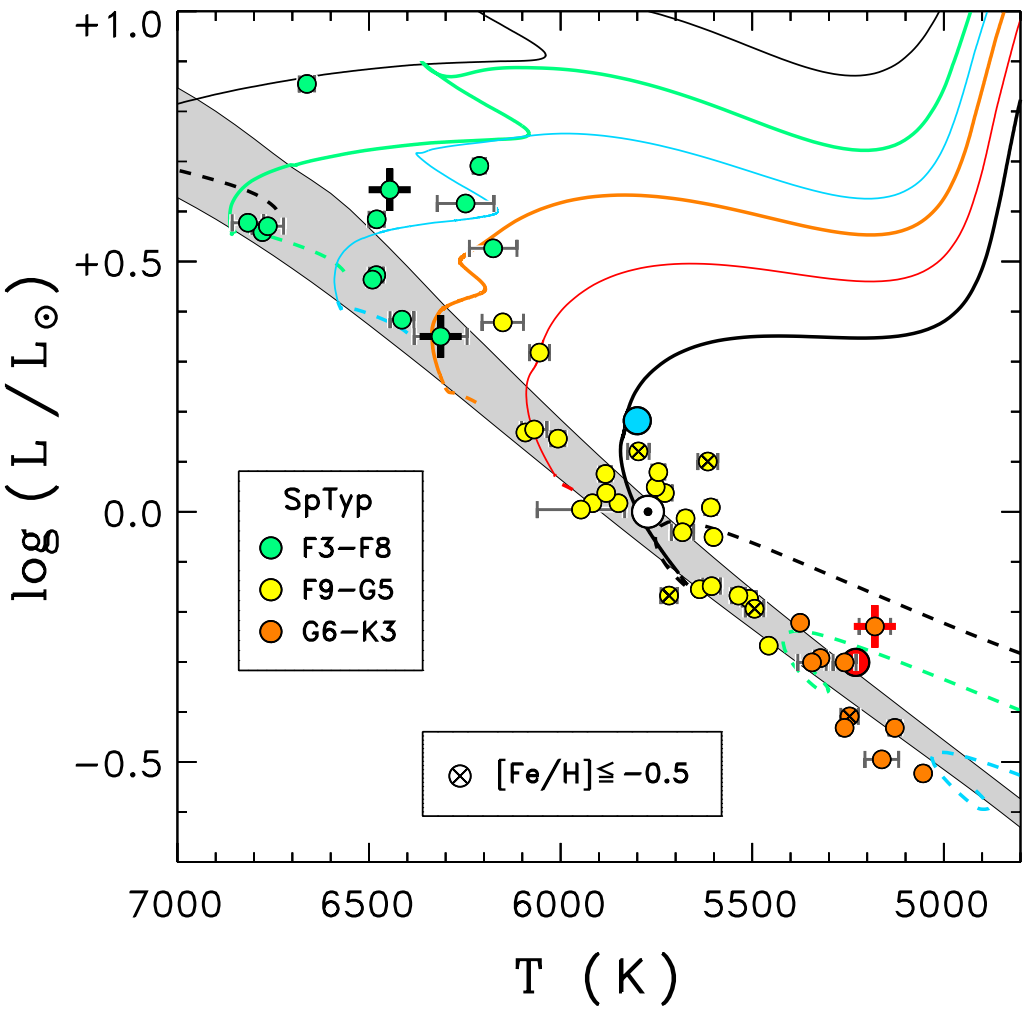

Fig. 2.— Hertzsprung–Russell Diagram of the EclipSS targets (smaller dots, color-coded by spectral type according to the legend). The Sun is marked ⊙, and α Cen AB by larger blue and red dots, respectively. Dark gray horizontal error bars indicate uncertainties in the effective temperatures; equivalent uncertainties in the (Gaia-based) luminosities are smaller than the symbol sizes. Light gray band marks the Zero Age Main Sequence along the lower edge, and the 50 % Main-sequence lifetime at the upper edge. Solid curves are post-ZAMS tracks starting at the Sun (1 $M_{\odot}$) and extending to the left in increments of 0.1 $M_{\odot}$. Dashed curves are Hayashi tracks: more complete view for the Sun, and for lower masses in 0.1 $M_{\odot}$ steps to the right; but only the terminal portions of the tracks at the higher masses. Symbols marked by dark pluses are visual binaries with near-equal components and separations smaller than the COS aperture (so are observed together). The object marked with a red plus is another close visual binary, but with a bright primary and faint companion. Small × indicates reduced metallicity (below one-third solar).

Figure 2 is a Hertzsprung–Russell (H–R) diagram of the sample, based on the summary stellar parameters of Table 1 (described in more detail in the Appendix). Solid curves are post Zero Age Main sequence (ZAMS) PARSEC evolutionary tracks (Bressan et al. 2012), and dashed curves are pre-Main sequence Hayashi tracks. The shaded Main-sequence (MS) band represents the spread between the ZAMS (lower boundary) and the point at which a star has reached 50 % of its MS lifetime (upper boundary), for PARSEC models with standard solar composition. Sun-like comparison stars α Cen AB are the larger blue and red dots, respectively. Like slightly evolved α Cen A, several of the F stars lie above the upper MS boundary, presumably because they too are entering post-MS territory (although unrecognized binaries, with components of near-equal brightness, also are a possibility). At the same time, most of the G and K dwarfs fall within, or close to, the MS band. Dark pluses mark two known visual binaries with companions of similar V magnitude, while the red plus is for the one previously classified close binary with unequal components: a bright primary and faint secondary. The binaries are described in more detail below.

One of the EclipSS targets, HD 22359, was found, after DR2 was released, to have an inconsistent, anomalously low, Gaia magnitude ($G = 7.855$) relative to the (earlier) Hp from Hipparcos[5] over a similarly broad optical bandpass; and also when compared in an $L_{\rm BOL}$ versus $T_{\rm eff}$ H–R diagram. The star is a visual binary with near-equal components ($\Delta Hp \sim 0.35$ mag), and a small separation ($\sim 0.7''$) according to Hipparcos. A revised G (+7.46 mag) was assigned to HD 22359 based on an empirical correlation between $G - Hp$ as a function of broad-band colors, for example Gaia ($bp - rp$), Hipparcos cataloged ($B - V$), or the Hipparcos ($V - I$). Even with the revised value, the H–R diagram position of HD 22359 in Fig. 2 still is slightly below that expected given the similar brightnesses of the companions.

One of the other targets, HD 156389, also is a visual binary with a small separation and near-equal components, although in this case the total bolometric luminosity in Fig. 2 is consistent with those attributes. However, for this star (only), Gaia DR2 did not provide a parallax, so the distance was based on the earlier Hipparcos ϖ; sufficiently accurate, given that the star is only 86 pc away, well within the Hipparcos horizon.

A third star, HD 41004, also is a close visual binary ($0.5''$ separation). But, in this case the magnitude difference is large ($\Delta Hp \sim 3.7$ mag), so any spectral influence on the early-K dwarf primary by the M-type companion is expected to be negligible. Zucker et al. (2004) report that the system has additional, hierarchical complexity: a Brown Dwarf orbiting the faint secondary star and a multi-Jovian-mass planet orbiting the primary. Curiously, however, HD 41004 sits slightly above the ZAMS in Fig. 2, as if it were a binary with

[5]ESA, 1997, VizieR Online Data Catalog, I/239

components of similar brightness. Alternatively, HD 41004 might be very young and still contracting toward the ZAMS. Its high activity level, a characteristic of youth, provides some support for that possibility.

Finally, a fourth target, HD 144061, is another visual binary with a dominant primary and faint secondary ($\Delta V \sim 5$ mag), but the 2.4″ separation is large enough that the dim companion would fall outside the 2.5″-diameter Primary Science Aperture (PSA) of the COS s-FUV channel. A number of the other EclipSS stars are even wider binaries, but are not explicitly noted here because the fainter secondaries would have no influence on the COS spectra (recall that candidates with over-bright visual secondaries that might affect TESS or eROSITA already were weeded out during the initial selection process).

2.2. HST/COS s-FUV Channel

COS is a "faint object" ultraviolet spectrograph optimized for moderate-resolution ($\lambda/\Delta\lambda \sim 18{,}000$) UV spectroscopy of dim sources, such as Active Galactic Nuclei, quasar absorption-line systems, and, in the case of EclipSS, distant cool dwarf stars. COS was installed in Hubble in 2009 during Servicing Mission 4. Many nearby late-type stars are too bright in the s-FUV for COS, violating detector safety limits, mainly because of their strong chromospheric H I 1215 Å Lyα (normally dominant emission of the s-FUV region). Consequently, it was important to select EclipSS targets that would be "safe" for Lyα, but still bright enough to have measurable fluxes of other important s-FUV species, like Si III 1206 Å, N V 1238 Å, C II 1335 Å, and Si IV 1393 Å, and also be suitable for, e.g., TESS and eROSITA (as described earlier).

The original plan called for a pair of COS G130M CENWAVEs—1291 Å and 1327 Å—to cover the 1160–1420 Å range without gaps, in a single HST orbit for each star. Two FP-POS splits were designated for each CENWAVE[6]. However, following the HST Cycle 25 selection process, a new COS policy[7] was adopted to minimize detector aging at Lyα due to persistent, saturated geocoronal emission through the PSA. All the supported G130M CENWAVEs admitted Lyα, which had forced the original EclipSS target selection to the fainter magnitudes. The new policy disqualified all but one of these CENWAVEs for use with the FUV short-wavelength side-b camera segment, where the strong hydrogen line falls. Only G130M–1291 was allowed to activate both camera sides (a and b), and just two of the FP-

[6]The splits are small grating rotations that move the spectrum on the COS FUV detector in discrete steps to suppress camera "fixed pattern noise"

[7]see: https://www.stsci.edu/hst/instrumentation/cos/proposing/cos2025-policies

POS (3 and 4) were permitted. Normally, four splits would be needed to adequately suppress fixed pattern noise. To counter-balance the excluded side-b settings, a new CENWAVE was introduced, 1222 Å, which dispensed with Lyα by placing it in the detector gap, but still captured (just barely) important Si III 1206 Å and N V 1238 Å. All four FP-POS were allowed with the new setting. It was decided to use the G130M 1291 Å CENWAVE at the two permitted FP-POS, together with 1222 Å, also at FP-POS 3 and 4. The four exposures would fully cover the s-FUV range, especially the important emissions below Lyα, and could be fitted in the single HST orbit allocated for each target.

The EclipSS stars were bright enough that an efficient near-ultraviolet (NUV) imaging acquisition could be done, with the neutral-density (ND) filtered Bright Object Aperture (BOA) and Mirror A or B (the latter also ND-filtered) depending on the target V magnitude. The typical NUV-ACQ exposure was less than a minute. The acquisition was followed by the two s-FUV G130M settings, 1222 Å and 1291 Å, at the pair of FP-POS splits. The same integration time, typically 20 m, was used for each setting. This double-setting, dual-split sequence was slightly less efficient than using a single CENWAVE at the four default FP-POSs. However, that only would have been possible with G130M–1222, whose detector side-a red edge is at 1360 Å, so diagnostically important transitions—including the Si IV 1393 Å + 1402 Å doublet and O IV 1401 Å—at longer wavelengths would have been sacrificed.

The modified strategy allowed most of the s-FUV wavelengths to be recorded by four independent grating tilts, important for fixed pattern suppression. Also, with this choice of settings the O I resonance triplet[8] near 1305 Å was in all four splits, so that skyglow-free emission profiles might be captured during periods of low backgrounds (spacecraft night). This was the case for all but 3 of the 49 EclipSS visits. Similarly, key C III 1175 Å complex, C II 1334 Å + 1335 Å multiplet, and valuable coronal forbidden lines—Fe XII 1241 Å (1 MK) and Fe XXI 1354 Å (10 MK)—also were in all four sub-exposures, thereby achieving maximum S/N; while important bright Si III 1206 Å, just shortward of Lyα, was in three.

[8]In what follows, the oxygen triplet, 1302 Å + 1304 Å + 1306 Å, will be designated "O I 1305 Å," to distinguish the multiplet from the individual components.

Table 2. HST/COS Observing Log

Name	Visit	ACQ	Mirror	$t_{\rm acq}$ (s)	U.T. Start (yyyy-mm-dd.dd)	$t_{\rm exp}$ (s)	BL?	$N_{\rm OXY}$
(1)	(2)	(3)	(4)	(5)	(6)	(7)	(8)	(9)
HD 20052	15	i6q	A	5	2019-02-12.46	1180	···	2
HD 21166	05	f4q	B	16	2018-12-15.81	1226	···	1
HD 22359	10	nnq	B	37	2018-12-09.40	1148	···	2
HD 24293	26	ahq	A	7	2018-10-29.79	1178	···	3
HD 24636	04	ifq	B	16	2018-12-11.53	1226	√	4
HD 28471	53[a]	otq	A	7	2019-04-03.36	1178	···	2
HD 28481	09	f7q	A	4	2018-12-10.81	1142	···	4
HD 28701	22	mlq	A	6	2018-11-01.17	1216	···	2
HD 29255	51[b]	n2q	A	4	2018-09-01.91	1238	···	1
HD 30501	49	yiq	A	14	2019-03-23.33	1132	···	1
HD 32778	34	ypq	B	45	2018-12-14.65	1130	···	4
HD 34297	35	a2q	A	5	2018-05-04.04	1234	···	2
HD 36767	18	k3q	B	31	2018-04-03.06	1208	···	1
HD 38459	48	pfq	A	32	2019-03-21.38	1076	···	1
HD 39194	41	voq	A	12	2018-12-13.73	1230	···	3
HD 39755	02	sdq	B	27	2018-08-23.27	1158	√	3
HD 41004	46	k6q	A	36	2018-10-31.77	1072	√	2
HD 42286	47	exq	A	32	2018-08-20.91	1142	···	1
HD 47252	44	zoq	A	14	2018-12-14.75	1208	···	3
HD 51608	42	orq	A	12	2018-12-09.62	1162	···	4
HD 51929	21	bfq	A	4	2018-12-14.92	1170	···	2
HD 53658	08	phq	B	28	2018-12-12.87	1194	···	2
HD 55720	37	hbq	A	6	2018-08-26.87	1116	···	1
HD 56737	06	a1q	B	17	2018-12-10.04	1168	···	2
HD 62850	25	hbq	B	54	2018-08-21.19	1120	√	1
HD 63765	38	k5q	A	8	2018-08-14.87	1138	···	2
HD 64184	27	vfq	A	6	2018-08-24.16	1168	···	0
HD 73744	28	a4q	A	7	2018-08-25.17	1232	···	1

Table 2—Continued

Name	Visit	ACQ	Mirror	$t_{\rm acq}$ (s)	U.T. Start (yyyy-mm-dd.dd)	$t_{\rm exp}$ (s)	BL?	$N_{\rm OXY}$
(1)	(2)	(3)	(4)	(5)	(6)	(7)	(8)	(9)
HD 137826	33	y1q	A	58	2018-01-26.13	1150	···	2
HD 144061	31	orq	A	6	2019-04-10.95	1236	···	1
HD 146044	20	l3q	A	6	2018-12-26.18	1168	···	1
HD 146868	32	t7q	A	7	2018-12-20.32	1178	···	2
HD 147231	29	peq	A	8	2018-12-09.89	1234	···	2
HD 150706	24	ofq	B	45	2018-12-19.49	1194	√	3
HD 151541	43	epq	A	8	2018-12-22.48	1214	···	3
HD 154956	07	e1q	A	4	2018-08-20.40	1142	···	2
HD 156389	03	vvq	B	26	2018-08-17.16	1148	√	1
HD 156559	01	u0q	B	0[c]	2018-08-24.04	1144	√	1
HD 159329	17	f1q	B	0[d]	2018-08-19.14	1138	···	1
HD 161897	39	heq	A	8	2018-10-02.11	1234	···	1
HD 165700	12	x4q	B	54	2018-08-17.29	1120	···	2
HD 168093	14	b4q	B	48	2018-08-18.25	1084	···	2
HD 172669	23	fdq	A	4	2018-08-19.22	1218	···	1
HD 180712	16	dbq	A	4	2018-08-18.88	1170	···	0
HD 185239	13	aqq	A	6	2018-08-18.15	1168	√	1
HD 187876	19	jbq	A	4	2018-12-11.87	1170	···	2
HD 199476	36	d6q	A	6	2018-11-29.97	1236	···	1
HD 201651	40	ugq	A	12	2019-01-11.23	1210	···	0
HD 202123	45	dyq	A	38	2018-06-25.44	1204	···	2

Note. — In Col. 3, the NUV imaging acquisition ("ACQ") dataset is "ldg1" + Visit Number (Col. 2) + ACQ-name (Col. 3), i.e., ldg115igq for HD 20052 (first entry). All the NUV acquisitions were with the Bright Object Aperture (BOA) plus Mirror A or B (Col. 4), depending on target brightness. Col. 6 Start Time is for the NUV ACQ at the beginning of the sequence. Col. 7 exposure time was the same for G130M-

1222 and G130M-1291, each of which was split into equal sub-exposures (i.e., $t_{\rm exp}/2$) at FP-POS 3 and 4. The datasets are named "ldg1" + Visit Number + "010" for G130M-1222 and "ldg1" + Visit Number + "020" for G130M-1291, i.e., ldg115010 and ldg115020 for HD 20052. In Col. 8, a check mark indicates that the spectrum is broad-lined ("BL"). Col. 9 lists the number of low-airglow FP-POS splits included in the O I 1305 Å triplet region: "0" means that all the splits were too contaminated to qualify.

[a] Repeat of Visit 30, which had delayed Guide Star acquisition; subsequent G130M exposures blank.
[b] Repeat of Visit 11, which had failed Guide Star acquisition; subsequent G130M exposures blank.
[c] 30 s planned exposure, but the Guide Star acquisition was delayed, and the COS internal shutter remained closed for the NUV imaging ACQ. Nevertheless, the G130M exposures appear unaffected.
[d] 47 s planned exposure, but the Guide Star acquisition failed, and the COS internal shutter remained closed for the NUV imaging ACQ. Nevertheless, the G130M exposures appear unaffected.

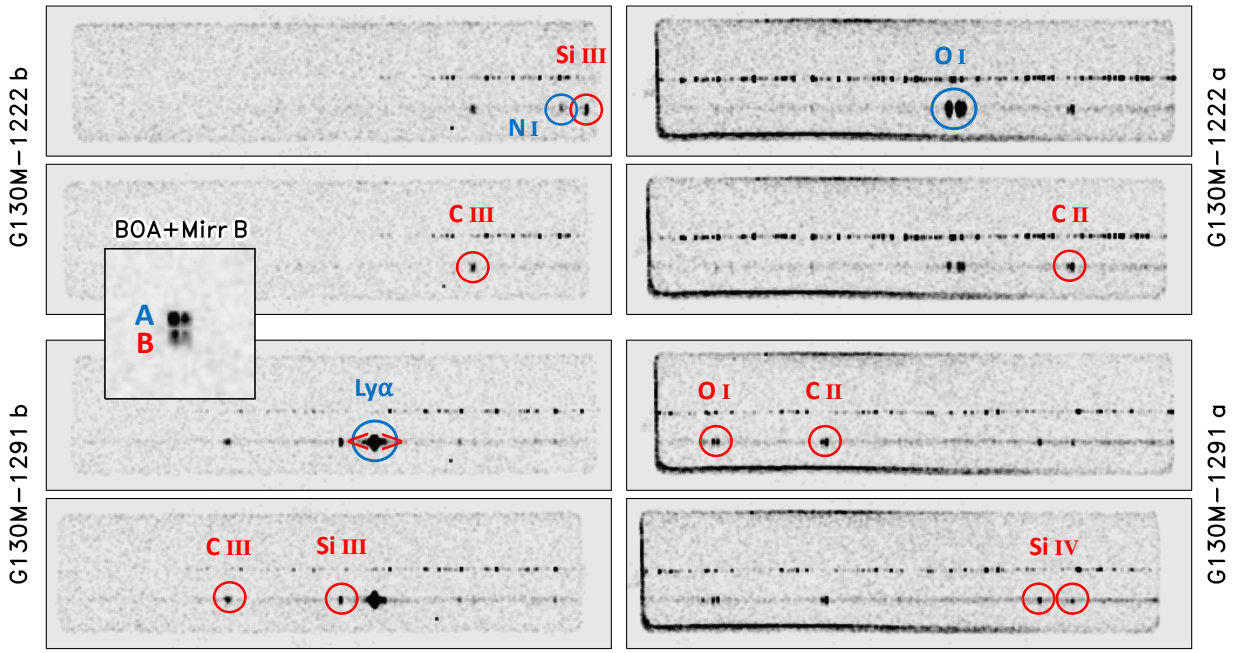

Fig. 3.— Visualization of the COS observing sequence for the close binary HD 22359. The inset panel at middle left shows the NUV acquisition image, in this case doubled in the vertical direction by the close binary companions ("A" and "B"), and doubled in the horizontal direction owing to a glint in Mirror B. The horizontally oriented spectral images are from the two grating settings: G130M-1222 FP-POS= 3 and 4 for the upper pair, and G130M-1291 3 and 4 for the lower; detector side "b" to the left and "a" to the right. The stellar spectrum appears in the lower portion of each frame. The thin emission line trace above the stellar spectrum is the "lamp-flash" wavelength calibration. Features that are dominantly airglow are circled in blue; those that are stellar are circled in red. Helpfully, the bright oxygen airglow in the upper right panels has faded in the lower panels, unveiling the intrinsic stellar emission.

Table 2 summarizes the COS G130M pointings on the EclipSS targets. Figure 3 depicts the sequence of COS acquisition and spectral exposures for the previously mentioned close visual binary HD 22359. For this system, and the other previously known close binary with near-equal components (HD 156389), a visit-level ORIENT constraint was imposed to ensure that the binary separation would be orthogonal to the dispersion axis. The central part of the NUV acquisition image is illustrated in the inset panel at middle left, labeled with the instrumental setup, "BOA + Mirr B." The displayed acquisition postage stamp is 6″ on a side. Surprisingly, the NUV image appears to have quadruple point sources, a perhaps unsettling sight for an observer expecting just a double. In reality, the left-most vertical image pair represents the brighter A component of the binary (upper) and fainter B (lower), separated

by 0.7″, and differing somewhat in NUV brightness; while the horizontally replicated spots are due to a glint in (attenuated) Mirror B. The other binary with components of similar brightness, HD 156389, also showed a doubled NUV/ACQ image. Aside from these two, all the other acquisition images were single. If any of these "single" targets are unrecognized near-equal binaries, the separation must be below the COS resolution ($\sim 0.3''$).

The upper two sets of frames display the G130M–1222 splits. The images are from the CALCOS pipeline-processed flat-fielded science files ("flt"), which were built up from the time-tagged event lists, corrected for geometrical distortions, pixel-to-pixel sensitivity variations, dead-time effects in the counting electronics, and re-binned onto a linear wavelength scale. Note the slight horizontal spatial shift of the detector images, due to the FP-POS splits, in the fixed-wavelength flt reference frame. In that system, the stellar emission features, such as the C III 1175 Å multiplet and O I 1305 Å triplet, line up vertically. The narrow trace above the stellar spectrum is the "lamp-flash," a brief exposure of a hollow-cathode calibration source to validate the wavelength zero point.

Blue circles mark features that are dominantly geocoronal: for example, N I 1200 Å and O I 1305 Å in the top panel. Notice, however, that the O I airglow has faded dramatically in the bottom two panels, representing the G130M–1291 splits taken later in the one-orbit visit. In these segments, the oxygen emission dominantly is stellar. Note also the strong Lyα geocoronal features present in the two (lower) 1291 Å panels, but absent in the upper two (1222 Å), thanks to placement of Lyα in the detector a/b gap by design. Also note in the 1291 Å segments the slightly extended Lyα blips in the spectral (horizontal) direction, marked by red angle brackets, on either side of the more circular airglow blob (tracing out the PSA footprint). These in-order features represent extended wings of the stellar H I emission. Other strong stellar features are highlighted by red circles. In addition to the conspicuous emission lines, the HD 22359 spectrum displays a faint long-range continuum, not unexpected given the warm mid-F type. Closer inspection reveals that the continuum trace is slightly more concentrated toward the upper side, indicating that the dominant visual component A is brighter and/or warmer than the less luminous companion B, as expected from evolutionary considerations for a co-eval pair of differing masses. Nevertheless, the AB emission lines themselves appear to be more similar in intensity. (In what follows, the visual binaries were treated as single stars of the combined FUV fluxes and the total system irradiance.)

2.3. COS Spectral Reductions

The spectral reductions proceeded from a series of high-level CALCOS pipeline-processed files for each of the two G130M CENWAVEs. The files called "x1dsum" were a summation of all the FP-POS splits collected for a given CENWAVE. The co-addition process was designed to minimize the influence of detector fixed pattern dropouts and other defects such as gain-sag holes. In addition, subsidiary files were provided, called "x1dsum$\langle n \rangle$," an extracted spectrum for each FP-POS. Here, $n = 3$ or 4 for both the CENWAVEs. All the various types of x1dsum files are populated with quantities extracted from the corresponding flt images, including wavelengths, calibrated fluxes, photometric errors, and data quality flags, as well as the underlying gross, net, and background count rates.

2.3.1. Modified Photometric Error

The CALCOS pipeline assigns a photometric uncertainty to each linearized wavelength bin (see COS Data Handbook V3, §3.4.17) according to a relation following the upper confidence limit (UCL) proposed by Gehrels (1986), based on Poisson statistics for low-count X-ray sources with a negligible background (his eq. 7),

$$\mathrm{UCL} = \mathcal{N} + \Delta\mathcal{N} \ , \tag{1}$$

where,

$$\Delta\mathcal{N} = \sqrt{(\mathcal{N} + \frac{3}{4})} \ + \ 1 \ . \tag{2}$$

Here, $\mathcal{N}$ is the total number of counts recorded in the detection cell over some time interval (the "detected source"), and the upper bound offset, $\Delta\mathcal{N}$, is appropriate to an 84% confidence level ($1\,\sigma$ in a single-sided Gaussian distribution: see Gehrels 1986). There is a companion relation for the lower flux confidence limit. (Ayres (2004) derived similar, slightly more elaborate, expressions for the case where the background is non-negligible.) One can think of the UCL as the largest intrinsic source that could have provided the measured counts $\mathcal{N}$, at the given confidence level, within the context of Poisson fluctuations. Note that even when zero counts are collected in the time interval, i.e., $\mathcal{N} = 0$, the UCL still is 2 counts, indicating that some fraction of the time an intrinsic 2-count source will provide zero counts in the reference time bin, thanks to the counting statistics. The UCL is appropriate to establish the extreme bounding fluxes on, say, a weak X-ray detection in the low-count regime. Note that when the background is very low, capturing just a few counts from a source can be a highly significant detection, but, according to Gehrels, the knowledge of the

intrinsic source flux will be poor (see, also, Ayres 2004). Alternatively, when the counts are high, $\Delta\mathcal{N}$ approaches the $\sqrt{\mathcal{N}}$ standard deviation of Gaussian statistics.

The CALCOS error formulation (expressed in counts) for the net counts N_i in cell i ($N_i \equiv G_i - B_i$, where G_i is the total number of counts collected in the cell, and B_i is the inferred, possibly fractional, background[9]) is analogous to the Gehrels $\Delta\mathcal{N}$ in eq. 1 above:

$$\sigma_{N_i} = \sqrt{(T_i + \frac{3}{4})} \; + \; 1 \;\; , \tag{3}$$

where T_i is a sum of three expressions that account for the various uncertainties associated with collecting the COS counts to establish the net N_i. Importantly, the COS Cross-Delay-Line (XDL) camera of the FUV channel does not have physical pixels like a CCD, so the associated uncertainty is not simply, crudely speaking, the square root of the gross counts in a cell.

The three components of the T_i are as follows. The main one is G_i with a, usually small, correction for the incident photon-to-counts conversion (in)efficiency (the part having to do with small-scale pixel-to-pixel variations and detector dead-time corrections). A second term accounts for the uncertainty in the background correction. The third part is for the uncertainty in the inefficiency factor itself. Helpfully, the COS XDL camera has a very low internal background, and other external background sources in the COS s-FUV channel generally are very small. Thus, the term in T_i for the background correction is small and can be ignored. The component for the inefficiency factor can likewise be shown to be negligible in the low-counts regime (i.e., for faint sources like the EclipSS stars). This leaves just the leading term involving the gross counts. Thus, essentially, the COS error formulation is identical to the $\Delta\mathcal{N}$ in Gehrel's UCL expression. However, Gehrel's derivation was geared toward the conservative characterization of the flux bounds implied by a single X-ray detection in the low-counts regime. This situation is much different than the case of a spectrum, which involves thousands of individual, often correlated, "sources" (e.g., consider a featureless White Dwarf continuum produced by a constant intrinsic f_λ, where the wavelength-arrayed pixel counts only vary according to the counting statistics).

The conservative nature of the COS photometric error is further magnified by the fact that it is assigned on a per pixel basis, and the XDL effective pixels highly oversample the spectral resolution, with about 7 bins per resolution element (resel). The undesirable consequence in the low-counts regime is that a connected series of pixels with zero gross

[9] B_i is derived by collecting background counts in a large enough area outside the cell to yield a significant result, then scaling back to the (much smaller) area of the detect cell.

counts each would individually be given the ∼2 counts minimum error, whereas if the counts were collected over a single resolution element, the error for the super-bin would be just the minimum 2 counts (based on the total of zero gross counts), instead of $2\sqrt{7}$ if the individual pixels were added together, with the errors combined in quadrature.

On both accounts (UCL and oversampled pixels), the CALCOS photometric error is too conservative in the low-counts regime. What would be more helpful, in terms of spectral fitting, is the standard deviation of a flux (hypothetically measured over many trials) as dictated by Poisson statistics (for which the variance is $\mathcal{N}$ for $\mathcal{N} \geq 1$). Thus, for the sake of expediency in the subsequent emission-line fitting, a simplified "spectral" error was introduced for the negligible background case:

$$\sigma_{N_i} = \sqrt{G_i > 1} \ , \tag{4}$$

where G_i is, as before, the gross number of counts collected in the wavelength bin[10], and the inequality is understood to mean the greater of G_i and 1. The flux photometric error, $\sigma_{\rm phot}$, is the above result, in counts, divided by the exposure time and multiplied by a wavelength-dependent "inverse sensitivity" curve. The modified formulation has the desired property that it trivially follows the Poisson variance for all non-zero counts, but has a limiting value for $G = 0$ to avoid divergences in practical quantities like $1/\sigma^2$. The modified photometric error was important for the line-flux measurements described later, especially the weaker spectra, because the more conservative CALCOS version would have negated the significance of legitimate low-S/N detections.

[10]Aside from the limiting value at $G = 0$, this is the same relation (for the low counts regime) in the pre-flight "COS Calibration & Requirements Document" (E. Wilkinson; COS-01-003: 2002 May): $\sigma_{N_i} = \sqrt{T_i}$, in the notation used earlier. The additional, Gehrels-like, constant terms inside and outside the square root were added later, undoubtedly in a burst of conservative statistical zeal.

As mentioned earlier, the COS s-FUV channel spectra are highly over-sampled, with 10 mÅ bins compared to a resel of about 70 mÅ. (The STIS medium-resolution spectra, e.g., of α Cen, are reported with 14 mÅ bins (at 1300 Å) compared to a resel of twice that.) For convenience, the CALCOS x1dsum fluxes were re-binned into 50 mÅ steps, and the photometric error was calculated, as above, for the total gross counts, $G_{\rm sbin}$, associated with the new 50 mÅ super-bin: $\sigma_{\rm sbin} = (\sqrt{G_{\rm sbin} > 1}) \,/\, 5$. Here, the divisor is the resampling factor, which enters because the error in counts is multiplied by the native inverse sensitivity, which, however, is defined for the original, smaller, wavelength pixel.[11]

2.3.2. Merging the CENWAVEs

The CALCOS pipeline was designed to creatively combine the up to four different splits of an observation in a given CENWAVE, recognizing, and ignoring if necessary, intervals corrupted by camera artifacts. However, the pipeline was not trained to eliminate variable geocoronal contamination. This can be an issue, especially at Lyα, but also at the O I 1305 Å triplet (e.g., Fig. 3), and to a lesser extent at the N I 1200 Å multiplet.

Thus, a specialized combination of the various full and partial x1dsum files was concocted to minimize the airglow effects. The N I 1200 Å region was not crucial to the objectives of the program, so was treated with a simplistic rationale to accept the one of the four possible splits in that interval (considering the overlapping CENWAVEs) that had the lowest average intensity, indicating the least geocoronal contamination. H I 1215 Å was more important, but, realistically, extracting useful stellar information from the over-exposed Lyα geocoronal feature was pretty much hopeless, and there were only two splits to work with in any event. The situation was more hopeful for the diagnostically important chromospheric O I 1305 Å triplet where the airglow emissions more dramatically subside during orbital night, and there were four possible grating splits from which to choose one, or possibly

[11]As this paper was being finalized, the COS team released a revised version of the CALCOS pipeline, in which a new error estimation algorithm was introduced (COS STScI Analysis Newsletter, October 2020). However, the new implementation mainly corrects subtle errors in the original software (having to do with propagation of errors from the individual splits into the final x1dsum), but still retains the original Gehrels Upper Confidence Limit formulation (although now providing the companion Lower Confidence Limit as well). The new implementation is improved in some respects, but does not alleviate the philosophical tension between the UCL and the flux dispersion as far as spectral fitting is concerned, and still suffers from the consequences of the "over-sampled pixel syndrome" described earlier. The COS STAN also announced a new time-dependent flux correction, to better follow the slowly fading FUV detector sensitivity. The implementation mainly concerns the period after mid-2019, and thus does not affect EclipSS, for which the majority of observations were in 2018, with a few extending into the first quarter of 2019.

more, low-airglow spectra. An algorithm was developed to assess the strength of the oxygen emissions in each grating split, then decide which to accept in a local average to achieve the minimum airglow contamination. Three of the targets were too contaminated to qualify any of their splits. At the other extreme, there were cases where as many as 3, or even all 4, of the FP-POS were deemed acceptable, displaying consistently low oxygen emissions. For the majority (~ 70 %) of the targets, however, only one or two splits were worth saving.

Figure 4 illustrates the reduction strategy for HD 156389, the other instance of a visual binary with near-equal components fitting inside the COS PSA. The two panels display the full spectral range of the combined G130M–1222 and G130M–1291 settings, and their associated FP-POS pairs. Three spectra are depicted: blue for CENWAVE 1222 Å, red for 1291 Å, and a darker curve for the sum, weighted by a smoothed $1/\sigma^2_{\rm phot}$ in the overlap regions, and including cutouts for the airglow intervals, which were separately treated as described above. Gray shading traces out the maximum of the O I 1302–1306 Å airglow contamination, while yellow shading indicates the consensus low-airglow line shapes. (Similar tagging was applied to Lyα, although it never achieved truly airglow-free status in any of the EclipSS visits.) The thin dotted-dashed tracing above the spectrum represents the $10\,\sigma$ photometric error, based on the streamlined σ_λ formulation described earlier, weighted between the two CENWAVEs if appropriate and heavily smoothed for display purposes. Slight discontinuities in the photometric error are evident in a number of places, highlighting gaps where only one of the CENWAVEs contributed. Inset panels illustrate the individual x1dsum splits in the vicinity of the conspicuous airglow features noted earlier. In these panels, small $\times$s indicate flagged defects, such as the gain-sag hole in the middle of the Lyα feature of one of the G130M–1291 FP-POS (darker profile). Another camera artifact is seen as a sharp downward spike in the orange airglow-dominated curve in the O I triplet inset panel. In that case, only one of the G130M splits was deemed satisfactory from a low-airglow perspective (lower darker curve). The number of low-airglow splits identified for each target is listed in Table 2.

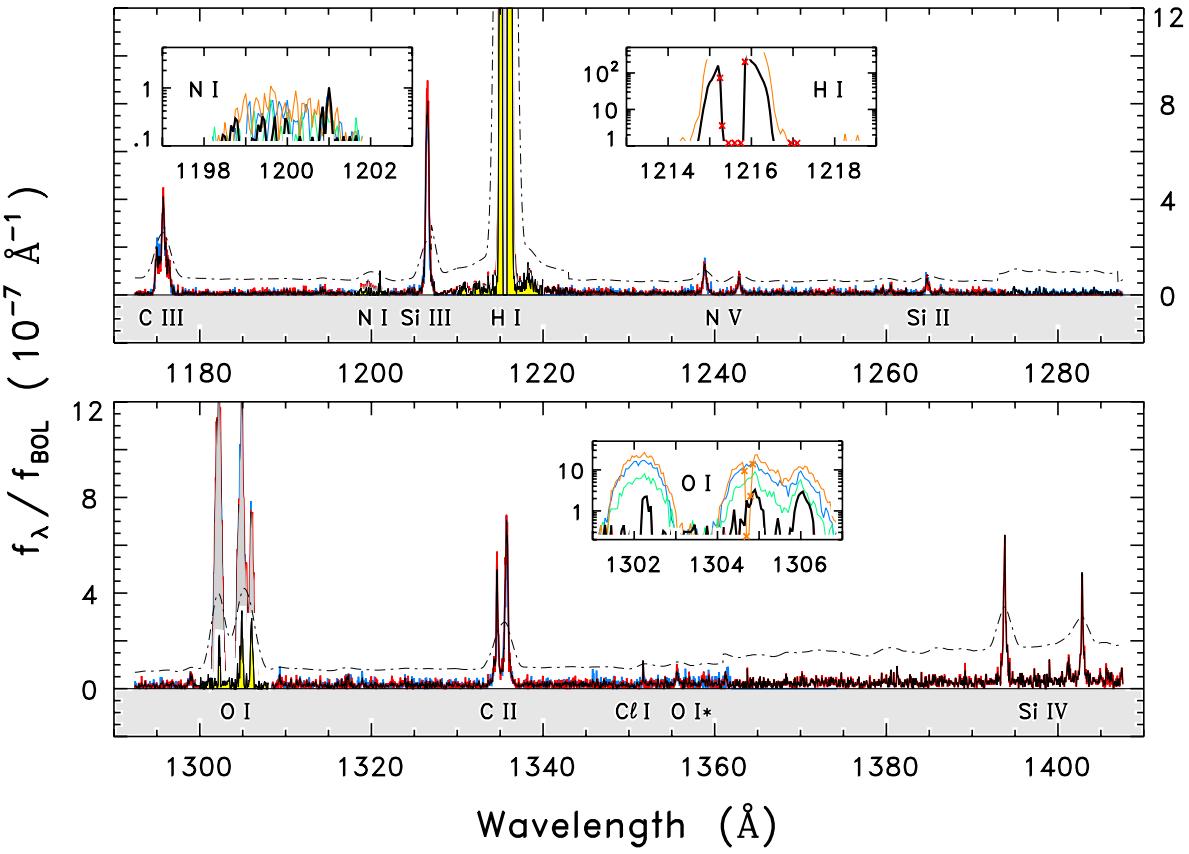

Fig. 4.— Schematic rendering of the spectral reduction procedure for HD 156389, merging the G130M-1222 (blue) and G130M-1222 (red) FP-POS splits (darker tracing is the sum). Inset panels illustrate the empirical compensation for geocoronal airglow by only retaining the splits showing minimal contamination. Gray-shaded O I emissions, on the left side of the lower panel, indicate the amplitude of the features without correcting for the airglow contamination. Yellow-shaded profiles are the result of selecting the minimum airglow-affected features from the four independent splits (in this case only one qualified). The H I Lyα interval was too contaminated to correct, and suffered from a significant gain-sag hole in one of the splits. Nevertheless, genuine stellar emission could be recovered in the Lyα wings on either side of the geocoronal core. The thin dotted-dashed curve is the smoothed $10\,\sigma$ photometric error.

2.4. Flux Measurements

In Paper I, emission line strengths were derived from the daily SORCE/SOLSTICE low-resolution ($\lambda/\Delta\lambda \sim$ 1,500) FUV irradiance scans by numerically integrating the flux densities in fixed wavelength bands. The strategy was expedient for the FUV because there were relatively few blends of any consequence in the bright lines, even with the considerable instrumental broadening of the solar scanner. A self-consistent approach was applied to the higher resolution ($\lambda/\Delta\lambda \sim$ 40,000) spectra of α Cen AB, from HST/STIS, using the same broad bandpasses for the stellar features as used for the partially blended solar counterparts (e.g., O I 1304 Å +1306 Å, and C II 1334 Å + 1335 Å).

In the present study, the EclipSS spectra were recorded by moderate-resolution COS G130M ($\lambda/\Delta\lambda \sim$ 18,000), which fully resolves the important stellar s-FUV features. It was decided to still retain the numerical integration scheme for the line fluxes (especially since many of the features have distorted, non-Gaussian line shapes, including interstellar absorptions in some cases), but now tailor the integration bandpasses to better match the resolution capabilities of the companion HST instruments, COS for EclipSS and STIS for α Cen AB. A key consideration was to separate features like O I 1302 Å, 1304 Å, and 1306 Å, which are differentially affected by atomic oxygen airglow in COS; and C II 1334 Å and 1335 Å, for which interstellar C^+ more strongly absorbs the ground-state transition (1334 Å) in all the stars. However, the pursuit of higher resolution for the stellar fluxes, now fitting individual lines rather than blends of the same species, meant that the corresponding low-resolution solar fluxes derived in Paper I for multi-line combinations had to be translated into the single-line equivalents. The high-resolution STIS spectra of solar twin α Cen A, and s-FUV spectra from the solar Interface Region Imaging Spectrograph (IRIS: see Paper I), were put to good use for this purpose, as described later.

Figure 5(a) depicts the numerical integration scheme for epoch-average α Cen AB spectra exclusively from the STIS E140M–1425 medium-echelle setting ($\lambda/\Delta\lambda \sim$ 40,000), achieving more than twice the resolution of COS in the s-FUV, and very high signal-to-noise given the brightness of these nearby stars. The collection of STIS α Cen observations was described in detail in Paper I, but the datasets were reprocessed for the present study owing to the introduction of new CALSTIS reference files, some relevant to the radiometric calibration, in the interim. Each of the sub-panels of Fig. 5(a) illustrates profiles of a selected s-FUV emission line, shaded for solar-twin α Cen A, un-shaded for (slightly more active) α Cen B, and displayed on a relative $f_\lambda/f_{\rm BOL}$ scale normalized to the peak of the B spectrum in that sub-panel. The features of both stars were corrected for the respective stellar radial velocities (which differ slightly because of the relative binary orbital motion).

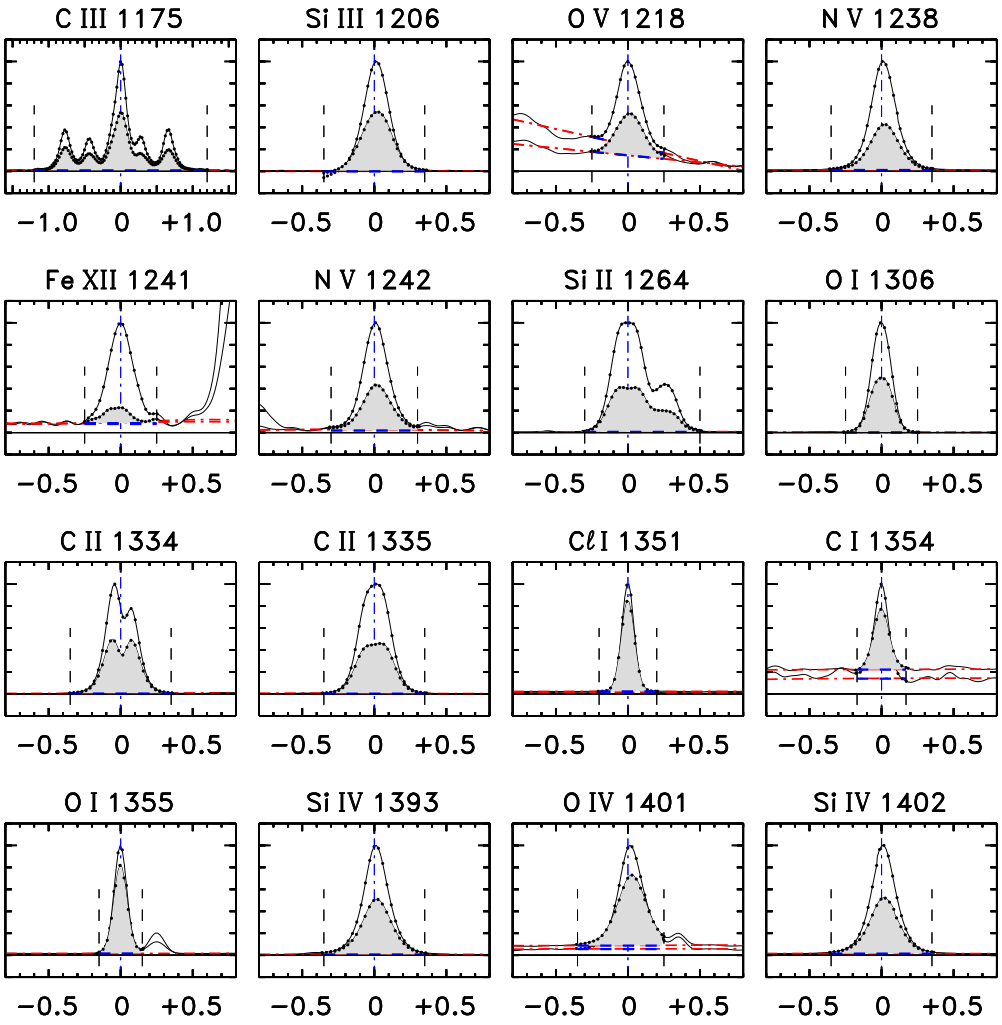
C III 1175
Si III 1206
O V 1218
N V 1238
Fe XII 1241
N V 1242
Si II 1264
O I 1306
C II 1334
C II 1335
Cℓ I 1351
C I 1354
O I 1355
Si IV 1393
O IV 1401
Si IV 1402
−1.0 0 +1.0
−0.5 0 +0.5

Fig. 5(a).—

Fig. 5.— (a) Illustration of the spectral measurement procedure for α Cen. Shaded profiles are for solar twin A; un-shaded for more active companion B. A thin vertical dotted-dashed line marks the laboratory line center; dashed lines on either side indicate limits of the flux integration. Red curves, where visible are long-range continuum fits; thicker blue dashed lines (possibly slanted) are the continuum levels adopted for the particular species. (b) For the EclipSS targets. Shaded profiles are for an average of low-activity sample members; open profiles for a high-activity average. Note the prominent Fe XXI 1354 Å emission ($T \sim 10$ MK) of the latter; and the asymmetry of the C II 1334 Å resonance lines, especially in the high-activity case, caused by interstellar C^+ absorption. Vertical dashed lines again mark the flux integration limits, but now there are two sets for several of the species (e.g., Si III 1206 Å) that display extended profile wings.

Most of the emission lines in Fig. 5(a) were previously utilized in Paper I, especially the important high-temperature s-FUV species C III, Si III, N V, and Si IV. But, with the higher resolution of COS for the EclipSS stars compared with SOLSTICE for the Sun, additional diagnostics became accessible. One example is O I 1306 Å, longward component of the O I triplet, blended in SOLSTICE with O I 1304 Å, but the most favored O I line for COS because it is least affected by oxygen airglow and ISM absorption. Other examples are O V 1218 Å, in the red wing of Lyα, too blended in the SOLSTICE scans; faint Fe XII 1241 Å coronal forbidden line, obscured by stronger N V 1242 Å in SOLSTICE (and nearly 3 times stronger than subsidiary, but more isolated component Fe XII 1349 Å which was, just barely, measurable in SOLSTICE); and density-sensitive O IV 1401 Å, also low contrast, and in the shadow of Si IV 1402 Å in SOLSTICE. The Si II 1264 Å doublet was added here as a representative chromospheric feature from a low first-ionization potential ("FIP") species, to counter the loss of key NUV Mg II 2800 Å, which could not be included in the EclipSS program owing to the limited observing time available, as well as failing sensitivity of the COS G285M channel. (For the similar reason of limited observing time, the long-FUV interval, 1420–1700 Å could not be observed in EclipSS, thereby unfortunately excluding the important C IV 1548 Å + 1551 Å doublet and He II 1640 Å Balmer-α. However, the s-FUV is much richer in diagnostics, so the loss of the longer FUV wavelengths was minor.)

The addition of narrow, weak chromospheric C I 1354 Å might seem like an odd choice, but the carbon line coincides with a key coronal forbidden transition—Fe XXI 1354 Å ($T \sim 10$ MK)—a solar "flare line" that appears in a few of the most active of the EclipSS stars, and for which the C I line is a contaminant. The behavior of the C I feature versus more isolated chromospheric features, like O I 1306 Å, especially in higher activity α Cen B, could potentially provide a correction for this contamination in the more extreme cases showing significant Fe XXI. A few other potentially accessible s-FUV features, like Fe XII 1349 Å (as mentioned earlier, intrinsically about 3 times weaker than 1241 Å, but more isolated and near the peak of the G130M sensitivity) and semi-permitted O V 1371 Å, were investigated, but found to be too faint for useful measurements in the majority of the EclipSS stars, so were not considered further, especially since other brighter features of the same ions already were available.

In Fig. 5(a), red dotted-dashed curves (not always visible) represent estimated continuum levels based on a long-range hierarchical filtering scheme described in Paper I. The same filter parameters were applied to the STIS spectra of α Cen AB and the (resampled) COS spectra of EclipSS: running median of 71 bins, minimum filter of 101 bins, and boxcar of 71 bins (see Paper I for details). There was an additional slight modification here for O V 1218 Å and coronal forbidden line Fe XII 1241 Å to account for possibly sloping backgrounds contributed by wings of nearby stronger emissions (H I Lyα and N V 1242, respectively).

A blue dashed line indicates the specific local value of the continuum level adopted for the integrated flux measurement; constant across the feature in most instances, but slanted for the two sloping background cases. In each panel, a thin blue vertical dotted-dashed line marks the adopted (laboratory) line center, and two flanking vertical dashed lines indicate the blue ("B") and red ("R") wavelength limits, possibly asymmetric, between which the net fluxes (above the local continuum level) were integrated (dark dots are the included points). The associated pixel photometric errors were combined in quadrature across the feature, compatible with the numerical integration of the flux densities, and, for simplicity, the potential uncertainty in the background fit was ignored.

Table 3 summarizes the emission line fitting parameters for α Cen AB (which also apply to the EclipSS stars with an important exception noted below). The column "$\log T_{\rm MAX}$" lists temperatures of maximum species concentration (in collisional ionization equilibrium) from CHIANTI (Dere et al. 2019), mainly for the higher excitation, optically thin features. Also included are estimates for the lower excitation, thicker resonance lines of the upper chromosphere, as well as the optically thin, lower excitation species, which tend to form deeper in the atmosphere at reduced temperatures.

Note in Fig. 5(a) that the low-excitation, narrow, likely optically thin chromospheric emissions of Cl I 1351 Å, C I 1354 Å, and O I 1355 Å have similar $f_{\rm L}/f_{\rm BOL}$ ratios in both α Cen stars, but the optically thick chromospheric species, Si II 1264 Å and O I 1306 Å, are significantly stronger in the K dwarf. The latter chromospheric difference extends to the higher ionization sub-coronal species like Si III, Si IV, and N V. The excitation disparity between A and B peaks at the Fe XII 1241 Å forbidden line, which apparently is more favored in B thanks to its hotter corona (see, e.g., Ayres 2014).

Figure 5(b) is similar to Fig. 5(a), for the COS EclipSS stars. As in Fig. 5(a), two sets of profiles are displayed in each sub-panel. The lower, shaded feature is a co-addition of nine low-activity members of the sample, while the higher, open profile is an average of five of the more active dwarfs[12]. The selected high-activity candidates avoided some of the most active stars of the sample: early-F stars that either had excessive rotational broadening (HD 156559), or significant s-FUV continuum emission, which, for display purposes, undesirably reduced the apparent line contrasts.

[12]HD numbers of low-activity sub-sample: 20052, 47252, 73744, 144061, 146868, 159329, 168093, 187876, 202123; high-activity sub-sample: 38459, 41004, 62850, 150706, 185239.

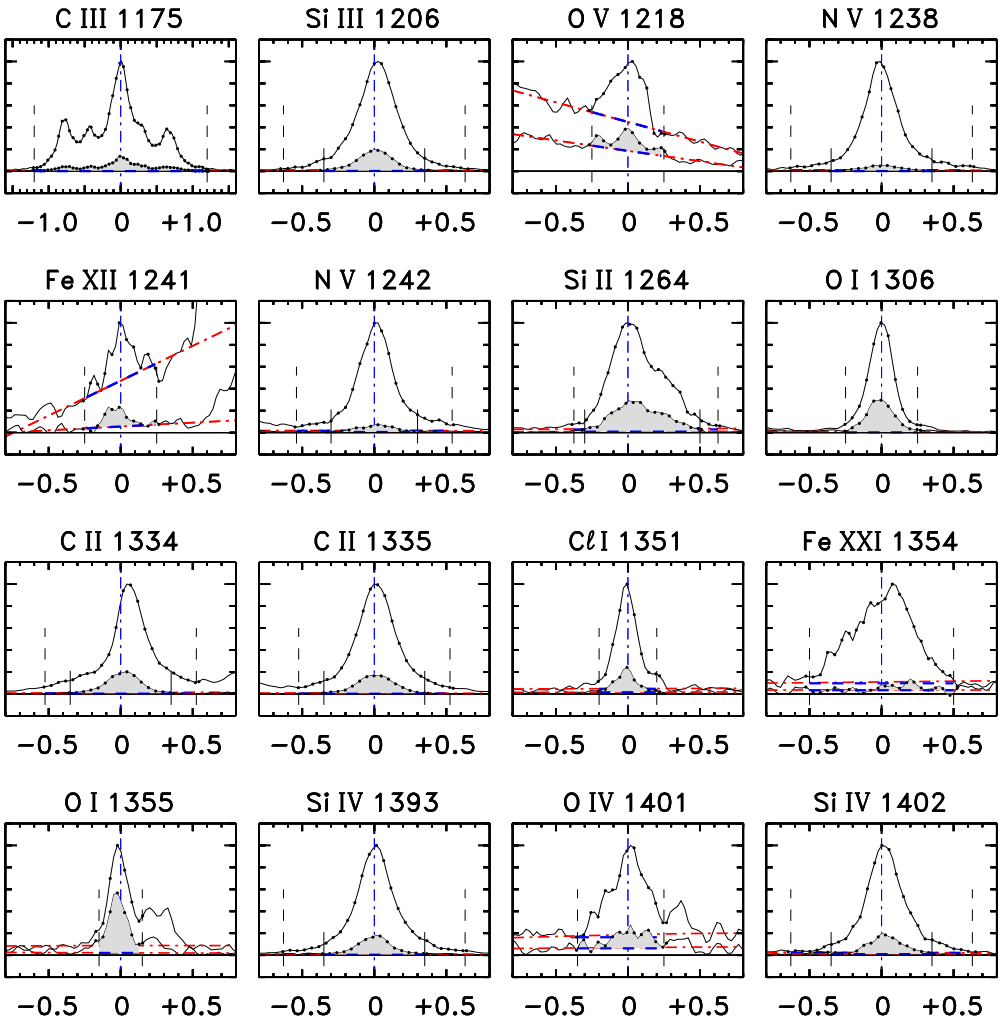
C III 1175
Si III 1206
O V 1218
N V 1238
Fe XII 1241
N V 1242
Si II 1264
O I 1306
C II 1334
C II 1335
Cℓ I 1351
Fe XXI 1354
O I 1355
Si IV 1393
O IV 1401
Si IV 1402
−1.0 0 +1.0
−0.5 0 +0.5

Fig. 5(b).—

Table 3. Line Flux Integration Parameters

Feature	$\lambda_{\rm LAB}$ (Å)	$\log T_{\rm MAX}$ (K)	$(\Delta\lambda_{\rm B}, \Delta\lambda_{\rm R})$ (Å)	$\rho_\star$
1	2	3	4	5
C III 1175	1175.711	4.8	(1.20, 1.20)	0.00
Si III 1206	1206.500	4.7	(0.35, 0.35)	0.80
O V 1218	1218.344	5.3	(0.25, 0.25)	0.00
N V 1238	1238.810	5.2	(0.35, 0.35)	0.80
Fe XII 1241	1241.985[a]	6.2	(0.25, 0.25)	0.00
N V 1242	1242.800	5.2	(0.30, 0.30)	0.80
Si II 1264	1264.738	(3.9)	(0.30, 0.50)	0.25
O I 1306	1306.029	(3.9)	(0.25, 0.25)	0.00
C II 1334	1334.532	4.5	(0.35, 0.35)	0.50
C II 1335	1335.702	4.5	(0.35, 0.35)	0.50
Cl I 1351	1351.656	(3.8)	(0.20, 0.20)	0.00
Fe XXI 1354	1354.10	7.1	(0.50, 0.50)	0.00
C I 1354	1354.288	(3.8)	(0.17, 0.17)	0.00
O I 1355	1355.598	(3.8)	(0.15, 0.15)	0.00
Si IV 1393	1393.760	4.9	(0.35, 0.35)	0.80
O IV 1401	1401.157	5.1	(0.35, 0.25)	0.00
Si IV 1402	1402.773	4.9	(0.35, 0.35)	0.80

Note. — Col. 1 is the short name of the feature. Col. 2 is the laboratory wavelength (mainly from Ayres 2015: especially N V and Si IV), but Atomic Line List v2.05b21 (see: https://www.pa.uky.edu/∼peter/newpage/) otherwise, except as noted for Fe XII 1241 Å). Col. 3 is the approximate temperature of maximum emissivity from CHIANTI (see: https://www.chiantidatabase.org/chianti_linelist.html); parenthetical values are estimates for species that form in the

chromosphere. Flux integration bandpass (Col. 4) is ($\lambda_{\rm LAB} - \Delta\lambda_{\rm B}$) to ($\lambda_{\rm LAB} + \Delta\lambda_{\rm R}$). For the several stars with unusually broad lines, especially the high-activity cohort and mainly their high-temperature species, the Col. 4 wavelength limits were boosted by the factor $(1 + \rho_\star)$, where $\rho_\star$ is listed in Col. 5. The specific BL stars were highlighted previously in Table 2 (Col. 8). In the unique case of HD 156559, even the low-excitation chromospheric lines are broad thanks to extreme $v \sin i$, so the integration bandpasses were opened up to ±0.7 Å, except for the already spread-out C III 1175 Å multiplet where ±1.4 Å was used.

[a]Empirical value based on epoch-average α Cen B STIS spectrum.

In each panel, the high-activity profile was normalized to its peak flux density, $f_{\rm max}^{\rm hi-act}$, while the companion low-activity feature was scaled to the same $f_{\rm max}^{\rm hi-act}$ to provide a relative comparison. Here, the s-FUV emission contrast between the low-activity and high-activity objects is much more pronounced than for α Cen AB. Note, for example, the strong Fe XXI 1354 Å feature in the active average, compared with essentially noise in the corresponding low-activity tracing (although with possible weak C I 1354 Å emission at +0.2 Å); and the N V resonance lines (1238 Å + 1242 Å), where the low-activity counterpart barely is visible. Also note the asymmetric profile of C II 1334 Å in both the active and quiet averages, more evident in the former, presumably due to ISM absorption. A more subtle effect is seen in the O I 1355 Å panel with regard to the weak blend on the red shoulder of the semi-permitted ground-state oxygen line. The blend is a moderate-excitation permitted C I transition, 1.26 eV above ground, probably mainly formed by recombination (Lin et al. 2017). Note that the carbon line is much brighter in the active average relative to O I, compared with the quiet average. This effect might be a consequence of enhanced Lyα photoionization of carbon (see, e.g., ibid).

As in Fig. 5(a), vertical dotted-dashed lines in Fig. 5(b) mark the adopted line centers, while flanking dashed lines delimit the integration bandpasses. For the EclipSS case, however, two sets of integration bandpasses ("quiet" (inner pair) and "active" (outer)) appear for several of the features—moderate temperature C II and Si III, and higher temperature Si IV and N V—which show extended emission wings in the high-activity sample members, a curious characteristic of active stars that highlights the role of gas-dynamic processes in the magnetically impacted outer atmospheres (e.g., Ayres et al. 2007). Table 3 lists the additional fitting parameter (called "$\rho_\star$") to accommodate the extra broadening.

Table 4 summarizes integrated flux measurements, in $f_{\rm L}/f_{\rm BOL}$ units, for the COS EclipSS stars, the epoch-average STIS spectra of α Cen AB, and the SOLSTICE scans for solar Cycle 23/24 MIN (2008.7±0.3) and MAX (2014.9±0.1). (Note: Cycle 24 was unusually weak compared with other sunspot cycles over the past 50 years). Only the strongest lines that appear in a majority of the stars are listed. For the SOLSTICE combinations O I 1304 Å + 1306 Å and C II 1334 Å + 1335 Å, the single-line equivalents, O I 1306 Å and C II 1335 Å, respectively, were derived from the solar blends by applying a factor 0.524 for O I, as deduced from high-resolution STIS spectra of the solar-twin α Cen A; and 0.566 for C II, derived from an equally high-resolution IRIS solar pseudo-disk-average (see Paper I, Fig. 3). The latter closely matches the α Cen A spectrum in relative flux density, aside from the conspicuous ISM absorption dip in the stellar 1334 Å resonance component. (This was why the α Cen A spectrum could not be used for the C II ratio; however, the O I 1304 Å and 1306 Å components are less affected by ISM absorption, and, in any event, the IRIS wavelength coverage does not extend below 1330 Å.)

Table 4. Main Spectral Features: Bolometrically Normalized Line Fluxes (f_L/f_{BOL} (10^{-7}))

Star Name	Type	C III 1175	Si III 1206	N V 1240	Si II 1264	O I 1306	C II 1335	Cl I 1351	O I 1355	Si IV 1400
1	2	3	4	5	6	7	8	9	10	11
Sun (MIN)[a]	G2	0.36	0.57	0.125	···	0.31	0.63	0.040	···	0.41
Sun (MAX)[b]	G2	0.47	0.95	0.166	···	0.37	0.87	0.046	···	0.62
HD 128620[c]	G2	0.388	0.685	0.151	0.114	0.323	0.715	0.046	0.070	0.526
HD 128621[d]	K1	0.661	1.057	0.315	0.242	0.566	1.343	0.052	0.082	0.903
HD 20052	G0	0.34	0.45	0.15	0.08	0.28	0.63	0.06	0.06	0.52
HD 21166	F4	1.11	1.06	0.32	0.10	0.66	1.03	0.11	0.13	1.13
HD 22359	F6	0.74	0.94	0.20	0.12	0.35	0.91	0.05	0.08	0.97
HD 24293	G3	0.32	0.49	0.13	0.08	0.32	0.53	0.04	0.07	0.38
HD 24636	F3	8.5	9.4	2.39	0.45	1.48	8.2	0.37	0.18	8.5
HD 28471	G3	0.32	0.54	0.10	0.07	0.24	0.48	< 0.03	0.04	0.39
HD 28481	F7	0.37	0.54	0.11	0.10	0.35	0.57	< 0.04	0.06	0.5
HD 28701	G3	0.25	0.35	0.04	0.09	0.32	0.40	0.03	0.10	0.35
HD 29255	F7	1.0	1.21	0.29	0.09	0.43	1.11	0.08	0.10	1.2
HD 30501	K2	1.48	1.87	0.61	0.43	1.08	2.64	0.10	0.14	1.68
HD 32778	G3	0.19	0.22	0.05	0.07	0.27	0.26	0.021	0.040	0.23
HD 34297	G4	0.19	0.28	0.04	0.07	0.40	0.31	0.023	0.07	0.24
HD 36767	F9	0.34	0.43	0.07	0.08	0.29	0.51	0.04	0.05	0.31
HD 38459	K0	3.3	4.8	1.86	0.72	2.1	5.5	0.26	0.12	5.2
HD 39194	G8	0.14	0.27	0.06	0.06	0.31	0.30	< 0.03	0.05	0.29
HD 39755	F3	9.1	9.6	2.26	0.51	1.4	7.9	0.34	0.15	10.0
HD 41004	K3	19.9	11.1	16.0	1.14	5.0	22.8	0.58	0.52	10.6
HD 42286	K2	0.37	0.46	0.12	0.14	0.39	0.59	< 0.04	0.04	0.43
HD 47252	G9	0.39	0.60	0.12	0.11	0.45	0.74	< 0.03	0.07	0.57

Table 4—Continued

Star Name	Type	C III 1175	Si III 1206	N V 1240	Si II 1264	O I 1306	C II 1335	Cl I 1351	O I 1355	Si IV 1400
1	2	3	4	5	6	7	8	9	10	11
HD 51608	G8	0.40	0.59	0.12	0.21	0.46	0.76	< 0.03	0.06	0.78
HD 51929	G1	0.22	0.30	0.04	0.09	0.26	0.31	0.03	0.06	0.26
HD 53658	F6	0.40	0.42	0.07	0.07	0.32	0.53	0.08	0.07	0.44
HD 55720	G5	0.27	0.36	0.08	0.07	0.31	0.48	0.03	0.07	0.32
HD 56737	F5	0.71	0.68	0.14	0.09	0.37	0.67	0.06	0.09	0.71
HD 62850	G2	6.2	12.5	2.74	1.11	2.45	8.1	0.37	0.25	13.3
HD 63765	G6	1.09	1.61	0.35	0.27	0.69	1.83	0.08	0.08	1.5
HD 64184	G4	0.77	0.90	0.19	0.16	···	1.02	0.05	0.12	0.75
HD 73744	G2	0.55	0.92	0.15	0.15	0.46	0.79	0.03	0.07	0.81
HD 137826	G5	0.3	0.34	< 0.08	0.07	0.3	0.47	< 0.05	0.07	0.4
HD 144061	G2	0.53	0.84	0.11	0.12	0.45	0.73	0.03	0.05	0.77
HD 146044	G5	0.34	0.36	0.09	0.10	0.38	0.52	< 0.03	0.07	0.24
HD 146868	G4	0.40	0.66	0.11	0.13	0.34	0.64	0.02	0.04	0.54
HD 147231	G5	0.31	0.49	0.07	0.08	0.36	0.58	0.03	0.07	0.31
HD 150706	G1	3.09	6.63	1.00	0.72	1.38	4.50	0.17	0.13	6.0
HD 151541	G8	0.21	0.27	0.07	0.09	0.25	0.37	< 0.02	0.06	0.31
HD 154956	F8	0.26	0.40	0.08	< 0.04	0.33	0.33	< 0.04	0.07	0.31
HD 156389	F6	3.4	3.8	0.85	0.26	0.79	3.0	0.12	0.11	3.5
HD 156559	F3	7.2	7.0	1.64	0.34	2.7	5.8	0.39	0.24	7.0
HD 159329	G0	0.36	0.67	0.13	0.09	0.46	0.56	0.04	0.05	0.60
HD 161897	G5	0.99	2.19	0.36	0.32	0.81	1.89	0.07	0.09	1.70
HD 165700	F8	0.23	0.26	0.07	0.05	0.33	0.24	0.05	0.05	0.24
HD 168093	F9	0.31	0.40	0.09	0.09	0.32	0.48	0.04	0.08	0.45
HD 172669	G2	1.12	2.27	0.34	0.32	0.58	1.51	0.06	0.05	2.13

Table 4—Continued

Star Name	Type	C III 1175	Si III 1206	N V 1240	Si II 1264	O I 1306	C II 1335	Cl I 1351	O I 1355	Si IV 1400
1	2	3	4	5	6	7	8	9	10	11
HD 180712	G1	1.19	2.44	0.29	0.29	···	1.63	0.07	0.09	2.1
HD 185239	F5	4.8	5.7	1.43	0.36	1.6	4.9	0.32	0.20	5.6
HD 187876	G0	0.45	0.59	0.11	0.09	0.26	0.77	0.05	0.08	0.52
HD 199476	G5	0.22	0.31	0.06	0.06	0.27	0.37	0.03	0.08	0.25
HD 201651	G7	0.23	0.34	0.07	0.09	···	0.39	0.03	0.05	0.29
HD 202123	K1	0.32	0.57	0.07	0.11	0.5	0.59	< 0.05	0.08	0.4

Note. — The bolometrically normalized fluxes are in units of 10^{-7}. Upper limits are $3\,\sigma$. Otherwise, listed fluxes are more significant than $3\,\sigma$, and the numerical values are presented such that the $1\,\sigma$ uncertainties are less than a few units in the last reported decimal place. Null entries in the leading solar rows refer to species that were not measured in the SOLSTICE scans. A null entry in the O I 1306 column indicates that all four of the G130M spectral splits of that star were contaminated by oxygen airglow.

[a] 2008.7±0.3 (interval at Cycle 23/24 minimum)

[b] 2014.9±0.1 (interval near Cycle 24 maximum)

[c] α Cen A

[d] α Cen B

Table 5 is a shorter list of—typically the most active—EclipSS stars, for which the more exotic, weaker, features were detected, such as the coronal forbidden lines, semi-permitted O V 1218 Å, and O IV 1401 Å. Only targets for which at least two of the four features were detected at $>3\,\sigma$ were included in the list. None of these lines were measurable in the Sun due to blending (although the $\sim$3 times weaker Fe XII 1349 Å component was reported in the SOLSTICE time series of Paper I). In the case of α Cen AB, the entry in the Fe XXI column is C I 1354 Å, which can be a source of contamination for Fe XXI in the more active stars (see Ayres et al. 2003).

Table 5. Subsidiary Spectral Features: Bolometrically Normalized Line Fluxes (f_L/f_{BOL} (10^{-7}))

Star Name	Type	O V-1218	Fe XII-1241	Fe XXI-1354	O IV-1401
1	2	3	4	5	6
HD 128620[a]	G2	0.077	0.004	(0.004)[c]	0.038
HD 128621[b]	K1	0.131	0.026	(0.006)[c]	0.049
HD 21166	F4	0.23	< 0.02	< 0.05	0.16
HD 22359	F6	0.15	< 0.02	< 0.04	0.08
HD 24636	F3	0.8	< 0.03	< 0.07	0.44
HD 30501	K2	0.31	0.04	< 0.03	0.09
HD 36767	F9	0.09	< 0.01	< 0.02	0.04
HD 38459	K0	0.7	0.13	0.10	0.15
HD 39755	F3	0.8	< 0.05	0.11	0.4
HD 41004	K3	1.1	< 0.1	2.0	0.5
HD 56737	F5	0.10	< 0.02	0.05	0.10
HD 62850	G2	0.7	0.05	0.22	0.31
HD 63765	G6	0.3	< 0.03	< 0.05	0.10
HD 64184	G4	0.12	< 0.02	0.03	0.06
HD 144061	G2	0.17	< 0.01	< 0.02	0.03
HD 147231	G5	0.14	< 0.02	< 0.04	0.08
HD 150706	G1	0.29	0.05	0.06	0.19
HD 156389	F6	0.13	< 0.03	0.07	0.23
HD 156559	F3	0.4	< 0.07	< 0.1	0.3
HD 161897	G5	0.23	< 0.02	< 0.03	0.09
HD 172669	G2	0.15	0.04	< 0.03	0.08
HD 180712	G1	0.2	< 0.03	< 0.05	0.09
HD 185239	F5	0.3	< 0.05	< 0.08	0.27
HD 187876	G0	0.13	< 0.02	< 0.04	0.07
HD 199476	G5	0.14	< 0.02	< 0.04	0.05

Note. — The bolometrically normalized fluxes are in units of 10^{-7}. Upper limits are $3\,\sigma$. Otherwise, listed fluxes are more significant than $3\,\sigma$, and the numerical values are presented such that the $1\,\sigma$ uncertainties are less than a few units in the last reported decimal place. The Sun is not included because all the target lines were too blended in the SOLSTICE scans.

[a] α Cen A

[b] α Cen B

[c] C I 1354 Å, possible contaminant of Fe XXI 1354 Å.

3. ANALYSIS

The following sections present the main empirical results of the EclipSS study, based on the spectral measurements described earlier. In what follows, bracketed quantities refer to logarithmic normalized fluxes: $[\mathrm{Y}] \equiv \log\left(f_{\mathrm{Y}}/f_{\mathrm{BOL}}\right)$, for species "Y". Note also—relevant to the figures presented in the next section—that the y-axis might be a difference of bracketed quantities, so that, for example, $[\mathrm{Y}]-[\mathrm{Z}]$ would refer to the (logarithmic) ratio of the original fluxes "Y" and "Z."

3.1. Comparisons of Selected Line Ratios

3.1.1. C II 1334 Å versus C II 1335 Å

The first comparison, shown in Figure 6(a), displays the ratio of the two main components of the C II multiplet, 1334 Å and 1335 Å, as a function of stellar distance. As mentioned earlier, the ground-state resonance transition, 1334 Å, is more severely affected by interstellar absorption than the excited-state counterpart, 1335 Å[13], consequently a dependence of the ratio on distance might be anticipated. The EclipSS dots—restricted to $\geq 7\,\sigma$ detections of both C II components to ensure a $\geq 5\,\sigma$ ratio—are color-coded according to the legend in Fig. 2, namely the yellow symbols are for the Sun-like spectral types, green for the warmer stars, and orange for the cooler. The corresponding C II ratios for α Cen AB, over their magnetic cycles, are depicted as blue dots for A and red for B in the cutout panel at upper left. The inset panel at lower right is a flux–flux diagram for 1334 Å versus 1335 Å, illustrating the range of intensity variations of the α Cen stars over their respective cycles, and further that the two components are in a 1:1 relationship (the dashed lines are power laws with slopes $\alpha = 0.5$ (bottom), 1, 2, and 3 (top)). The EclipSS points are marked according to Ecliptic pole. The shaded horizontal band at the top of the diagram is the solar ratio deduced from the IRIS pseudo-disk-average mentioned earlier. The thinner horizontal dashed line at a logarithmic ratio of -0.2 represents the average C II ratio of α Cen A. The offset between the solar and α Cen A values presumably is related to local ISM absorption by C^+ over that (short) sightline. (The small additional displacement of the average α Cen B ratio likely is an excitation effect, given the somewhat more active nature of the K dwarf.)

---

[13]The 1335 Å component itself is a blend of 1335.66 Å and 1335.71 Å, both arising 63 cm^{-1} above ground and differing by a factor of 9 in absorption line strength gf (lower-level statistical weight, g, times the oscillator strength, f; 1335.71 Å is the stronger of the two). The ground-state transition, 1334.53 Å, has a gf about 60 % that of 1335.71 Å.

Although the initial anticipation was for a systematic trend of decreasing C II ratio with distance, in step with increasing interstellar columns, the observed ratios run contrary to that expectation. Several of the stars show higher ratios than α Cen A, infringing on the solar ISM-free value in a few cases (though not exceeding that limit). That is curious, given that the average EclipSS star is 30 times further away than α Cen. To be sure, the majority of the EclipSS stars do display smaller ratios than α Cen AB, although the points are scattered and no obvious trend with distance is evident.

The main systematic effect is that most of the values below -0.4 are in the Ecliptic South pole. Linsky et al. (2019) identified a region of low neutral hydrogen column (the "Hydrogen Hole") and a high ionization, geometrically thin "Blue Cloud" (possibly a Strömgren shell) in the ISM toward that direction, which could account for the increased absorption in C^+. In this case, the (photo-)ionization is caused by relatively nearby hot stars ϵ CMa and β CMa, and very nearby α CMa. In the authors' ISM map, the North Ecliptic pole falls near the edge of the so-called "Local Interstellar Cloud" (LIC), which apparently extends only a few pc from the Sun, mainly on the anti-Galactic-Center side, and has characteristics of a typical warm, partially ionized interstellar cloud (which would have low C^+ absorption). Alpha Cen is in the opposite, Center-ward direction, behind another small cloud ("G"). In fact, Linsky et al. emphasize that the interstellar medium in the vicinity of the Sun is defined by a Local Cavity of low density extending about 80 pc in all directions, in which are situated more than a dozen individual, higher density clouds. This reality counters the naive expectation expressed earlier, that the ISM column should increase systematically with distance from the Sun. Instead, the column density to any given star will depend on how many clouds are intercepted by the sightline, which might be only one or two, and thus distance is a less important determinant of ISM absorption within the EclipSS volume (which mostly is within the Local Cavity). The lack of systematics in the C II ratios of the EclipSS sample, aside from the Southern Ecliptic preference, adheres to that view.

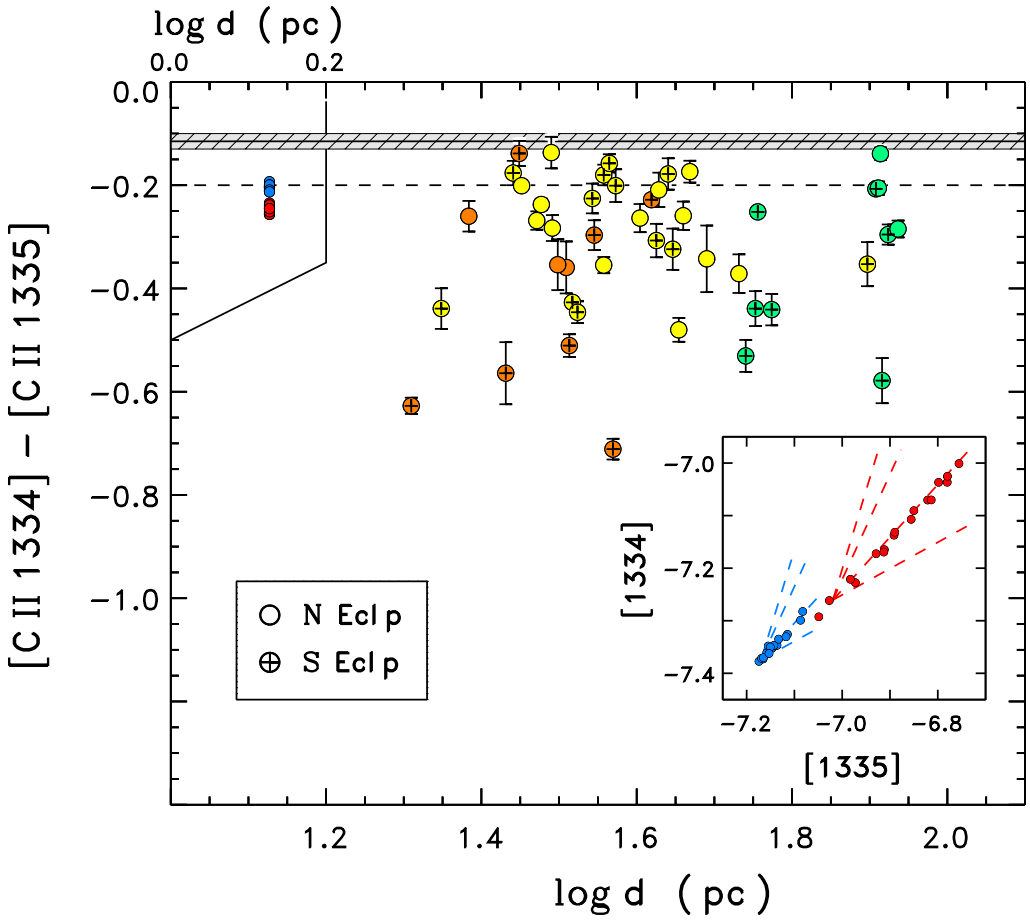
log d (pc)
0.0
0.2
0.0
−0.2
−0.4
−0.6
−0.8
−1.0
[C II 1334] − [C II 1335]
N Eclp
S Eclp
[1334]
−7.0
−7.2
−7.4
−7.2
−7.0
−6.8
[1335]
1.2
1.4
1.6
1.8
2.0
log d (pc)

Fig. 6(a).—

Fig. 6.— (a) Logarithmic ratio of the C II components as a function of the stellar distance. Alpha Cen AB ratios, over their starspot cycles, are shown in the left cutout panel as blue dots (A) and red (B), at the 1.34 pc distance of the nearby system. The α Cen C II values also are shown at lower right in an inset flux–flux diagram. The shaded horizontal band at the top of the main diagram represents the ISM-free solar 1334 Å/1335 Å ratio; the horizontal dashed line is the average for Sun-like α Cen A. The downward displacement of the A ratio is caused by interstellar absorption. The EclipSS stars are scattered in their values; no apparent trend with distance is evident. However, the smallest ratios (below -0.4 in the log) favor the S Ecliptic pole (points marked with plus signs). (Error bars here, and in subsequent figures, are $\pm 1\,\sigma$.) (b) For the N V resonance doublet, and versus the 1238 Å flux instead of distance (local ISM absorption is expected to be negligible). The Sun (open circles) also is included in the diagram because the N V components could separately be measured in the SOLSTICE scans (whereas C II was too blended). The horizontal gray dashed line represents the ratio of statistical weights of the two transitions, the flux ratio expected under optically thin conditions. (c) For the Si IV resonance doublet, and versus the 1393 Å flux instead of distance (local ISM absorption is expected to be negligible). The Sun (open circles) also is included in the diagram because the Si IV components could separately be measured by SOLSTICE. The horizontal gray dashed line represents the ratio of statistical weights of the two transitions, the flux ratio expected under optically thin conditions. (d) For the ratio of C II 1335 Å to O I 1306 Å, versus the flux of the latter. The stars were restricted to those with reported [Fe/H] values (as marked according to the legend). The α Cen stars are included, but not the Sun (both C II 1335 Å and O I 1306 Å are blended with other members of the respective multiplets in the low-resolution SOLSTICE scans).

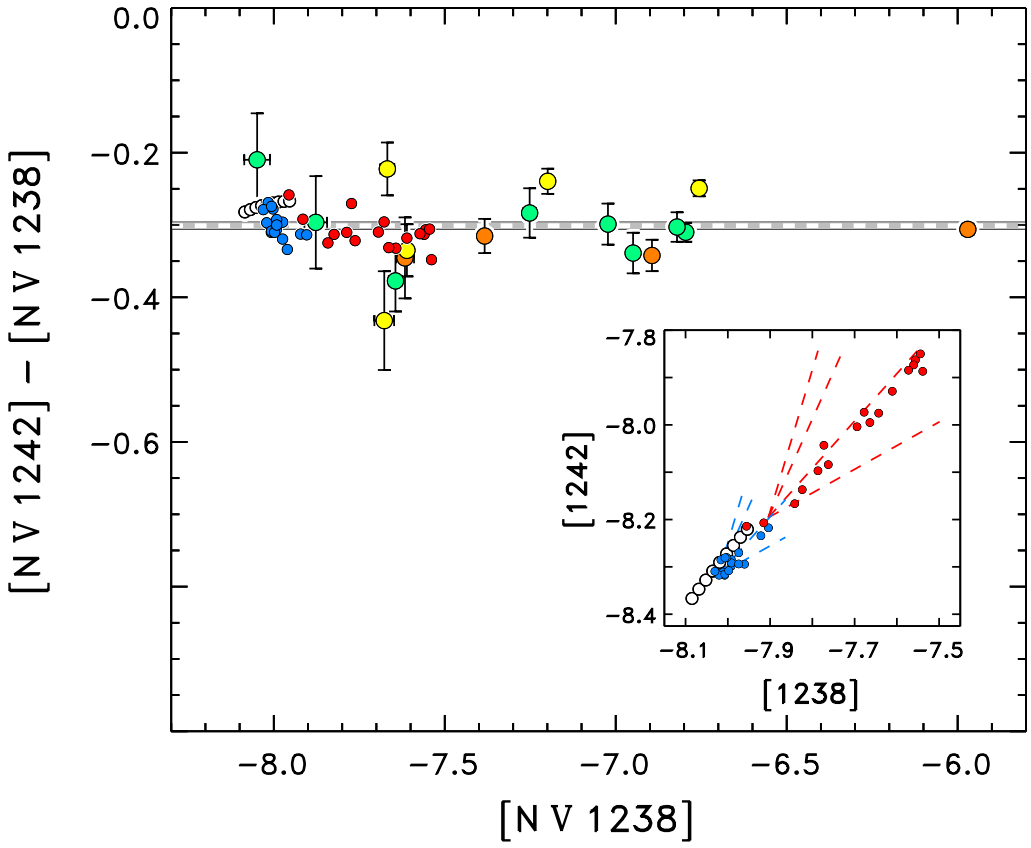

Fig. 6(b).—

3.1.2. N V 1238 Å versus 1242 Å

Figure 6(b) is similar to Fig. 6(a), but now comparing the doublet components of N V, 1238 Å and 1242 Å, and versus the 1238 Å normalized flux rather than distance (local interstellar absorption effects are expected to be negligible in this hot species). The horizontal gray dashed line represents the optically-thin ratio expected given the statistical weights of the two resonance transitions (1238 Å/1242 Å $\sim$ 2:1). Again, the α Cen cycle-resolved trends are illustrated by the blue and red points, but now also SOLSTICE measurements are included for the Sun (open circles). The α Cen (and solar values) are repeated in a 1242 Å versus 1238 Å flux–flux diagram at lower right. As before, the doublet components of all three comparison stars show 1:1 correlations over their cycle ranges, although the solar trend for 1242 Å is slightly elevated compared with near solar twin α Cen A. Possibly, this is

due to the influence of (weak) Fe XII 1241 Å on the solar N V 1242 Å line: the two features are blended at SOLSTICE resolution, but not with STIS (or COS).

In the main panel, the comparison stars and the EclipSS targets hover near the expected doublet ratio, with no indication for systematic shifts with respect to line strength. In fact, unlike optically thick chromospheric C II, the "hot" N V doublet likely is optically thin under most conceivable stellar Transition Zone (TZ: $T \sim 10^5$ K) conditions, and even if mildly optically thick, it should still show a 2:1 flux ratio because these transitions would be highly scattering ("effectively thin") owing to the low collisional quenching rates at the meager TZ densities anticipated for even the most active of the EclipSS stars. Given that the expected line ratio is empirically seen, henceforth the N V doublet will be represented by the sum of the two components (designated "N V 1240 Å").

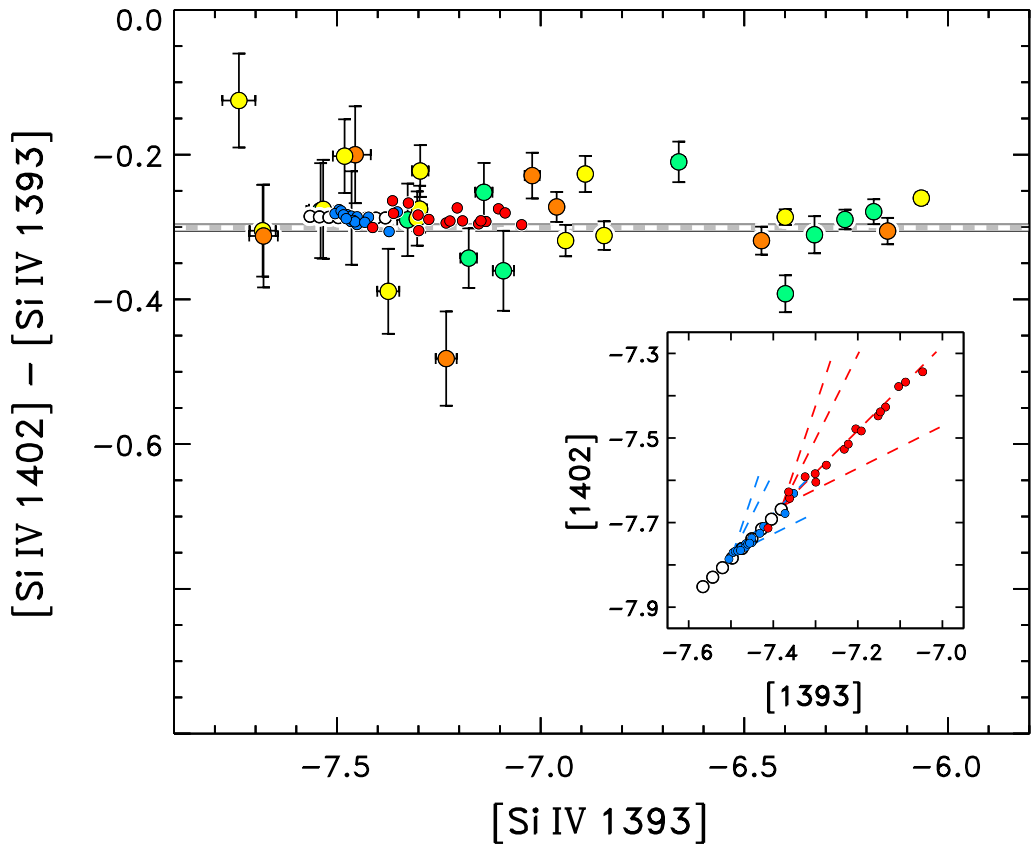

Fig. 6(c).—

3.1.3. Si IV 1393 Å versus 1402 Å

Figure 6(c) is a similar comparison for the Si IV 1393 Å + 1402 Å doublet. These features form in the stellar TZ at lower ionization temperatures than N V, and are much stronger in normal stars of all activity levels (e.g., Fig. 4). For this reason, the diagram is better populated, because more of the EclipSS fluxes satisfied the 7 σ detection threshold. The flux–flux diagram at lower right again shows the expected 1:1 correlations for all three comparison stars, which, perhaps coincidentally, are closely co-aligned. Likewise, the comparison stars show consistent ratios in the main panel, slightly elevated above the simple 2:1 statistical weight expectation. The EclipSS ratios are more scattered, but still close to the nominal value and without evidence for any systematic trends. Similar to N V, Si IV 1393 Å and

1402 Å henceforth will be presented as a combined "Si IV 1400 Å" flux.

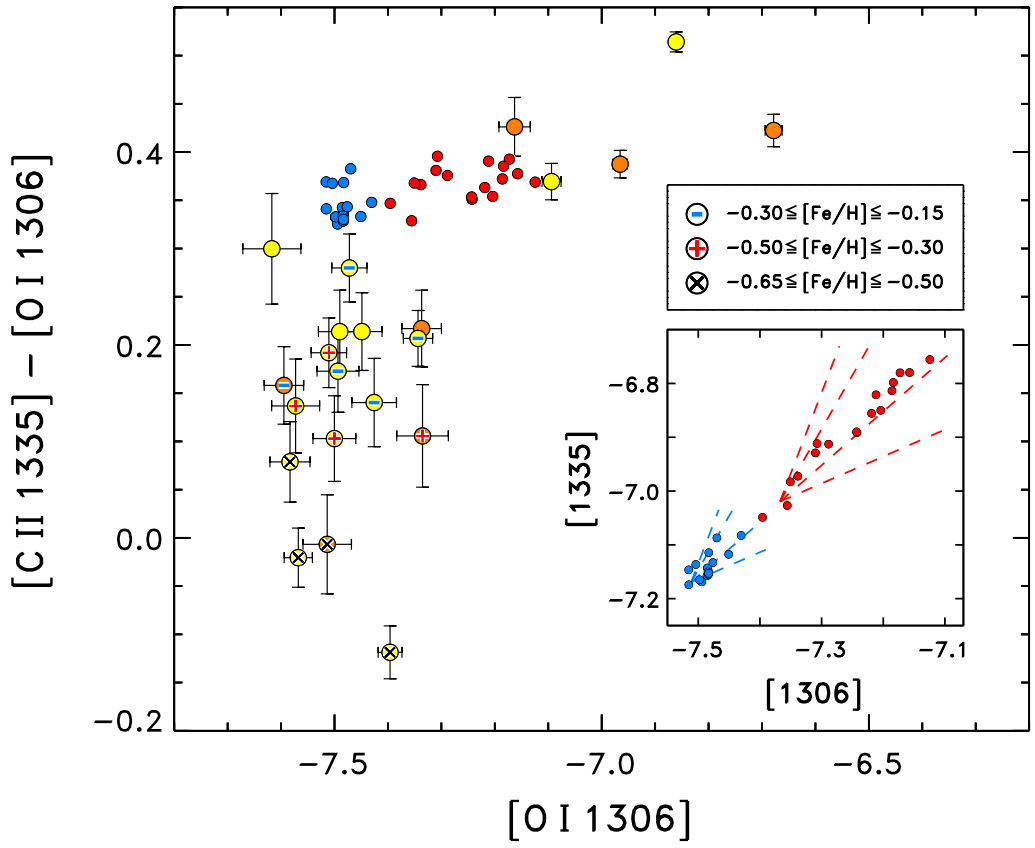

Fig. 6(d).—

3.1.4. C II 1335 Å versus O I 1306 Å

Figure 6(d) is a similar, though slightly different comparison, now for the ratio of upper chromosphere C II 1335 Å and middle chromosphere O I 1306 Å, versus the flux of the latter. The significance of the comparison will become evident later. The stars illustrated here were restricted to those that have at least one literature value of [Fe/H], and excluded the few most active EclipSS members. Alpha Cen AB are included: their metallicity ([Fe/H]$\sim$ 0.2 dex) is well-established (see Paper I). The Sun is not represented here, however, because its behavior in C II versus O I (illustrated in Figure 7(a), next) is somewhat contrary to that of α Cen AB. (The solar values in Fig. 7(a) were not directly derived from the specific C II and

O I components, but were scaled from the respective low-resolution SOLSTICE blends by activity-independent constant factors, so are not as trustworthy as the high-resolution α Cen measurements.)

The figure shows that the C II/O I ratio of the α Cen stars is relatively constant with increasing O I activity over their cycles, with only perhaps a slight increase toward higher O I flux values. The more active EclipSS stars, to the right, roughly follow that upward sloping trend. On the lower flux side, the EclipSS stars "pile up" at a minimum value of O I (x-axis direction) that is similar to the O I minimum of the α Cen A time series. However, the C II/O I ratios (y-axis direction) display a distinct downward spread below the level set by the α Cen cycles. The metallicities of the stars are marked according to the legend at the right, just above the flux–flux panel. The "slumped" C II/O I values apparently follow a trend of decreasing ratio with decreasing [Fe/H]. The implications of this behavior will be discussed at greater length later.

3.2. Flux–Flux Diagrams

The next set of figures are flux–flux diagrams pitting multiple species against a reference transition, for the EclipSS stars, α Cen AB, and the Sun (if available).

3.2.1. Reference Feature: O I 1306 Å

Figure 7(a) is for the 1306 Å component of the atomic oxygen triplet as the reference. It is an optically thick transition that arises in the middle to high chromosphere at temperatures around 6000–8000 K, and is thought to be formed, at least partially, by "Bowen fluorescence," involving a coincidence between the O I 1025 Å resonance line and bright H I Lyβ (see, e.g., Carlsson & Judge 1993). O I 1306 Å is compared to four other species that also form within, or just above, the chromosphere. In each of the panels, the flux–flux measurements of the EclipSS stars are indicated by dots, with $1\,\sigma$ error bars, color-coded by spectral type as before. Only $\geq 3\,\sigma$ values are displayed. A small $\times$ indicates low metallicity, as in Fig. 2. Also, as previously, the α Cen stars over their cycles are represented by blue dots for A and red for B, and the Sun, over its cycle, by open circles (at least for those species with SOLSTICE measurements). An inset in the lower right corner schematically illustrates a blow-up of the α Cen (and solar, if available) points by themselves. The fans of power laws in each panel are for $\alpha = 0.5$, 1, 2, and 3. The blow-up panel has a separate set of reference power laws for α Cen B (only). There, the origin of the power-law fan is well characterized.

However, in the main panel, the EclipSS origin is somewhat arbitrary, especially since the O I 1306 Å points appear to pile up at the left side of the diagram, in an apparent lower limit, just below the terminal ends of the α Cen and solar trends; and display a spread in the y-axis direction especially in the C II comparison.

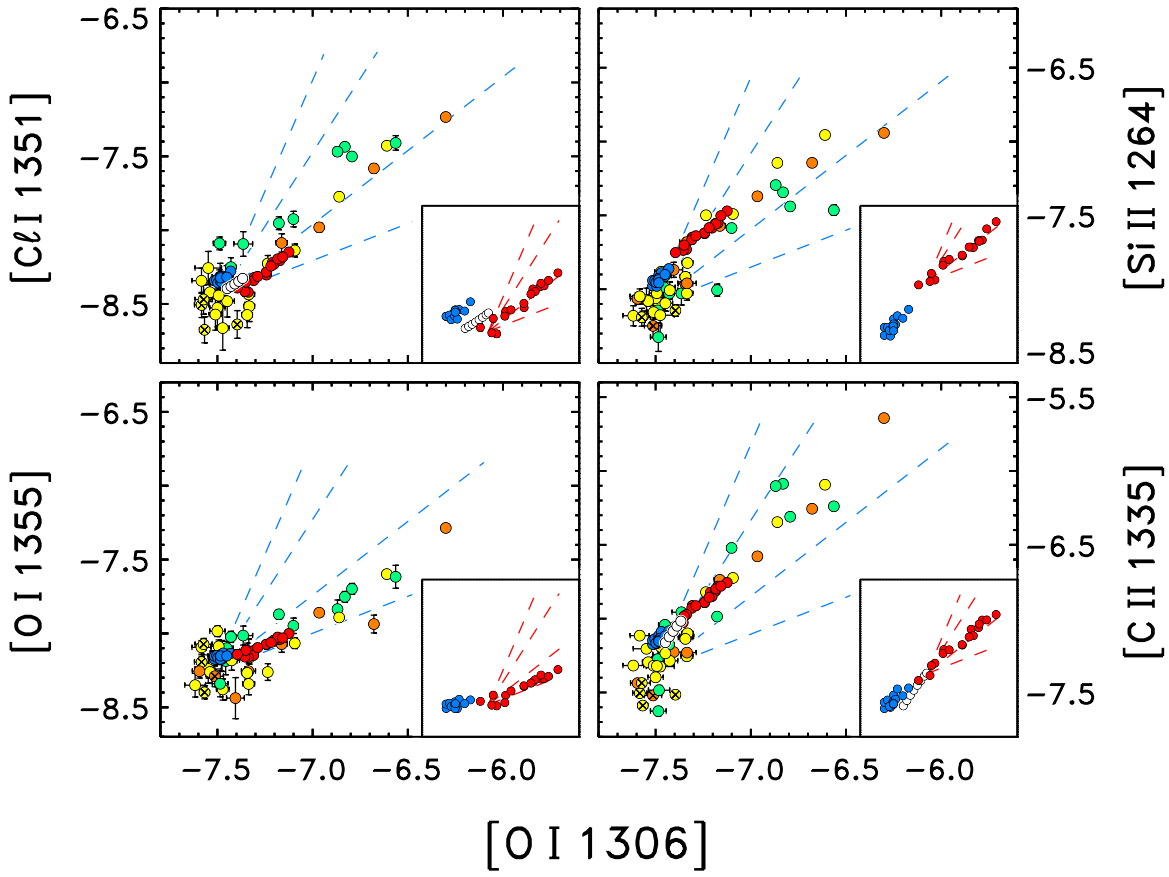

Fig. 7(a).—

Fig. 7.— (a) Flux–flux diagram for several species relative to a reference, in this case O I 1306 Å, the component of the atomic oxygen triplet least affected by geocoronal airglow and interstellar absorption. In each panel, the main part shows the correlation for the EclipSS stars, color-coded by type as in Fig. 2, and marked with × if low-metallicity. Superimposed are the cycle ranges of α Cen A (blue dots) and B (red), and the Sun, if available (open circles). The α Cen (and solar) distributions are shown separately in the lower right inset. Dashed lines indicate power laws with slopes of 0.5 (lowest), 1, 2, and 3 (highest), in the main panel and the inset (there, exclusively for α Cen B). (b) For reference species C II 1335 Å, longward component of the multiplet, and least affected by interstellar absorption. (c) For reference species Si III 1206 Å, normally brightest of the s-FUV transitions that form above the chromosphere in the low TZ.

The "pile up" (also seen in previous Fig. 6(d)) perhaps indicates a minimum chromospheric heating rate that an inactive Sun-like star achieves independently of the Dynamo-generated active regions that cause the conspicuous upward slanted trends of the α Cen and solar fluxes over their respective cycles. A similar minimalist behavior was recognized in other chromospheric diagnostics in the 1980's, during the era of the International Ultraviolet Explorer, and was called the "basal flux" (e.g., Schrijver 1987). Notice that the cluster of points near the minimum has representation from all the spectral classes, so the constant minimum value of $f_{\rm L}/f_{\rm BOL}$ suggests that the *surface flux* of O I scales as the surface bolometric flux, $\sigma\,T_{\rm eff}^4$, which also is equivalent to the energy carried by convection in the sub-surface layers. The turbulent fluid motions can release sound waves that ultimately shock in the low chromosphere (e.g., Carlsson & Stein 1992), as well as spawn small-scale magnetic fields by "local dynamo" processes (e.g., Nordlund et al. 1992), both of which are potential sources of chromospheric heating.

The lower left panel is for the O I 1355 Å intersystem line, one of the strongest of the low-excitation narrow chromospheric emissions in the s-FUV region. Lin & Carlsson (2015) concluded that the transition is optically thin, and forms mainly by recombination (in contrast to optically thick reference O I 1306 Å, which is at least partially fluoresced by collisionally excited Lyβ). According to the authors, the oxygen ionization in the chromosphere is strongly tied to that of hydrogen via charge exchange. The hydrogen ionization balance itself is complex, owing to the possibility of photoionizations out of the $n = 2$ excited level (Balmer continuum, illuminated by the photospheric radiation field), as well as non-equilibrium effects given the long collisional and recombination timescales at the low densities typical of the chromosphere, and the prevalence of transient, highly dynamic shocks (Leenaarts et al. 2007).

The O I 1355 Å versus 1306 Å diagram shows a compact cluster of points on the low-activity side, likely related to the basal heating of the chromosphere mentioned above, but then a trend of values, including especially α Cen B, slanting upward and to the right away from the terminus with a power-law slope between 0.5 and 1. All the spectral types are represented for the (few) active stars, so the $\alpha < 1$ behavior appears to be systemic, and likely conveys insight concerning the ionization properties of chromospheres as they become more intensely heated. Note on the low-activity side that the metal-poor stars display 1355 Å fluxes (y-direction) similar to those of the solar-metallicity dwarfs, and that the 1306 Å fluxes (x-direction) are only slightly lower for the metal-poor stars.

The upper left panel compares Cl I 1351 Å against the O I 1306 Å reference. Like O I 1355 Å, the chlorine line is one of the strongest of the narrow, optically thin chromospheric features of the s-FUV region, in the Sun as well as the stars. However, this line is quite

unusual, because chlorine is a rare element in the solar mixture, and there are no other strong Cl I transitions from the same multiplet, or any other multiplet for that matter, in the FUV spectrum. Shine (1983) resolved the conundrum, which had been recognized in early solar rocket and satellite spectra, by showing that a ground-state Cl I transition at 1335 Å was coincident with the strong 1335 Å component of upper chromosphere C II, and connects to the upper level of Cl I 1351 Å. Thus the anomalous strength of 1351 Å must be caused by UV pumping. One curiosity of this explanation is that the abundance of atomic chlorine likely peaks in the low and middle chromosphere, where densities are high, while in a normal stratified chromosphere, the C II emission would arise much higher, where the temperatures are between 1–2×10^4 K (Rathore & Carlsson 2015). To be sure, C II 1335 Å would be strongly scattering in the chromosphere, so a diffuse downward directed 1335 Å radiation field certainly could be present in the lower lying chlorine layers. More realistically, though, the chromosphere is a highly dynamic and inhomogeneous place, so there likely are situations where hot shocks, or local magnetic reconnection events, spiking to C II temperatures are in closer proximity to cool plasma, thereby enhancing the radiative pumping of fluorescent transitions like Cl I 1351 Å.

In the Sun and the α Cen stars (see inset at right side of main panel), Cl I displays a roughly 1:1 correlation with the O I reference, but, as shown shortly, C II 1335 Å has a steeper than $\alpha = 1$ power law against the oxygen emission in the Sun and α Cen A (the C II–O I power law, however, flattens to 1:1 for more active α Cen B). Thus, the chlorine emission, at least in the two solar-like comparison stars, shows a shallower than 1:1 dependence on the radiative pumping transition C II, possibly reflecting the inefficiency of the photon diffusion process. In fact, the 1:1 correlation between Cl I 1351 Å and O I 1306 Å perhaps is instructive, because the oxygen triplet also is fluoresced by an upper chromosphere transition (Lyβ) with the same difficulty of photon penetration from source region to pumping layers.

Even more curious, there appears to be a significant separation of the Cl I–O I power laws between α Cen A, the Sun, and α Cen B (see inset), and a further displacement of most of the F types relative to the cooler EclipSS dwarfs. The major physical difference between the F dwarfs and the others is that the warmer stars likely have thinner chromospheres (in hydrogen column density: see discussion by Ayres 2015), which, in principle, would favor photon diffusion and fluorescence processes.

The upper right panel compares the Si II 1264 Å blend, which forms in the middle chromosphere much like the Mg II 2800 Å h & k lines, and similarly is from a low-FIP species (low-FIP elements can display enhanced coronal abundances in the Sun owing to a controversial fractionation process that likely has its roots in the chromosphere (see, e.g.,

Laming et al. 1995)). In the α Cen inset panel, the A correlation is at lower flux levels than B, but is steeper. Further, the B relation steps up significantly compared with A, but anchors the general trend displayed by the more active of the EclipSS FGK dwarfs. The step-up indicates that at a given chromospheric Si II flux, the O I emission is less than expected for the active stars. These objects tend to have thicker chromospheres (see, e.g., Ayres 1979), which might act to partially suppress the Lyβ diffusion and consequent fluorescence of the oxygen triplet. At the same time, the cluster of Si II–O I points on the low-activity side is relatively compact, as seen earlier for O I 1355 Å and Cl I 1351 Å, showing that all these features have well-defined basal minima, close to the Sun/α Cen A values, for this minimally-biased sample of mostly inactive stars.

In contrast, the lower right panel illustrates upper chromosphere C II, which displays a larger spread (y-direction) in values at the O I 1306 Å minimum (as previously seen in Fig. 6(d)) than the other, albeit pure-chromosphere, tracers. Like Si II, however, C II has a similar step-up: steep power law for the Sun, which then flattens at a higher level into a roughly 1:1 correlation for the α Cen B cycle series, and beyond into the higher activity EclipSS stars. The C II–O I relation is well mixed in terms of the EclipSS spectral types, showing that the surface temperature dispersion in the Cl I panel is related to something other than the simple flux of the pumping line C II 1335 Å.

3.2.2. Reference Feature: C II 1335 Å

Figure 7(b) is for C II 1335 Å as the reference. C II is an important solar plasma diagnostic for the Interface Region Imaging Spectrograph (IRIS: De Pontieu et al. 2014). IRIS carries out long-slit stigmatic spectral imaging of the Sun's atmosphere at moderate spectral resolution ($\lambda/\Delta\lambda \sim 35{,}000$, similar to the STIS FUV medium echelle, and about twice that of COS G130M); high spatial resolution (down to $0.33''$); and high temporal cadence as well. IRIS has three spectral channels: one NUV (2785–2835 Å—Mg II 2800 Å) and two FUV (1332–1358 Å—C II 1334 Å + 1335 Å, Fe XII 1349 Å, Cl I 1351 Å, O I 1355 Å; and 1390–1406 Å—Si IV 1393 Å + 1402 Å, O IV 1401 Å). Both the IRIS FUV channels are covered by the COS G130M settings here.

The C II multiplet is the brightest feature captured by IRIS, which, however, is only part of its significance. Rathore & Carlsson (2015) determined that the C II emissions can form throughout the chromosphere, where at low temperatures (5000–7000 K) a high fractional ionization of atomic carbon is maintained by photoionization (driven mainly by Lyα). The collisionally excited C II lines are optically thick (although, importantly, effectively thin: Judge et al. 2003), and the cores arise in the crucial upper boundary at the top of the

classical chromosphere, segueing into the overlying low-TZ (the latter represented here by C III 1175 Å and Si III 1206 Å). Rathore et al. (2015) showed that while C II forms just above the layers in which the strong NUV Mg II lines become thick, the C II cores are much less influenced by the dynamical signatures seen pervasively in the h & k lines, and attributed to acoustic shocks in the low chromosphere (like the analogous violet Ca II H & K lines near 3950 Å, in the pioneering radiation-hydrodynamic modeling by Carlsson & Stein (1992) mentioned earlier).

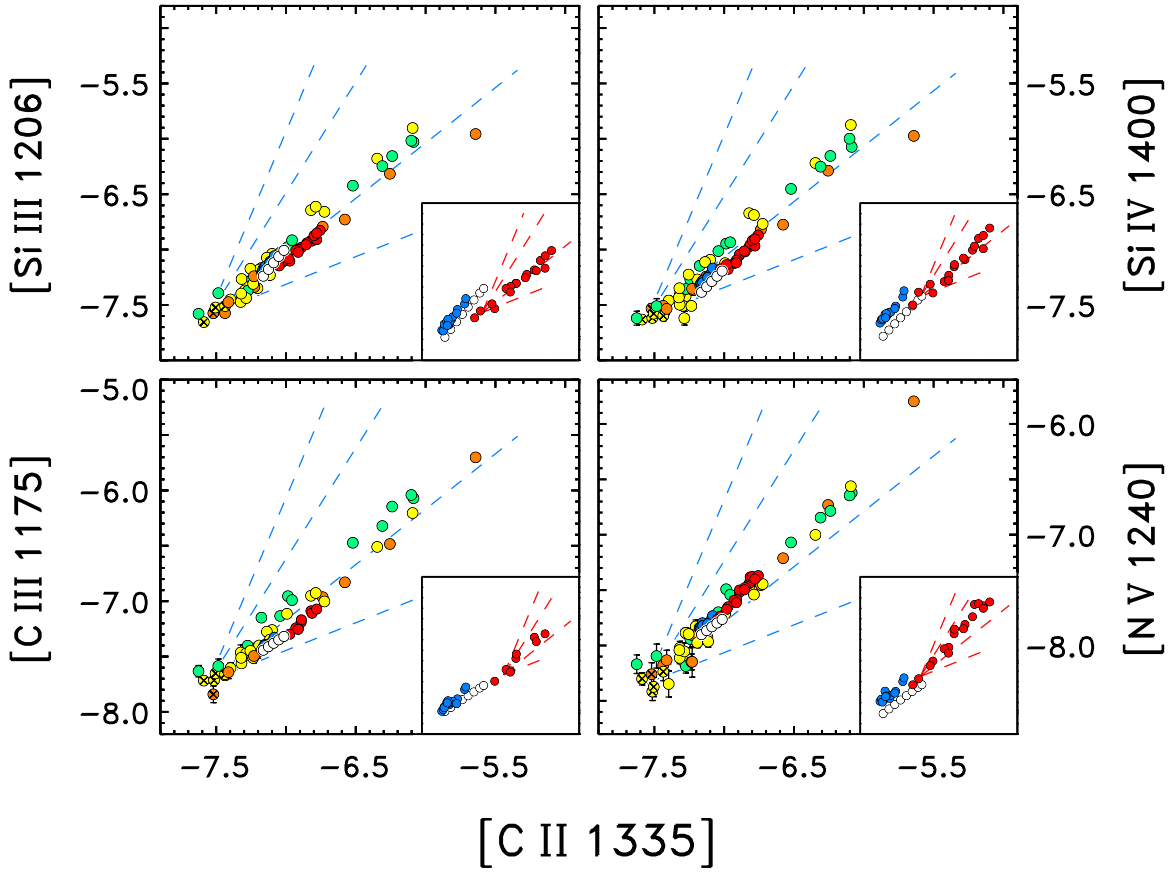

Fig. 7(b).—

In Fig. 7(a) (and earlier in Fig. 6(d)) there was a prominent downward slump of C II intensities, below the terminus of the solar cycle trend, at the basal boundary marked by the minimum O I 1306 Å normalized flux. Apparently, there are Sun-like stars in the minimally biased EclipSS sample that have significantly less C II emission than the Sun itself, or solar twin α Cen A. However, the downward slump of C II intensities in Fig. 7(a) versus O I, is replaced in Fig. 7(b) by sharply pointed flux–flux correlations against the higher ionization temperature, low-TZ emissions C III and Si III (3–5$\times10^4$ K), and middle-TZ Si IV and N V (0.8–2$\times10^5$ K). There is no obvious basal pile-up in any of these features, in line with the notion that the higher temperature emissions are exclusively connected with magnetic processes that seem to avoid the conspicuous minimum fluxes seen in chromospheric O I here (and Mg II in previous studies). Superficially, all the TZ indicators display similar power-law correlations versus C II, with slopes near $\alpha = 1$.

Nevertheless, examining the EclipSS behaviors more closely, especially the comparison stars α Cen and the Sun, reveals subtle distinctions. C III 1175 Å, at lower left, shows a somewhat flatter relation for the two G-type comparison stars, which steepens for α Cen B's cycle. The low-activity EclipSS G and K trend seems to initially follow the shallower solar distribution but then steepens at fluxes similar and above α Cen B into the active G and K dwarf regime. The F stars appear to show a more consistent slope throughout the activity range, slightly displaced above the main trend defined by the cooler dwarfs.

Si III 1206 Å, at upper left, at first glance appears to nearly be identical to C III, displaying a roughly 1:1 correlation with C II 1335 Å. However, now the Sun and α Cen A show steeper cycle tracks than α Cen B, while, curiously, the flatter B relation originates somewhat below those of the Sun and A. The more active dwarfs seem to favor the α Cen B slope, with the G dwarfs somewhat above the K dwarfs, and the F stars in the middle.

Si IV 1400 Å, at upper right, has a similar look to the previous panel for Si III, although the fine details, especially the solar behavior versus α Cen B, are different. Now, the B trend is steeper, and the solar relation flows seamlessly into it. Meanwhile, α Cen A is parallel, displaced upward. Some of the deviations can be ascribed to small abundance differences between α Cen and the Sun (see Paper I), but the differential behavior between the A Si III and Si IV relative to the solar trend probably is an excitation effect. The EclipSS stars, taken altogether, trace out a correlation that is steeper than 1:1, but shallower than that of α Cen B over its cycle. Again, there is a slight apparent separation among the more active stars with respect to type, although possibly coincidental given the small numbers.

The lower right panel presents the correlation relative to N V 1240 Å, hottest of the TZ lines in the s-FUV band. The cycle trend for the Sun is flatter than that of α Cen B, while the more active of the EclipSS stars seem to favor B's $\alpha > 1$ relation. The active dwarfs

are more tightly arrayed with respect to type in this comparison, and the most active of the EclipSS sample—K dwarf HD 41004—is conspicuously elevated.

Finally, the minimum values of f_L/f_{BOL} for the EclipSS hot lines in all four comparisons consistently are lower than those of solar MIN, by factors of 2–4.

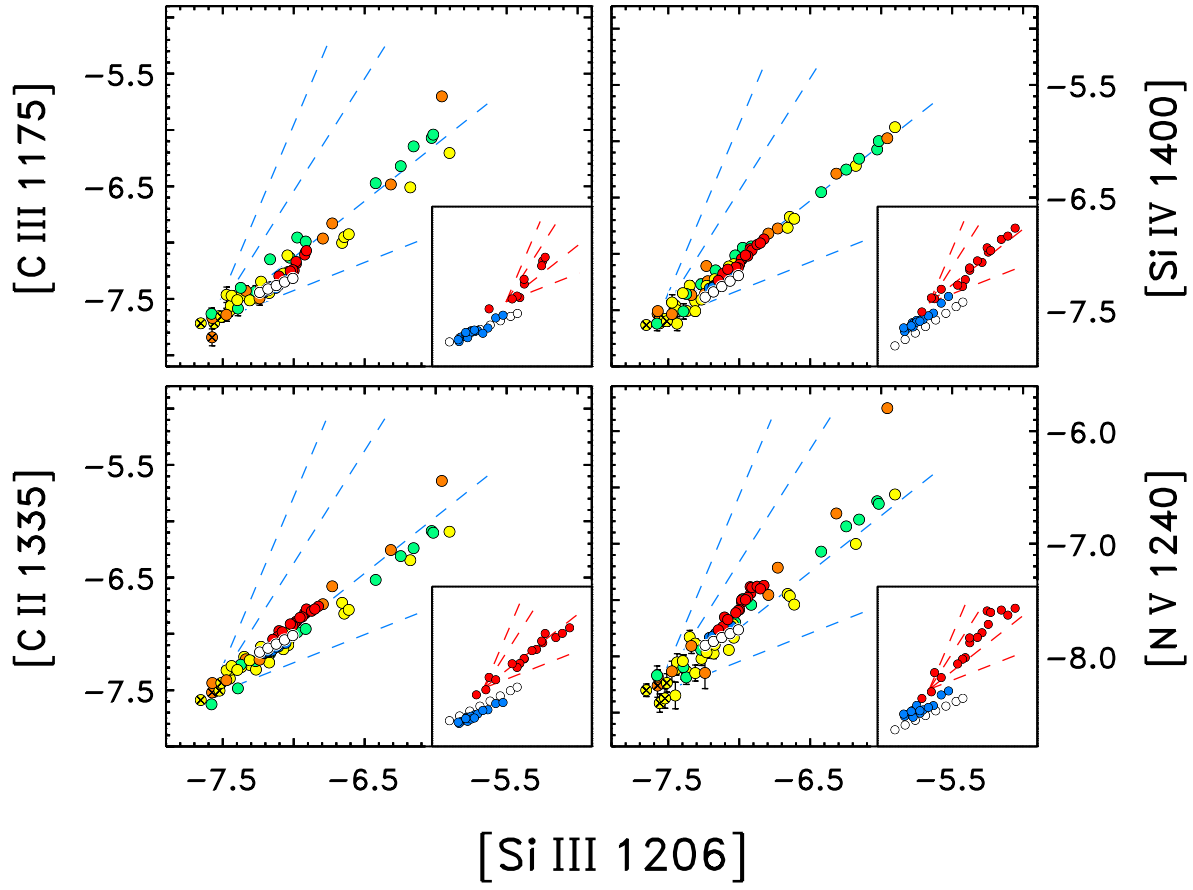

Fig. 7(c).—

3.2.3. Reference Feature: Si III 1206 Å

The final quartet of comparisons, in Figure 7(c), is with Si III 1206 Å as the reference. The Si^{++} resonance line is comparable in brightness to the 1335 Å component of C II, but forms at a higher ionization temperature, about 5×10^4 K. In Paper I, Si III was accorded special status, because over the solar cycle variation (and that of α Cen A), it exhibited

the steepest power laws with respect to chromospheric Mg II, whereas previous stellar experience dictated that the correlations should rise systematically with increasing ionization temperature, normally favoring N V for the most extreme slope in the FUV (see discussion in Paper I). Even so, the inverted temperature behavior did not extend to more active α Cen B. Here, in Fig. 7(c), a similar trend is seen. The Sun and α Cen A have shallow power-law slopes for all the species, largely paralleling the low-activity EclipSS dwarfs, but α Cen B and the more active EclipSS stars display steeper correlations (note, especially, the K dwarfs in the N V panel), more in line with the previous stellar expectation. Even so, the Si IV–Si III correlation is very close to 1:1 despite the 30,000 K difference in formation temperature of the two ions.

4. DISCUSSION

All the flux–flux behaviors presented here undoubtedly hold clues, in some cases nuanced, to the expression of chromospheric and sub-coronal heating in the disparate objects of the EclipSS sample, as well as the two Sun-like comparison stars, and the Sun itself.

The EclipSS-reinforced historical finding that Sun-like dwarfs can have significantly lower C II surface fluxes than the Sun at its cycle minimum is provocative. (In Schrijver's (1987) original study of C II basal fluxes, many of the survey stars were subgiants, giants and supergiants, in addition to dwarfs, whereas the stars of the EclipSS sample exclusively are dwarfs, or in a few cases pre-subgiants. Thus, the depressed basal limits seen here are not biased by radically different surface gravities.) The existence of sub-solar basal fluxes is surprising, if one imagines that at solar cycle minimum, when the disk is free of active regions, the global C II emission is dominated by the supergranulation network. That minimum should be more-or-less universal among Sun-like stars, if the network fields mainly are produced by surface effects, related more to local convection (e.g., $T_{\rm eff}^4$) than external Dynamo properties like rotation (which can vary significantly from object to object). Note that α Cen A has a similar C II minimum as the Sun, despite the Sun's larger cycle range: α Cen A and the Sun are similar in temperature, gravity, and rotation period, although A is slightly more evolved and slightly metal-rich (see Paper I).

A similar conclusion was reached by Judge et al. (2003), who examined spatially resolved solar FUV spectra of C II 1335 Å (from SoHO/SUMER) in the broader context of stellar basal limits on C II, such as proposed by Schrijver (1987). Judge et al. determined that the solar C II emission is concentrated in the magnetic supergranulation network, rather than powered by acoustic shocks in the internetwork cells like some fraction of the Mg II and Ca II emission. In fact, it often was argued that the basal fluxes dominantly are "acoustic," because

the empirical minimum fluxes are large for the low-FIP ions Mg^+ and Ca^+, and the dynamical impacts are clearly imprinted on the line profiles; whereas the empirical minimum fluxes are small—in fact challenging to quantify—for higher ionization temperature C II and C IV (e.g., Schrijver 1987), and the low chromosphere dynamical influences are more difficult to see (e.g., Martínez-Sykora et al. 2015). Nevertheless, some fraction of the basal fluxes, including Mg II and Ca II, must be "magnetic," thanks to the influence of the ubiquitous supergranulation network, which supports emissions from both chromospheric and TZ species, albeit at much lower levels than in active regions.

In any event, there were some disagreements between the Judge study and that of Schrijver concerning where the Sun, as a star, fell in the stellar C II context, and the appropriate value of the basal flux. The solar C II 1335 Å flux, taken at the Cycle 23/24 minimum (Table 4), converted back to the full multiplet, and further expressed in surface flux units (compatible with the Judge et al. study) is $F_{\rm C\,II} \sim 7.0{\times}10^3$ erg cm^{-2} s^{-1}. The minimum $F_{\rm C\,II}$ for the "slumped" stars in Fig. 7(a), using the solar bolometric surface flux, $F_{\rm BOL} \sim 6.29{\times}10^{10}$ to scale $f_{\rm C\,II}/f_{\rm BOL}$, is about $2.8{\times}10^3$ erg cm^{-2} s^{-1}, significantly below the solar MIN level. Schrijver had proposed $F_{\rm C\,II} \sim 3.4{\times}10^3$ for the minimum Sun (as reported by Judge et al., and including an upward correction applied by those authors), which is a factor of 2 smaller than the solar MIN value obtained here (the latter is compatible with the Judge et al. $\bar{I}$ values (their Table 2) for solar MIN from "SOLSTICE-I" (a precursor, lower resolution version of the SORCE/SOLSTICE spectrometer utilized in Papers I and II)). A factor of two difference between the old and new solar MIN values is perhaps not concerning given the more primitive nature of the solar measurements Schrijver had available at the time, compared with state-of-the-art SORCE/SOLSTICE now. In fact, the stellar basal surface fluxes for C II proposed by Schrijver (as quoted in the Judge Table 2), based on low resolution ($\lambda/\Delta\lambda \sim 200$) measurements by IUE and not corrected for ISM absorption, are only slightly lower than the EclipSS minimum $F_{\rm C\,II}$ seen here. Significantly, the EclipSS minimum is similar to the solar internetwork ("cell center") C II surface fluxes cited by Judge et al., as well as to a few scattered measurements (HST+IUE) of low-activity G dwarfs in the authors' Table 2.

There is, however, a basal flux gorilla in the room, so to speak, namely the fact that most of the depressed C II points (Figs. 6(d), 7(a), and 7(b)) represent low-metallicity G and K stars. Further, the two low C II F stars (of unknown metallicity) are pre-subgiants (with reduced surface gravities).

The bright chromospheric emissions of a star, say Mg II or Ca II, normally do not depend strongly on metallicity. This is because these species are the dominant radiative coolants of the chromosphere, through electron collisional excitation of effectively thin resonance

transitions. If the heating of the chromosphere is a weak function of metallicity, as expected for acoustic shocks or magnetic reconnection, then the integrated emission of a cooling species such as Mg II will closely follow the heating input (because cooling must balance heating), nearly independently of the chemical composition. In other words, a chromosphere on a low-metallicity star must adjust its structure (mainly by thickening in column density) to accommodate reduced metal-contributed collisional electrons and lower abundances of the cooling lines, in order to provide the same total cooling. (This is the essence of arguments advanced by Ayres (1979) to explain puzzling aspects of the Wilson-Bappu Effect, alluded to earlier.) Any subsidiary species that, like Mg^+, is the dominant ionization stage in the chromosphere, such as atomic oxygen, will have resonance-line fluxes, e.g., of O I 1306 Å, closely paralleling the Mg II emission, thanks to the systematically altered chromospheric structure.

In the upper chromosphere, where C II forms, the situation is analogous, but different. There, the local cooling is almost exclusively controlled by H I Lyα, and hydrogen ionization is the main source of collisional electrons. Accordingly, the thermal structure, specifically the hydrogen column density, will be dictated by Lyα, again independently of metallicity (but more trivially than for the main chromosphere). If the heating at upper chromosphere altitudes is independent of metallicity, the hydrogen columns will be similar for normal and metal-poor stars. In that situation, the emission strengths of ancillary metal lines will be responsive to composition, C II in the case at hand, but also species like Si III and C III. This is because the C II column density will be proportional to the (fixed) hydrogen column times the composition-dependent carbon abundance. Paradoxically, then, the C II intensity can be affected by metallicity even when the upper chromosphere heating is not. This is what is seen in the right hand panels of Fig. 7(a). The Si II–O I comparison shows a more compact mixed-metallicity basal regime, suggesting that both chromospheric emissions are less sensitive to composition. On the other hand, the C II–O I comparison displays a stronger downward trend on the C II side, dominated in the lowest part by the metal-deficient dwarfs (and the two lower gravity F stars).

However, it is possible that the high-altitude heating, which must mainly be magnetic, also depends on metallicity, at least in the secondary sense that metal-poor stars tend to represent older stellar populations, and such objects often are less active in the higher-temperature indicators, such as C IV or coronal X-rays (but not so different in chromospheric emissions, as seen in Fig. 7(a)). If the high-altitude heating also is reduced in the metal-poor stars, the C II flux will be doubly affected, both by a reduced hydrogen column in the upper chromosphere and the lower carbon abundance. Thus, C II appears to be an especially sensitive tracer of metallicity effects.

The idea that the upper chromosphere heating at C II temperatures might be lower in metal-poor stars is countered to some extent by Fig. 6(d), where the depressed C II fluxes relative to O I are nearly proportional to the abundance depletions, rather than even more suppressed as in the situation where the heating itself was reduced.

The possibility that the C II minimum fluxes are responding to metallicity effects alters how one views the "basal" fluxes for C II, and indeed all the hotter species. If one disregards the C II low points (in Figs. 6(d), 7(a), and 7(b)) connected with the low-metallicity stars, one is left with a new "solar-metallicity" basal limit that is much closer to the solar MIN value (dominated by the supergranulation network for C II), rather than down at levels several times lower, close to the magnetically weak internetwork floor in the Sun.

It is an intriguing possibility that solar cycle minimum, despite the complete absence of active regions, still represents a magnetically active state powered by the local dynamo and shaped by the supergranular flows. This bears on the question of what the solar high-energy spectrum might have been like during the 17th Century Maunder Minimum (Eddy 1976), an extended period (of many decades) when the Sun was relatively spot-free. If the Dynamo simply was in a holding pattern at the normal cycle minimum state, then the solar UV would have been no different than a contemporary solar MIN (a view advocated by Judge & Saar 2007). Even if the Dynamo had temporarily slipped into a hypothetical even lower state, the local dynamo would not care, and still continue to relentlessly replenish the supergranulation network with magnetic flux. The outcome would be the same as for a normal solar MIN. (Thus, one need not be apprehensive concerning potential consequences of a future "Eddy Minimum," because the solar conditions should be no different than, say, in early-2020 during the interregnum between Cycles 24 and 25.)

5. CONCLUSIONS

The new EclipSS study of Sun-like dwarf stars is unique compared with historical efforts such as the ROSAT-IUE All-Sky Survey (RIASS: Ayres et al. 1995), which attempted to broadly sample all the FGK luminosity classes; and more recent exoplanet-oriented programs such as MUSCLES (France et al. 2016), which have focused on the later-type K and M dwarfs. The latter are better targets for exoplanet detection by transit photometry, or the radial velocity method, owing to the associated observational biases. There is an additional potential advantage (for the development of life) of the long MS lifetimes of the low-mass dwarfs; but with the downsides of multi-Gyr high-activity phases and frequent flaring. The more luminous Sun-like early-F to early-K stars, on the other hand, have more voluminous habitable zones, to maximize the chances of actually enclosing a planet; and shorter-lived

high-activity phases, to minimize atmospheric erosion and thereby preserve a potentially habitable ecosphere. The EclipSS program also is unique in the number of objects, nearly 50, observed in a narrow range of spectral classes, and in terms of the minimally biased sample selection. The latter was done mainly by location, near the N or S Ecliptic poles (for ancillary observational reasons described earlier); and visual magnitudes in a narrow range; with a secondary criterion of a clean surrounding star field; but no pre-selection on FUV emission-line brightness (unknown for these faint, otherwise anonymous cool stars).

The minimally biased EclipSS sample has opened a new window on stellar chromospheric and sub-coronal behavior that has clarified a number of previous open questions.

First, many of the EclipSS Sun-like stars are in fact rather Sun-like in their activity levels, across all the important spectral diagnostics from chromospheric O I to middle-TZ N V. The study benefitted in this regard from the SORCE/SOLSTICE measurements of key solar FUV tracers over the post-maximum decline of solar Cycle 23, in 2003, all the way to the end of Cycle 24, 17 years later. Equally informative, from a contextual point of view, were similar cycle-spanning histories of FUV fluxes from long-term HST/STIS monitoring of the Sun-like stars of the central AB binary of the nearby α Cen triple system. These comparisons demonstrate that the Sun occupies a perfectly normal position on the low-activity side of the EclipSS distribution, with no notable deviations from the norm in any of the spectral tracers examined. This would not be welcome news for the advocates of "solar exceptionalism," but it is the observational reality.

Second, there are potentially informative differences in flux–flux behavior going from the low-activity cool stars of the EclipSS sample, including the Sun and its near-twin α Cen A, to the (albeit few) more active sample members, with the cycle-spanning fluxes of moderately active K-star α Cen B guiding the way. It is remarkable that the flux–flux correlations are so systematic in their trends, often shunting from one power law at lower activity to a different slope at higher activity, and occasionally with curious differential displacements for the different spectral types. The systematic nature of the shifting power laws offers some hope that they can be modeled in a way that would illuminate the underlying heating and cooling mechanisms, so that predictive prescriptions can be developed (to help understand, for example, the time history of radiative impacts on the atmosphere of an exoplanet orbiting a Sun-like star, perhaps an Earth 2.0).

Finally, the significant EclipSS sample size, containing by chance a number of mildly metal-poor dwarfs, has unveiled a new view of the so-called "basal" minimum fluxes of low-activity stars in the hotter lines like C II. Previous stellar surveys suggested that the stellar basal limit in key C II might be well below solar MIN fluxes, which are controlled by the supergranulation network, perhaps as low as the more magnetically-free internetwork regions.

EclipSS has shown, however, that most, if not all, of the C II-deficient stars are metal-poor (or low gravity pre-subgiants in two cases), for which the C II flux can be reduced even if the upper chromospheric heating is the same as at solar metallicity. Ignoring these outliers, the revised basal limit of C II is close to that of solar MIN, so it is not necessary to invoke extraordinary scenarios to explain how a Sun-like star might fall well below what probably is a more-or-less universal supergranulation/local-dynamo baseline at a given stellar type.

For the future, the TESS optical light curves of the EclipSS sample—targets intentionally selected to benefit from several or more sectors of near-continuous photometric coverage—can be analyzed to estimate rotation periods of the members, the crucial ingredient for at least the cycling Dynamo part of the activity picture (but perhaps also for the local dynamo if there is any subtle influence of large-scale rotation, or differential rotation, on the small-scale magnetic production process). The X-ray properties of the sample also will become clearer through additional eROSITA sky surveys beyond the two currently in hand. One-off, but deeper, X-ray exposures by the Chandra Observatory could provide baseline measurements to complement the long-term eROSITA series, and new HST/COS pointings could capture the long-FUV region, reluctantly forsaken in the initial survey (especially C IV 1548 Å + 1551 Å, a crucial radiative coolant and plasma diagnostic), particularly for the ten, or so, most extreme objects of the EclipSS sample. As of this writing, HST and Chandra programs with these aims are underway, and early observations have already been obtained.

Beyond the purely observational efforts, it would be instructive for solar radiation-hydro-MHD modelers to undertake chromospheric simulations with reduced metal abundances to test whether the different cooling regimes—metal lines and metal ionization in the lower chromosphere, Lyα and hydrogen ionization in the upper layers—truly do impose the systematic structural changes alluded to earlier in the discussion of basal fluxes. Greater generality and diversity in such outer atmospheric simulations, analogous to that done with grids of photospheric hydrodynamic convection models (Ludwig et al. 2009), ultimately should allow us to more clearly understand how these peculiar layers on the outsides of stars operate, as well as to better evaluate the harsh radiation fields produced under the rather extreme conditions of high temperatures and low densities, and the impacts on their surroundings, especially planetary systems, including our own. EclipSS, rather than darkening this landscape, has perhaps brightened it.

This work was supported by grants from the Space Telescope Science Institute, operated by the Associated Universities for Research in Astronomy, under contract NAS5-26555 to NASA. This research also has made use of the SIMBAD database, operated at CDS, Strasbourg, France; and the VizieR catalogue access tool, CDS, Strasbourg, France (DOI: 10.26093/cds/vizier; the original description of the VizieR service was published in 2000,

A&AS 143, 23). The VizieR interface provided entry into Gaia Data Release 2, the earlier Hipparcos catalog, and PASTEL. This research benefited from access to the NASA/IPAC Infrared Science Archive, which is funded by NASA and operated by the California Institute of Technology. This work has made use of data from the European Space Agency (ESA) mission Gaia (https://www.cosmos.esa.int/gaia), processed by the Gaia Data Processing and Analysis Consortium (DPAC, https://www.cosmos.esa.int/web/gaia/dpac/consortium). Funding for the DPAC has been provided by national institutions, in particular the institutions participating in the Gaia Multilateral Agreement.

A. Stellar Fundamental Parameters

There are several stellar parameters that play central roles in the EclipSS analysis. The primary ones are spectral type and bolometric flux ($f_{\rm BOL}$ in erg cm^{-2} s^{-1} at Earth). Spectral type is used here to roughly discriminate between stars having deep convective envelopes (mid/late-G to K) and those with shallower convective layers (F to early-G). Convection zone depth is thought to play a crucial role in the Dynamo, often expressed in terms of the Rossby number, a ratio of rotational and convective timescales (Noyes et al. 1984). The bolometric flux is important as a normalization factor for the observed COS s-FUV fluxes, to help de-bias against different stellar sizes and distances. An important part of the bolometric flux calculation is the bolometric correction (BC), which depends on the shape of the stellar spectral energy distribution (SED). Other important, but more ancillary, stellar parameters are luminosity and radius (normally expressed in solar units: $L_\star/L_\odot$ and $R_\star/R_\odot$); the effective temperature, $T_{\rm eff}$ (K); surface gravity, $\log g$ (cm s^{-2}); and metallicity, [Fe/H] (logarithmic ratio with respect to solar abundances).

The bolometric flux can be calculated from an observed stellar magnitude, say Gaia G, with a (usually $T_{\rm eff}$-dependent) BC specific to the particular filter system, and a flux conversion factor, calibrated against solar quantities, i.e., the absolute magnitude of the Sun in that system:

$$f_{\rm BOL} \sim 2.55{\times}10^{-5}\ 10^{-(G+{\rm BC})/2.5}\ \ {\rm erg\ cm^{-2}\ s^{-1}}\ . \tag{A1}$$

Here, the leading (calibration) constant (see Ayres 2018) was based on Casagrande & VandenBerg (2018)—$G_\odot = -26.90$ mag and ${\rm BC}_\odot \sim 0.08$ mag—together with the solar irradiance, $1.361{\times}10^6$ erg cm^{-2} s^{-1} at 1 au. Following Casagrande & VandenBerg (2018), a correction was applied to the DR2 tabulated G magnitudes (to account for a small systematic error in the photometric scale of unknown origin),

$$G_{\rm corr} = 0.0505 + 0.9966\, G\ . \tag{A2}$$

The corrected G was used in the previous relation for $f_{\rm BOL}$. At the typical $G \sim 7.5$ mag of the EclipSS targets, $G_{\rm corr}$ is 0.025 mag fainter, thus the corresponding $f_{\rm BOL}$ would decrease by about 2 %.

The (bolometric) luminosity follows from the distance:

$$L_\star/L_\odot \sim 3.118{\times}10^4\ f_{\rm BOL}\ d_{\rm pc}^2\ , \tag{A3}$$

where d is the distance in parsecs ($d = 10^3/\varpi$ pc, with the parallax ϖ in marcs). The radius follows from the luminosity and effective temperature according to the Stefan-Boltzmann law:

$$R_\star/R_\odot = \sqrt{L_\star/L_\odot}\ /\ (T_{\rm eff}/5772)^2\ . \tag{A4}$$

The numerical value is the solar $T_{\rm eff}$ (K). The stellar effective temperature can be derived by inverting the above relation if R is known independently (for example, the radius might directly be measurable in favorable cases by interferometry). More typically, the effective temperature is obtained from model fits to an SED, or as a necessary byproduct of atmospheric simulations (say to achieve a balance between temperature-sensitive line ratios).

The surface gravity—$g \sim M_\star/R_\star^2$—requires additional knowledge of the stellar mass, either through evolutionary tracks or binary-star orbits; but in practice often is quoted in stellar catalogs as derived from analyses of atmospheric ionization ratios, e.g., Fe^+/Fe^0. All the EclipSS targets are MS dwarfs, or slightly evolved, as verified by their Gaia luminosities, and thus are expected to fall in a relatively narrow range of $\log g \sim 4.1$–4.6 cm s^{-2}. Metallicity normally is also derived through model atmospheres analyses of optical absorption spectra, and often accompanies companion $\log g$ and $T_{\rm eff}$ values in a catalog.

Almost all of these quantities are based on measured magnitudes and colors, or atmospheric modeling. The main exception is spectral type, which normally comes from examination of low-resolution classification spectra, which can result in inconsistent type assignments for the same object depending on the source material and/or evaluations of it. In fact, the effective temperature is a more fundamental way to categorize stars, specifically here with regard to convection properties. Nevertheless, $T_{\rm eff}$ determinations, from SEDs or modeling, can also be problematic. Thus, two parallel approaches were taken to obtain a more uniform system of spectral types and effective temperatures for the EclipSS stars, recognizing that both quantities are closely related.

Because spectral types are a classification of low-resolution optical spectra, the most natural surrogate would be a broad-band color. The Gaia $(bp - rp)$ color was chosen for the purpose, because the Gaia catalog is extensively populated out to, and beyond, the 100 pc outer solar neighborhood (the horizon of the EclipSS sample); the color is broad-band in nature; and the space measurements are expected to be uniform, at least compared to ground-based analogs, given the lack of atmospheric interference. Also, any differential color corrections due to interstellar extinction should be small given the proximity of the EclipSS sample. Figure A1 illustrates the spectral-type versus color calibration.

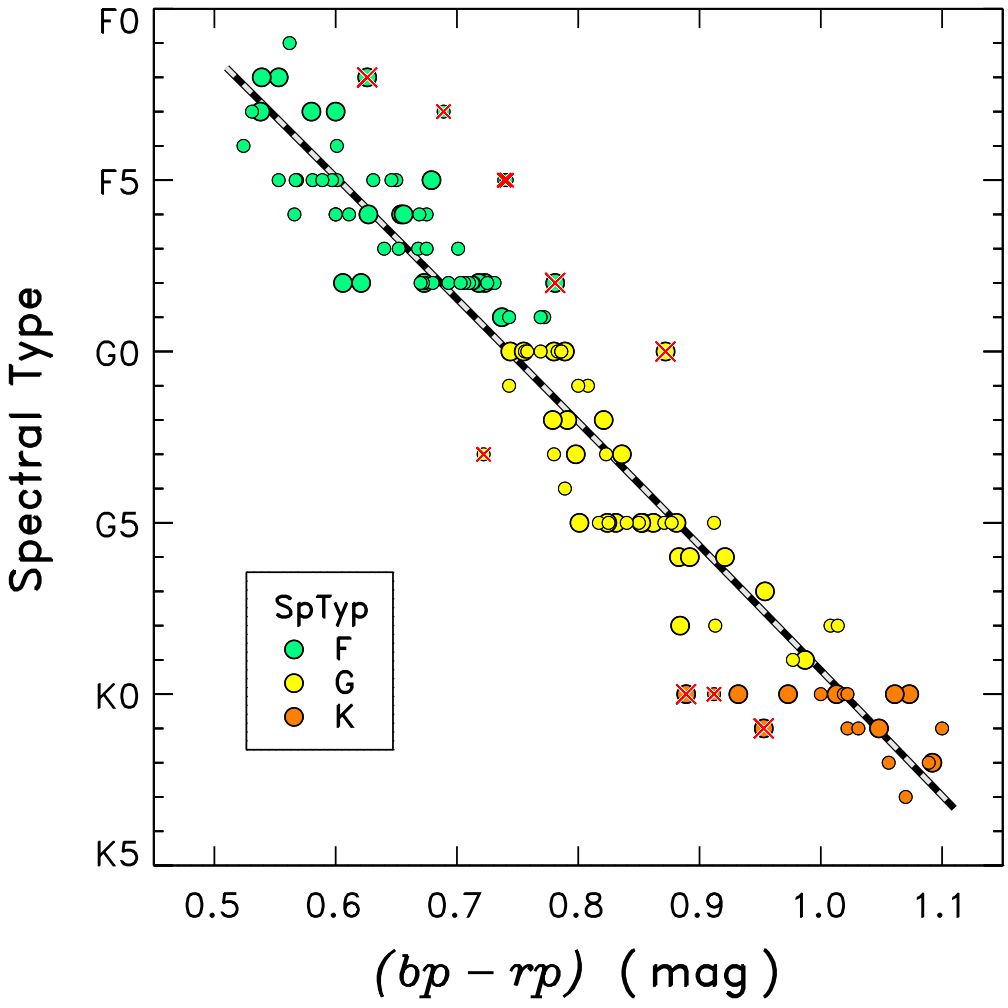

Fig. A1.— Empirical calibration of spectral type versus Gaia color index based on Hipparcos types for the EclipSS stars (larger dots) and a collection of nearby FGK dwarfs from a separate program (smaller dots). The dashed curve is the adopted best-fit relation, ignoring outliers (marked by red ×).

The figure depicts spectral types (uniformly drawn from the Hipparcos catalog) and Gaia colors for two samples of stars: EclipSS (larger dots), and an additional collection of nearby FGK dwarfs (smaller dots) from a separate analysis (subject of a subsequent paper of this series concerning the Mg II "Wilson-Bappu Effect"[14]). The dashed line behind the symbols is a quadratic fit (albeit only slightly curved), ignoring the 10 most discrepant of the 127 original points (excluded values are marked by a red ×). The derived correlation then was applied back to the EclipSS sample, to provide a new set of spectral types more consistent with the Gaia colors.

The equivalent rationalization of the effective temperatures was less straightforward. The complexity mirrors the fact that "$T_{\rm eff}$" has multiple meanings and can be derived in multiple ways. For example, there is the simple *definition* of the effective temperature in terms of L and R through the Stefan-Boltzmann law. Secondly, the effective temperature can be obtained by fitting an observed SED, relying on the fact that the emergent photospheric radiation arises in optically thick layers where the local ("surface") temperatures are closely related to the model $T_{\rm eff}$. Thirdly, and for similar reasons, a model $T_{\rm eff}$ can be estimated by reference to temperature-sensitive line ratios. Effective temperatures quoted for individual objects in the literature, or a catalog, could come from application of one, or more, of these approaches.

There are a number of extensive listings of stellar effective temperatures. Two important sources are the SIMBAD general catalog of stellar properties, and PASTEL (Soubiran et al. 2016), a compendium of $T_{\rm eff}$, $\log g$, and [Fe/H] with over 80,000 records (v2020-01-30). Two additional useful tabulations are Gaia DR2 and the TESS Input Catalog (TiC: Stassun et al. 2018). All these sources are not completely independent, especially SIMBAD and PASTEL, which have numerous overlaps. Further, for a catalog like SIMBAD that lists multiple $T_{\rm eff}$ entries per object from the literature, one must be cautious accepting specific values, given that a later study might simply quote an earlier result in its tables, which then might be picked up as an ostensibly independent entry in the top-level catalog. Such repeated values usually are straightforward to identify, but not always.

[14]The traditional WBE is a remarkable correlation between the widths of the Ca II H & K chromospheric emission cores and stellar absolute visual luminosity, discovered by Wilson & Vaina Bappu (1957).

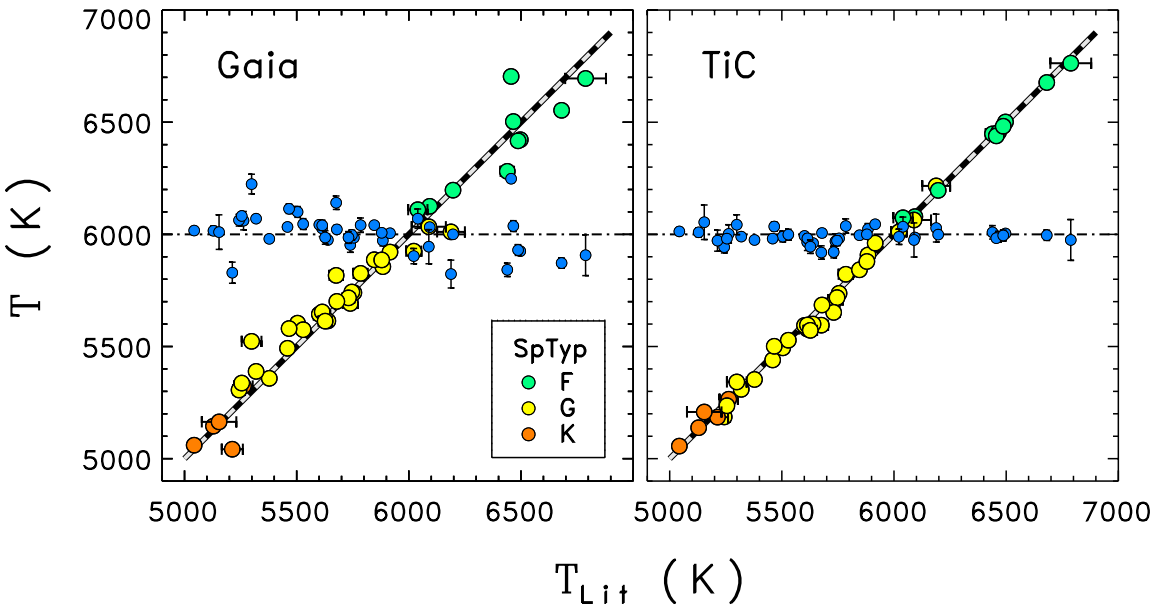

Fig. A2.— Comparison of $T_{\rm eff}$ from Gaia DR2 (left panel) and the TESS Input Catalog (right panel) versus aggregated literature values from the PASTEL Catalog and SIMBAD. Color-coding by type is according to the legend. Slanted dashed lines are 1:1 correlations. Small blue dots depict $T - T_{\rm Lit}$: dotted-dashed lines are the zero points for the differences, but otherwise the y-axis scale applies in a relative sense.

The approach adopted here was to collect a more-or-less unique set of $T_{\rm eff}$ for each EclipSS target mainly from PASTEL, but supplemented in several cases by SIMBAD; then combine the average aggregated value with two additional realizations, one from the TiC and a second derived from an empirical correlation between effective temperature and the Gaia $(bp - rp)$ color (similar to what was done for spectral type). In the combination procedure, the aggregated PASTEL/SIMBAD value was weighted by the number of accepted, ideally independent, measurements; which might be zero if no entries were available, or as many as a dozen for "popular" stars (typically hosts of substellar-mass companions, because the faint EclipSS stars otherwise are inconspicuous). The two additional temperatures—$T_{\rm TiC}$ and $T_{(bp-rp)}$—were included in the average with unit weighting. In this way, a star lacking any $T_{\rm eff}$ entries in the primary catalogs would still benefit from the average of the TiC and $(bp - rp)$ temperatures, while those stars with numerous independent catalog entries would further benefit from the averaging process (but still be anchored to some extent by the two additional $T_{\rm eff}$ realizations).

The TiC temperatures were favored over those listed in Gaia DR2, because $T_{\rm TiC}$ displayed a better correlation with the literature values (PASTEL and SIMBAD) than $T_{\rm Gaia}$, as

shown in Figure A2. The left hand panel depicts the Gaia temperature versus the average literature $T_{\rm eff}$ for the EclipSS targets having two or more of the latter entries. The larger green, yellow, and orange symbols represent EclipSS stars color-coded according to spectral type (F, G, and K, respectively). The slanted dashed line is the 1:1 relation. Smaller blue dots depict the differences (the horizontal dotted-dashed line is the zero point for the differences, but otherwise the y-axis scale applies in a relative sense). $T_{\rm Gaia} - T_{\rm Lit}$ shows significant scatter, and a possible slight negative trend toward higher temperatures. The right hand panel is the similar comparison for $T_{\rm TiC}$. Now, the scatter is reduced and no systematic trends are evident.

Figure A3 presents, in the left panel, a correlation of $T_{\rm Lit}$ values against Gaia $(bp - rp)$ for the WBE dwarf sample and EclipSS targets, as in Fig. A1, again retaining the stars with two or more unique temperature entries. The overlying curve is a fit of the form:

$$T_{\rm eff} \sim 5000 \times (1.8940 - 1.1846\,(bp - rp) + 0.3422\,(bp - rp)^2)\ , \tag{A5}$$

which matches the empirical values tolerably well. The right panel isolates the EclipSS stars, on top of the same correlation derived in the left panel. Again the agreement is good, suggesting that the $(bp - rp)$ temperature is a useful adjunct to $T_{\rm Lit}$ and $T_{\rm TiC}$. It is not clear, however, how independent the three different temperature estimates are, but hopefully by considering more than a single source of $T_{\rm eff}$ will help minimize possible systematics. In the final analysis, it is worth noting that the derived temperatures play only a minor role in this study, mainly in constructing the Fig. 2 H–R diagram and deriving bolometric corrections (as described below), but were provided with the thought that they might be useful in any future analyses of the EclipSS sample.

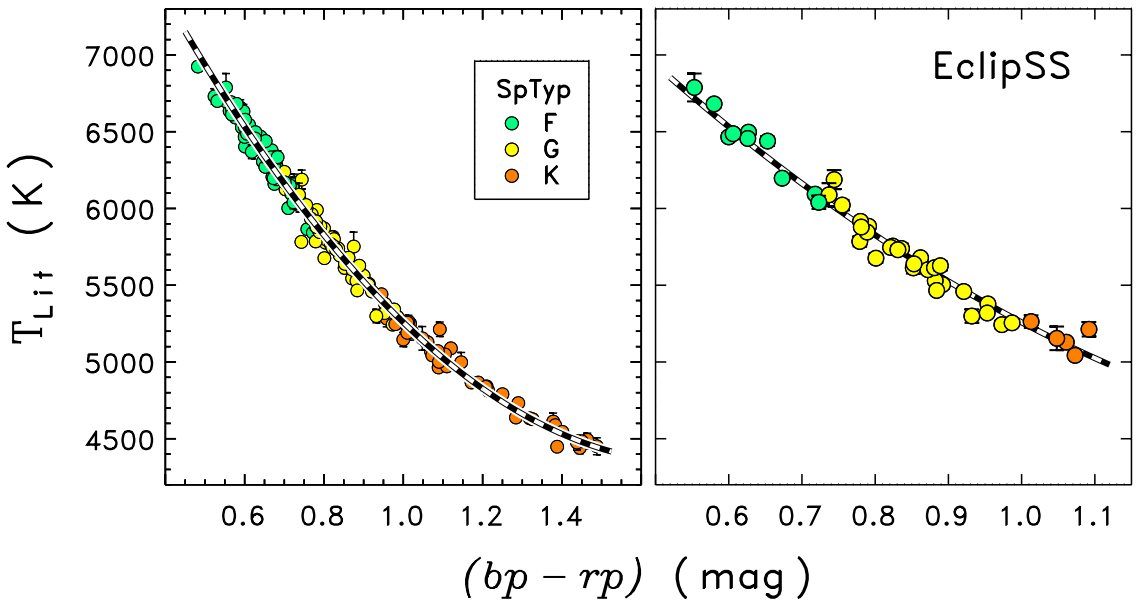

Fig. A3.— Correlation of $T_{\rm Lit}$ for the WBE dwarf sample and EclipSS targets versus Gaia color in the left panel. The overlying dashed curve is a least-squares parabolic fit. The EclipSS values are shown in the right panel, alone, on top of the same relation.

The final quantity central to the analysis is the bolometric correction, BC, mentioned earlier in the context of the bolometric flux. Here, again, the Casagrande & VandenBerg (2018) results were adopted. Figure A4 illustrates the variation of their solar-metallicity BCs with effective temperature for three different surface gravities, $\log g = 4.0$ (upper blue dots), 4.5 (middle dark), and 5.0 (lower red). The $\log g = 4.5$ curve was chosen for the EclipSS targets, given the expectation that their surface gravities would hover around the solar value, and in any event the variation of BC with $\log g$ is relatively minor. The dashed curve is an alternative formulation from Andrae et al. (2018), which is systematically lower than the C&V points by about 0.02 mag, but the relations agree within the uncertainties of the latter analysis.[15]

[15]If the Andrae et al. result had been adopted literally (e.g., $\mathrm{BC}_\odot \sim 0.06$ mag), the constant coefficient in eq. A1 would have to be lowered slightly, to 2.50×10^{-5} (a decrease corresponding to +0.02 mag devolving from the −0.02 mag change in the $(G_\odot + \mathrm{BC}_\odot)$ factor). However, since the Andrae et al. BCs largely parallel the C&V curve (i.e., $\Delta(\mathrm{BC}) \sim -0.02$ mag independent of $T_{\rm eff}$) for much of the EclipSS temperature range, the final calculated $f_{\rm BOL}$ values would be unchanged.

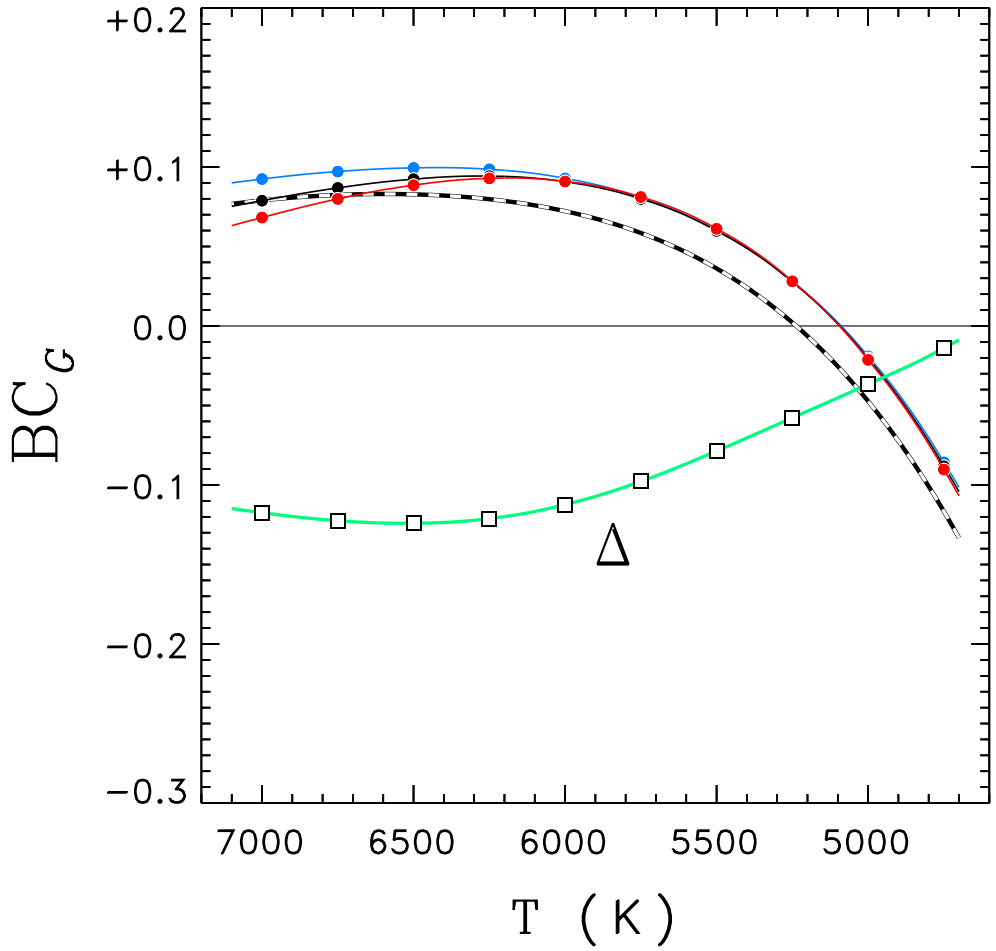

Fig. A4.— Casagrande & VandenBerg bolometric corrections for the Gaia G magnitude versus $T_{\rm eff}$ for three surface gravities and standard solar composition (solid curves and dots; $\log g = 5.0$ is lower curve, 4.5 (adopted for EclipSS) in middle, and 4.0 upper). Curve labeled "Δ" represents the change in BC going to a low-metallicity star with [Fe/H]= −2. Dashed curve is an alternative distribution from Andrae et al. for $\log g = 4.5$ and [Fe/H]= 0.

The green-connected open squares in Fig. A4 represent the difference, for the $\log g = 4.5$ case, between the C&V BCs for [Fe/H] $= -2$ and those for [Fe/H] $= 0$ (i.e., solar composition). The low-metallicity case has smaller BCs, thus the Δ factors are negative. Several of the EclipSS stars have [Fe/H] $\lesssim -0.5$, so the bolometric correction was adjusted as follows,

$$\mathrm{BC} = \mathrm{BC}_0(T_{\rm eff}) + (\{\,[\mathrm{Fe/H}] < 0\,\}/\{-2\}) \times \Delta(T_{\rm eff}) \ , \tag{A6}$$

where the leading term is the $T_{\rm eff}$-dependent BC relation for $\log g = 4.5$ and solar composition, and the parenthetical coefficient in the second term (for metallicity) is understood to be zero unless [Fe/H] is negative. (Only a few of the EclipSS stars have positive [Fe/H], typically less than a (negligible) $+0.2$.) The quantity $\Delta(T_{\rm eff})$ is the green curve in Fig. A1.

Table A1 lists the fundamental magnitudes, colors, and various $T_{\rm eff}$ collected for the EclipSS sample, and used in the previous diagrams. Table A2 presents other fundamental parameters, including the consensus $T_{\rm eff}$ based on the values summarized in Table A1, as well as surface gravities and metallicities aggregated in the same way from PASTEL and SIMBAD as the $T_{\rm Lit}$ described earlier. A top-level summary of the Table A1 and A2 parameters is provided in Table 1 of §2 (Observations).

Table A1. Magnitudes, Colors, and Temperatures

Name	Type	Type′	G	$(bp-rp)$	V	$(B-V)$	$(V-I)$	$T_{\rm Lit}$ [$N_{\rm Lit}$]	$T_{\rm Gaia}$	$T_{(bp-rp)}$	$T_{\rm TiC}$
					(mag)				(K)		
(1)	(2)	(3)	(4)	(5)	(6)	(7)	(8)	(9)	(10)	(11)	(12)
HD 20052	G0	G0	+8.175	+0.744	+8.32	+0.581	+0.65	6188±62 [2]	6011	6010	6216
HD 21166	F3	F4	+7.117	+0.580	+7.23	+0.413	+0.50	6681±23 [2]	6553	6610	6677
HD 22359	F8	F6	(+7.46)	+0.621	+7.56	+0.506	+0.58	6244± 0 [1]	5287	6452	6244
HD 24293	(G3)	G3	+7.684	+0.836	+7.85	+0.658	+0.72	5739±33 [3]	5692	5714	5708
HD 24636	F3	F3	+7.022	+0.538	+7.13	+0.400	+0.46	···	6723	6779	6776
HD 28471	G5	G3	+7.728	+0.824	+7.89	+0.650	+0.71	5755±12 [5]	5740	5751	5737
HD 28481	F6	F7	+8.167	+0.656	+8.29	+0.500	+0.57	···	6329	6321	6174
HD 28701	G2	G3	+7.695	+0.821	+7.86	+0.650	+0.71	5746±22 [8]	5743	5761	5718
HD 29255	F6	F7	+8.257	+0.654	+8.37	+0.501	+0.57	6439±30 [2]	6281	6328	6448
HD 30501	K0	K2	+7.339	+1.061	+7.58	+0.875	+0.91	5129±20 [6]	5145	5112	5138
HD 32778	G5	G3	+6.841	+0.831	+7.02	+0.636	+0.72	5731±26 [4]	5717	5730	5652
HD 34297	G5	G4	+7.144	+0.852	+7.32	+0.652	+0.72	5613±37 [4]	5640	5666	5578
HD 36767	F8	F9	+7.020	+0.718	+7.17	+0.538	+0.61	6093±15 [3]	6125	6099	6079
HD 38459	K0	K0	+8.292	+1.013	+8.52	+0.861	+0.90	5263±41 [6]	5324	5226	5265
HD 39194	K0	G8	+7.852	+0.973	+8.09	+0.760	+0.84	5243±26 [7]	5306	5327	5186
HD 39755	F2	F3	+7.739	+0.539	+7.84	+0.435	+0.50	···	6813	6775	6856
HD 41004	K2	K3	+8.376	+1.092	+8.65	+0.887	+0.93	5213±47 [4]	5042	5042	5185
HD 42286	K0	K2	+8.189	+1.073	+8.45	+0.844	+0.89	5043±17 [3]	5060	5085	5056
HD 47252	G9	G9	+8.033	+0.987	+8.27	+0.781	+0.82	5255±15 [3]	5337	5291	5236
HD 51608	G7	G8	+7.961	+0.954	+8.17	+0.771	+0.80	5378±12 [7]	5358	5377	5353
HD 51929	G2	G1	+7.240	+0.779	+7.39	+0.585	+0.66	5785±32 [10]	5826	5894	5822
HD 53658	F6	F6	+7.213	+0.627	+7.33	+0.464	+0.53	6497±13 [2]	6422	6429	6501
HD 55720	G6	G5	+7.309	+0.892	+7.50	+0.705	+0.75	5504±24 [6]	5604	5548	5494

Table A1—Continued

Name	Type	Type′	G	$(bp-rp)$	V	$(B-V)$	$(V-I)$	$T_{\rm Lit}$ [$N_{\rm Lit}$]	$T_{\rm Gaia}$	$T_{(bp-rp)}$	$T_{\rm TiC}$
					(mag)				(K)		
(1)	(2)	(3)	(4)	(5)	(6)	(7)	(8)	(9)	(10)	(11)	(12)
HD 56737	F3	F5	+7.040	+0.600	+7.17	+0.437	+0.51	6466±24 [2]	6503	6532	6455
HD 62850	G2	G2	+7.033	+0.791	+7.17	+0.637	+0.70	5884±24 [2]	5856	5855	5908
HD 63765	G6	G6	+7.910	+0.921	+8.10	+0.745	+0.79	5459± 8 [7]	5492	5466	5440
HD 64184	G5	G4	+7.312	+0.862	+7.49	+0.675	+0.73	5679±18 [6]	5701	5636	5685
HD 73744	G0	G2	+7.424	+0.789	+7.58	+0.607	+0.68	5846±12 [3]	5887	5862	5842
HD 137826	G6	G5	+8.556	+0.883	+8.73	+0.685	+0.74	5529±24 [5]	5575	5574	5528
HD 144061	G5	G2	+7.120	+0.801	+7.26	+0.654	+0.72	5676±30 [9]	5817	5823	5595
HD 146044	G0	G5	+7.934	+0.872	+8.12	+0.688	+0.75	5601±16 [3]	5644	5606	5594
HD 146868	G5	G4	+7.510	+0.853	+7.67	+0.659	+0.72	5639±13 [6]	5614	5663	5600
HD 147231	G5	G5	+7.654	+0.881	+7.83	+0.722	+0.77	5614±20 [6]	5654	5580	5596
HD 150706	G0	G1	+6.850	+0.780	+7.01	+0.607	+0.68	5916±12 [15]	5921	5891	5961
HD 151541	K1	G8	+7.344	+0.953	+7.56	+0.769	+0.81	5319±16 [11]	5389	5379	5309
HD 154956	F5	F8	+8.141	+0.679	+8.28	+0.460	+0.53	···	6093	6237	6114
HD 156389	F2	F6	+7.707	+0.626	+7.79	+0.457	+0.53	6456±17 [2]	6704	6433	6439
HD 156559	F2	F3	+7.782	+0.553	+7.89	+0.413	+0.48	6788±91 [2]	6695	6718	6763
HD 159329	F9	G0	+7.519	+0.737	+7.66	+0.581	+0.65	6089±76 [2]	6034	6034	6064
HD 161897	K0	G5	+7.418	+0.889	+7.60	+0.720	+0.77	5627±30 [4]	5613	5557	5572
HD 165700	F8	F8	+7.645	+0.673	+7.79	+0.456	+0.53	6197± 5 [2]	6197	6259	6196
HD 168093	F8	F9	+7.507	+0.723	+7.65	+0.542	+0.62	6040±43 [3]	6110	6082	6074
HD 172669	G3	G2	+7.415	+0.798	+7.58	+0.618	+0.69	···	5856	5833	6061
HD 180712	F8	G1	+7.822	+0.781	+7.97	+0.606	+0.68	5879±13 [3]	5886	5888	5879
HD 185239	F8	F5	+8.033	+0.606	+8.15	+0.452	+0.52	6487±24 [2]	6417	6509	6482
HD 187876	G0	G0	+7.611	+0.755	+7.76	+0.613	+0.68	6022±34 [2]	5925	5973	6011

Table A1—Continued

Name	Type	Type′	G	$(bp-rp)$	V	$(B-V)$	$(V-I)$	$T_{\rm Lit}$ $[N_{\rm Lit}]$	$T_{\rm Gaia}$	$T_{(bp-rp)}$	$T_{\rm TiC}$
					(mag)				(K)		
(1)	(2)	(3)	(4)	(5)	(6)	(7)	(8)	(9)	(10)	(11)	(12)
HD 199476	G8	G5	+7.625	+0.884	+7.81	+0.685	+0.74	5466±21 [3]	5580	5571	5501
HD 201651	K0	G7	+7.987	+0.932	+8.19	+0.766	+0.81	5299±44 [2]	5523	5436	5342
HD 202123	K1	K1	+8.444	+1.048	+8.69	+0.832	+0.87	5154±77 [3]	5164	5142	5208

Note. — Col. 2 spectral types are from the Hipparcos catalog, except for HD 24293 from SIMDAD. (Adopted) Col. 3 spectral types were based on a correlation between spectral type and the Gaia $(bp-rp)$ color (Fig. A1). Cols. 4 and 5 magnitudes and colors are from Gaia DR2, except for HD 22359, a close-separation, near-equal binary. For this star, the G magnitude (7.855) was too faint compared with Hipparcos Hp (and V), although the $(bp-rp)$ color appears normal with respect to the spectral type and other optical colors of the star. A revised $G \sim +7.46$ mag was estimated from Hp, based on a tight correlation between $(G-Hp)$ and $(bp-rp)$. A similar magnitude ($G \sim 7.43$) was derived from $(G-V)$ versus $(V-I)$ using V and $(V-I)$ from the Hipparcos catalog ($V = +7.56$ for HD 22359) The Hp-derived G is preferred (the Hp bandpass is broad like Gaia G, and also measured in space), and is the one listed in the Table. A further caution: the SIMBAD $V = +9.26$ for HD 22359 is nearly 2 mag fainter than the Hipparcos value. Cols. 6–8 magnitudes and colors are from the Hipparcos catalog. The Col. 9 effective temperatures are an average over aggregated literature values (bracketed $N_{\rm Lit}$ indicates number of unique measurements averaged), based mainly on the PASTEL Catalog (Soubiran et al. 2016: v2020-01-30), but supplemented by SIMBAD if warranted. Col. 10 effective temperatures are that reported in Gaia DR2. Col. 11 effective temperatures were based on a correlation between $T_{\rm eff}$ and $(bp-rp)$. Col. 12 effective temperatures are from the initial version of the TESS Input Catalog (Stassun et al. 2018).

Table A2. Fundamental Stellar Parameters and Derived Quantities

Name	β	ϖ	$v_{\rm R}$	$T_{\rm eff}$	$\log g$	[Fe/H]	BC	$f_{\rm BOL}$	$L/L_\odot$	$R/R_\odot$
	(°)	(marcs)	(km s^{-1})	(K)	(cm s^{-2})		(mag)	(10^{-8})		
(1)	(2)	(3)	(4)	(5)	(6)	(7)	(8)	(9)	(10)	(11)
HD 20052	−71.61	12.67	+28.2	6151± 54 [4]	···	···	0.09	1.23	2.39	1.36
HD 21166	−74.93	11.92	+6.9	6662± 20 [4]	···	···	0.09	3.26	7.16	2.01
HD 22359	−72.86	18.17	(+2.4)	6313± 69 [3]	···	···	0.09	2.37	2.24	1.25
HD 24293	−76.48	23.70	+21.6	5728± 19 [5]	+4.21±0.11 [2]	−0.08±0.04 [2]	0.07	1.96	1.09	1.06
HD 24636	−76.67	17.53	+14.6	6778± 2 [2]	···	···	0.09	3.57	3.62	1.38
HD 28471	−79.86	22.88	+54.7	5752± 8 [7]	+4.40±0.02 [4]	−0.04±0.01 [4]	0.08	1.88	1.12	1.07
HD 28481	−72.88	9.67	+30.5	6248± 74 [2]	···	···	0.09	1.24	4.13	1.73
HD 28701	−80.70	22.58	−6.6	5745± 17 [10]	+4.36±0.05 [6]	−0.30±0.01 [6]	0.07	1.96	1.20	1.11
HD 29255	−80.34	12.13	+8.4	6414± 31 [4]	···	···	0.09	1.14	2.42	1.26
HD 30501	−71.01	49.08	+23.1	5128± 15 [8]	+4.51±0.03 [2]	+0.08±0.00 [1]	0.01	2.87	0.37	0.77
HD 32778	−77.50	44.75	+0.8	5717± 21 [6]	+4.48±0.07 [3]	−0.59±0.03 [2]	0.05	4.36	0.68	0.84
HD 34297	−78.32	28.68	(+31.7)	5616± 26 [6]	+4.40±0.15 [2]	−0.65±0.00 [1]	0.04	3.32	1.26	1.19
HD 36767	−80.47	27.71	+46.3	6092± 9 [5]	+4.42±0.00 [1]	···	0.09	3.55	1.44	1.08
HD 38459	−71.14	26.99	+26.5	5259± 30 [8]	+4.48±0.03 [4]	+0.21±0.04 [2]	0.03	1.17	0.50	0.85
HD 39194	−86.15	37.83	+14.1	5246± 23 [9]	+4.57±0.02 [6]	−0.62±0.02 [5]	0.01	1.79	0.39	0.75
HD 39755	−85.40	12.36	+2.0	6816± 41 [2]	···	···	0.08	1.85	3.78	1.39
HD 41004	−71.68	24.04	+42.5	5180± 41 [6]	+4.39±0.05 [3]	+0.18±0.03 [3]	0.02	1.10	0.59	0.96
HD 42286	−82.95	37.06	+24.0	5054± 12 [5]	+4.61±0.00 [1]	···	−0.01	1.33	0.30	0.72
HD 47252	−86.28	35.55	+42.9	5259± 12 [5]	+4.59±0.00 [1]	···	0.03	1.49	0.37	0.73
HD 51608	−76.94	28.50	+39.9	5375± 9 [9]	+4.39±0.03 [5]	−0.07±0.01 [4]	0.04	1.57	0.60	0.90
HD 51929	−78.38	26.71	+66.3	5797± 28 [12]	+4.21±0.10 [9]	−0.65±0.04 [8]	0.05	3.02	1.32	1.14
HD 53658	−83.78	17.68	+7.4	6481± 18 [4]	···	···	0.09	2.98	2.97	1.37

Table A2—Continued

Name	β	ϖ	$v_{\rm R}$	$T_{\rm eff}$	$\log g$	[Fe/H]	BC	$f_{\rm BOL}$	$L/L_\odot$	$R/R_\odot$
	(°)	(marcs)	(km s^{-1})	(K)	(cm s^{-2})		(mag)	(10^{-8})		
(1)	(2)	(3)	(4)	(5)	(6)	(7)	(8)	(9)	(10)	(11)
HD 55720	−70.58	36.21	+87.4	5508± 18 [8]	+4.54±0.06 [4]	−0.31±0.02 [3]	0.05	2.84	0.67	0.90
HD 56737	−80.19	16.83	+7.0	6480± 20 [4]	···	···	0.09	3.49	3.84	1.55
HD 62850	−76.40	30.38	+17.9	5883± 15 [4]	+4.38±0.00 [1]	···	0.09	3.53	1.19	1.05
HD 63765	−72.14	30.70	+22.5	5457± 7 [9]	+4.47±0.02 [6]	−0.13±0.02 [4]	0.05	1.63	0.54	0.82
HD 64184	−75.81	29.94	−8.6	5674± 14 [8]	+4.47±0.03 [5]	−0.19±0.02 [4]	0.07	2.79	0.97	1.02
HD 73744	−74.70	27.24	+48.3	5849± 7 [5]	+4.47±0.00 [1]	···	0.09	2.47	1.04	0.99
HD 137826	+74.74	20.41	−34.6	5536± 18 [7]	+4.35±0.08 [3]	−0.34±0.03 [3]	0.05	9.03	0.68	0.89
HD 144061	+78.30	33.77	−8.6	5682± 29 [11]	+4.40±0.03 [4]	−0.29±0.04 [4]	0.06	3.34	0.91	0.99
HD 146044	+76.03	23.54	−67.3	5601± 9 [5]	+4.39±0.00 [1]	−0.15±0.00 [1]	0.06	1.58	0.89	1.00
HD 146868	+77.06	32.30	−17.9	5637± 11 [8]	+4.37±0.05 [5]	−0.28±0.02 [5]	0.06	2.34	0.70	0.88
HD 147231	+79.63	24.86	−16.9	5608± 15 [8]	+4.46±0.04 [4]	−0.03±0.03 [4]	0.07	2.03	1.02	1.07
HD 150706	+75.52	35.34	−17.1	5917± 11 [17]	+4.48±0.02 [2]	−0.03±0.01 [1]	0.09	4.18	1.04	0.97
HD 151541	+82.42	41.24	+9.2	5322± 15 [13]	+4.40±0.05 [8]	−0.20±0.01 [8]	0.03	2.79	0.51	0.84
HD 154956	+75.60	10.86	−10.8	6176± 62 [2]	···	···	0.09	1.27	3.36	1.60
HD 156389	+78.25	(11.58)	(−5.9)	6446± 9 [4]	···	···	0.09	1.89	4.40	1.68
HD 156559	+80.33	12.19	−18.0	6764± 41 [4]	···	···	0.09	1.78	3.72	1.41
HD 159329	+85.83	21.86	−34.0	6069± 33 [4]	···	···	0.09	2.25	1.46	1.09
HD 161897	+83.91	33.31	−16.7	5606± 23 [6]	+4.52±0.03 [4]	−0.02±0.02 [4]	0.07	2.52	0.71	0.89
HD 165700	+78.70	11.28	(−11.9)	6212± 16 [4]	···	···	0.09	2.00	4.91	1.91
HD 168093	+74.29	18.56	−9.1	6055± 26 [5]	+4.14±0.00 [1]	−0.15±0.00 [1]	0.08	2.29	2.08	1.31
HD 172669	+86.39	27.69	−6.8	5947±114 [2]	···	···	0.09	2.48	1.01	0.95
HD 180712	+79.14	22.16	−13.5	5881± 8 [5]	+4.43±0.00 [1]	+0.06±0.00 [1]	0.09	1.71	1.09	1.00
HD 185239	+76.01	12.27	+11.0	6491± 11 [4]	···	···	0.09	1.40	2.91	1.35

Table A2—Continued

Name	β	ϖ	$\upsilon_{\rm R}$	$T_{\rm eff}$	$\log g$	[Fe/H]	BC	$f_{\rm BOL}$	$L/L_\odot$	$R/R_\odot$
	(°)	(marcs)	(km s^{-1})	(K)	(cm s^{-2})		(mag)	(10^{-8})		
(1)	(2)	(3)	(4)	(5)	(6)	(7)	(8)	(9)	(10)	(11)
HD 187876	+74.45	21.48	−52.0	6007± 18 [4]	···	···	0.09	2.07	1.40	1.09
HD 199476	+74.10	32.36	−30.3	5494± 24 [5]	+4.54±0.04 [3]	−0.47±0.06 [3]	0.04	2.14	0.64	0.88
HD 201651	+72.76	31.00	−12.7	5344± 37 [4]	+4.48±0.06 [2]	−0.29±0.01 [2]	0.03	1.55	0.50	0.83
HD 202123	+73.04	31.79	+6.8	5162± 44 [5]	+4.47±0.14 [3]	−0.34±0.06 [3]	0.00	1.04	0.32	0.71

Note. — Col. 2 is the Ecliptic latitude. Col. 3 is the parallax from Gaia DR2, except for HD 156389, which is from Hipparcos (no DR2). Col. 4 is the stellar radial velocity from Gaia, otherwise SIMBAD (parenthetical values). Col. 5 is the consensus effective temperature (weighted average of $T_{\rm Lit}$, $T_{(bp-rp)}$, and $T_{\rm TiC}$, but not $T_{\rm Gaia}$, from Table A1). Col. 6 is the average aggregated literature value of the surface gravity, based mainly on the PASTEL Catalog (Soubiran et al. 2016; v2020-01-30), but supplemented by SIMBAD in several cases. Col. 7 is the same for the metallicity. Col. 8 is the bolometric correction. Col. 9 is the bolometric flux at Earth (in 10^{-8} erg cm^{-2} s^{-1}). Col. 10 is the derived stellar luminosity in solar units. Col. 11 is the derived stellar radius in solar units.

REFERENCES

Airapetian, V. S., Barnes, R., Cohen, O., et al. 2020, International Journal of Astrobiology, 19, 136

Andrae, R., Fouesneau, M., Creevey, O., et al. 2018, A&A, 616, A8

Ayres, T. R. 1979, ApJ, 228, 509

Ayres, T. R. 1997, J. Geophys. Res., 102, 1641

Ayres, T. R. 2004, ApJ, 608, 957

Ayres, T. R. 2014, AJ, 147, 59

Ayres, T. R. 2015, AJ, 149, 58

Ayres, T. R. 2018, AJ, 156, 274

Ayres, T. R. 2020a, ApJS, 250, 16 (Paper I)

Ayres, T. R. 2020b, ApJS, (in press: Paper II)

Ayres, T. R., Brown, A., Harper, G. M., et al. 2003, ApJ, 583, 963

Ayres, T. R., Fleming, T. A., Simon, T., et al. 1995, ApJS, 96, 223

Ayres, T. R., Hodges-Kluck, E., & Brown, A. 2007, ApJS, 171, 304

Bressan, A., Marigo, P., Girardi, L., et al. 2012, MNRAS, 427, 127

Canto Martins, B. L., Gomes, R. L., Messias, Y. S., et al. 2020, ApJS, 250, 20

Carlsson, M. & Judge, P. G. 1993, ApJ, 402, 344

Carlsson, M. & Stein, R. F. 1992, ApJ, 397, L59

Casagrande, L. & VandenBerg, D. A. 2018, MNRAS, 479, L102

De Pontieu, B., Title, A. M., Lemen, J. R., et al. 2014, Sol. Phys., 289, 2733

Dere, K. P., Del Zanna, G., Young, P. R., et al. 2019, ApJS, 241, 22

Eddy, J. A. 1976, Science, 192, 1189

France, K., Loyd, R. O. P., Youngblood, A., et al. 2016, ApJ, 820, 89

Gaia Collaboration, Prusti, T., de Bruijne, J. H. J., et al. 2016, A&A, 595, A1

Gehrels, N. 1986, ApJ, 303, 336

Green, J. C., Froning, C. S., Osterman, S., et al. 2012, ApJ, 744, 60

Judge, P. G., Carlsson, M., & Stein, R. F. 2003, ApJ, 597, 1158

Judge, P. G. & Saar, S. H. 2007, ApJ, 663, 643

Kervella, P., Bigot, L., Gallenne, A., et al. 2017, A&A, 597, A137

Laming, J. M., Drake, J. J., & Widing, K. G. 1995, ApJ, 443, 416

Leenaarts, J., Carlsson, M., Hansteen, V., et al. 2007, A&A, 473, 625

Lin, H.-H. & Carlsson, M. 2015, ApJ, 813, 34

Lin, H.-H., Carlsson, M., & Leenaarts, J. 2017, ApJ, 846, 40

Linsky, J. L. 2017, ARA&A, 55, 159

Linsky, J. L., Redfield, S., & Tilipman, D. 2019, ApJ, 886, 41

Ludwig, H.-G., Caffau, E., Steffen, M., et al. 2009, Mem. Soc. Astron. Italiana, 80, 711

Martínez-Sykora, J., Rouppe van der Voort, L., Carlsson, M., et al. 2015, ApJ, 803, 44

Mason, B. D., Wycoff, G. L., Hartkopf, W. I., et al. 2001, AJ, 122, 3466

Nordlund, A., Brandenburg, A., Jennings, R. L., et al. 1992, ApJ, 392, 647

Notsu, Y., Maehara, H., Honda, S., et al. 2019, ApJ, 876, 58

Noyes, R. W., Hartmann, L. W., Baliunas, S. L., et al. 1984, ApJ, 279, 763

Parker, E. N. 1970, ARA&A, 8, 1

Pesnell, W. D., Thompson, B. J., & Chamberlin, P. C. 2012, Sol. Phys., 275, 3

Predehl, P. 2017, Astronomische Nachrichten, 338, 159

Rathore, B. & Carlsson, M. 2015, ApJ, 811, 80

Rathore, B., Pereira, T. M. D., Carlsson, M., et al. 2015, ApJ, 814, 70

Ricker, G. R., Winn, J. N., Vanderspek, R., et al. 2015, Journal of Astronomical Telescopes, Instruments, and Systems, 1, 014003

Robrade, J. 2017, in proceedings of The X-ray Universe 2017 Conference, eds. Jan-Uwe Ness and Simone Migliari, 193 (online: https://www.cosmos.esa.int/web/xmm-newton/2017-symposium)

Schrijver, C. J. 1987, A&A, 172, 111

Shine, R. A. 1983, ApJ, 266, 882

Soubiran, C., Le Campion, J.-F., Brouillet, N., et al. 2016, A&A, 591, A118

Stassun, K. G., Oelkers, R. J., Pepper, J., et al. 2018, AJ, 156, 102

Tu, Z.-L., Yang, M., Zhang, Z. J., et al. 2020, ApJ, 890, 46

Wilson, O. C. & Vainu Bappu, M. K. 1957, ApJ, 125, 661

Woods, T. N., Eparvier, F. G., Hock, R., et al. 2012, Sol. Phys., 275, 115

Zucker, S., Mazeh, T., Santos, N. C., et al. 2004, A&A, 426, 695